Aus dem NeuroCure Clinical Research Center
der Medizinischen Fakultät Charité – Universitätsmedizin Berlin

DISSERTATION

**Neue Methoden der Nachbearbeitung und Analyse
retinaler optischer Kohärenztomografieaufnahmen bei
neurologischen Erkrankungen**

zur Erlangung des akademischen Grades
Doctor rerum medicinalium (Dr. rer. medic.)

vorgelegt der Medizinischen Fakultät
Charité – Universitätsmedizin Berlin

von

Kay Gawlik

aus Bernau

Datum der Promotion: 04.03.2022

Inhaltsverzeichnis

iv

Zusammenfassung

1 Abstrakt

Zusammenfassung

Viele neurologische Krankheiten verursachen Veränderungen in der Netzhaut, die mit Hilfe der optischen Kohärenztomography (*optical coherence tomography*, OCT) dargestellt werden können. Dabei entstehen viele Bilddaten, deren Auswertung zeitintensiv ist und geschultes Personal erfordert.

Ziel dieser Arbeit war die Entwicklung neuer Methoden zur Vorverarbeitung und Analyse retinaler OCT-Bilddaten, um Outcome-Parameter für Studien und diagnostische Marker für neurologische Erkrankungen zu verbessern. Dazu wurden Methoden für zwei wichtige Aufnahmebereiche der Netzhaut, den Sehnervenkopf (*optic nerve head*, ONH) und die Makula, entwickelt.

Für den ONH-Bereich wurde eine automatische Segmentierung auf Basis aktiver Konturen entwickelt, die eine akkurate Segmentierung der inneren Grenzmembran auch bei komplexer Topografie ermöglicht. Für den Bereich die Makula entstand eine intraretinale Schichtensegmentierungspipeline, die von der Auswahl der Bilddaten über die automatische Segmentierung sowie die manuelle Nachkorrektur bis zur Ausgabe verschiedener Schichtdicken in Tabellenform reicht.

Für beide Aufnahmebereiche wurden mehrere Programme entwickelt, die auf einer gemeinsamen Basis zur Verarbeitung von OCT-Daten fußen. Eines dieser Programme bietet eine grafische Oberfläche zur manuellen Verarbeitung der Bilddaten. Mit dieser Software wurden Teile der Referenzdaten manuell erstellt, die innere Grenzmembran des ONH automatisch segmentiert sowie eine komfortable Nachbearbeitung von intraretinalen Segmentierungen vorgenommen. Dies ermöglichte die automatische Auswertung morphologischer Parameter des ONH, wovon einige signifikante Unterschiede zwischen Patienten mit neurologischen Krankheiten und gesunden Kontrollen zeigten. Weiter kam die Schichtensegmentierungspipeline beim Aufbau einer normativen Datenbank sowie in einer Studie zum Zusammenhang des retinalen Schadens mit der kritischen Flimmerfrequenz zum Einsatz.

Ein Teil der Software wurde als freie und quelloffene Software (*free and open-source software*, FOSS) und der normative Datensatz für die Verwendung in anderen Studien freigegeben. Beides wird bereits in weiteren Studien eingesetzt und wird auch die Durchführung zukünftiger Studien vereinfachen sowie die Entwicklung neuer Methoden unterstützen.

Abstract

Many neurological diseases cause changes in the retina, which can be visualized using optical coherence tomography (OCT). This process produces large amounts of image data. Its evaluation is time-consuming and requires medically trained personnel.

This dissertation aims to develop new methods for preprocessing and analyzing retinal OCT data in order to improve outcome parameters for clinical studies and diagnostic markers for neurological diseases. For this purpose, methods concerning the regions of two landmarks of the retina, the optic nerve head (ONH) and the macula, were developed.

For the ONH, an automatic segmentation method based on active contours was developed, which allows accurate segmentation of the inner limiting membrane even in complex topography. For the macular region, an intraretinal layer segmentation pipeline from image data via automatic segmentation to manual post-correction and the output of different layer thicknesses in tabular form was developed.

For both, ONH and macular region, several programs were developed, which share a common basis for processing OCT data. One of these programs offers a graphical user interface for the manual processing of image data. Parts of the reference data were created manually

using this software. Moreover, the inner limiting membrane of the ONH was segmented automatically and post-processing of intraretinal segmentations was performed. This allowed for automatic evaluation of morphological parameters of the ONH, some of which showed significant differences between patients with neurological diseases and the healthy control group. Furthermore, the layer segmentation pipeline was utilized to create a normative database as well as to investigate the correlation of retinal damage and critical flicker frequency.

Part of the software was released as free and open-source software (FOSS) and the normative data set was released for use in other studies. Both are already being used in further studies and will also aid in future studies, as well as support the development of new methods.

2 Einführung

Das Umgebungslicht wird durch das optische System im Auge, bestehend aus Hornhaut, Linse und Glaskörper, zur Netzhaut (auch Retina genannt) geleitet, deren komplexer Schichtenaufbau in Abb. 1 schematisch dargestellt ist. Die Netzhaut nimmt diese Lichtreize auf und erzeugt in den Fotorezeptoren Signale, welche von der Nervenfaserschicht (*retinal nerve fiber layer*, RNFL) zum Sehnervenkopf (*optical nerve head*, ONH) geleitet werden. An diesem werden alle Nervenfasern der Netzhaut gebündelt und gehen in den Sehnerv über, welcher die Signale weiter Richtung Gehirn leitet.

Die Netzhaut ist zusammen mit dem Sehnerv Teil des zentralen Nervensystems (ZNS) und weist ähnliche zelluläre Kompositionen und spezialisierte Immunreaktionen wie die des Gehirns auf [1]. Bei vielen neurologischen Erkrankungen lassen sich daher Veränderungen in der Netzhaut beobachten. Diese krankheitsspezifischen Veränderungen können in einzelnen Schichten der Netzhaut, siehe Abb. 1, wie auch am ONH in Erscheinung treten. Anhand dieser Veränderungen können einige Krankheiten diagnostiziert und deren Verlauf beobachtet werden. Als bildgebendes Verfahren kommt hier die optische Kohärenztomografie (*optical coherence tomography*, OCT) zum Einsatz [2, 3, 4].

Diese Arbeit befasst sich mit der computergestützten Nachbearbeitung und Analyse retinaler OCT-Aufnahmen mit dem Ziel, die quantitative und qualitative Auswertbarkeit zu verbessern. Damit soll der Weg für neue Diagnosemöglichkeiten geebnet sowie das medizinische Personal entlastet werden, um eine engmaschige Verlaufskontrolle für die Patienten zu ermöglichen.
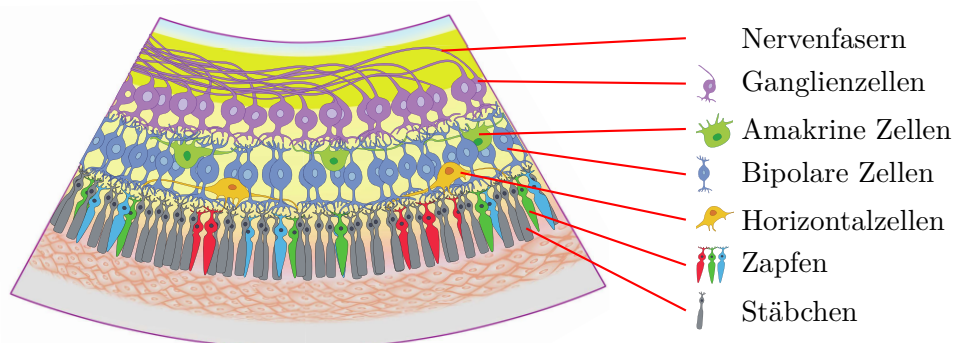
Abbildung 1 – Schematische Darstellung der Netzhaut im Schnitt. Quelle: Abgeleitet von `http://neurodial.de/2017/08/25/schematic-figure-retina-creative-commons-license/` Creative Commons Attribution 4.0 International License

2.1 Neurologischen Erkrankungen

Folgende neurologischen Erkrankungen, die zu spezifischen Veränderungen der Netzhautschichten der Retina bzw. zu charakteristischen Veränderungen des ONH führen, spielen für diese Arbeit eine Rolle:

Multiple Sklerose Die multiple Sklerose (MS) ist die häufigste neuroimmunologische Erkrankung des ZNS. Sie ist eine chronisch-entzündliche Krankheit, die meist im jungen Erwachsenenalter erstmals und überwiegend bei Frauen auftritt [5, 6, 7]. Es handelt sich dabei um eine Autoimmunkrankheit, wobei die T-Zellen des körpereigenen Immunsystems die Myelinscheiden der Nervenfasern angreifen. Im Nachgang kommt es zu Neurodegeneration, die sich in der Netzhaut durch Verdünnung der RNFL und Ganglienzellschicht messen lässt.[8, 9]

Retinale Veränderungen im Rahmen von MS treten vor allem, aber nicht nur, als Folge einer akuten Optikusneuritis auf.[10]

Akute Optikusneuritis Die Optikusneuritis (ON) ist eine Sehnervenentzündung, bei der es zunächst häufig zu einer kurzfristigen Schwellung des Sehnervs und durch retrograde Neurodegeneration zu neuroaxonaler Schädigung der Netzhaut kommt. Dies führt zu einer Verdünnung der RNFL und Ganglienzellschicht schon innerhalb der ersten Tage nach dem Ereignis [11].

Die ON führt zu akutem, meist remittierendem, Sehverlust und langfristig häufig zu Einschränkungen beim Niedrigkonstrastsehen.[2]

NMOSD Neuromyelitis-optica-Spektrum-Erkrankungen wurden lange als seltene Form der MS betrachtet. Seit der Entdeckung des krankheitsspezifischen Antikörpers gegen den astrozytären Wasserkanal Aquaporin-4 (AQP4) wird NMOSD als eigenständige Erkrankung betrachtet [12]. Da NMOSD eine andere Behandlung als MS-Patienten benötigen, ist eine frühe Diagnose wichtig.

Seit 2015 werden NMOSD-Patienten in zwei Gruppen unterschieden, solche mit und ohne vorhandenen Nachweis von AQP4-Antikörpern. Kardinalsymptome sind ON und Myelitis. Tritt die ON im Zusammenhang mit NMOSD auf, führt dies typischerweise zu deutlich stärkerer Verdünnung der RNFL und der Ganglienzellschicht als bei einer ON in MS.[2, 13, 14]

IIH Idiopathic Intracranial Hypertension ist eine schwer zu kontrollierende Krankheit, bei der erhöhter Hirndruck zu dauerhaften visuellen Einschränkungen führen kann. Charakteristisch sind diffuse Kopfschmerzen mit visuellen Störungen. Zusätzlich können ein vergrößerter blinder Fleck, Defekte im visuellen Feld, ein pulsierender Tinnitus und Augen- oder Rückenschmerzen auftreten. In der Netzhaut führt die IIH zu einem Papillenödem und dadurch zu einem vergrößerten ONH-Volumen und – als Folge – zu einer fortschreitenden Verdünnung der RNFL. Die Unterscheidung eines Papillenödems im Rahmen eines IIH von dem im Rahmen einer akuten ON ist nicht immer eindeutig. [15, 16]

2.2 Optische Kohärenztomografie

Die OCT ist ein nicht-invasives Untersuchungsverfahren, um in-vitro Gewebe in hoher Auflösung in der Tiefe zu vermessen.

Für die Untersuchung wird ein Laserstrahl, meist Nahinfrarot, durch einen Strahlteiler in einen Mess- und ein Referenzstrahl aufgeteilt. Der Referenzstrahl wird durch einen Spiegel reflektiert,
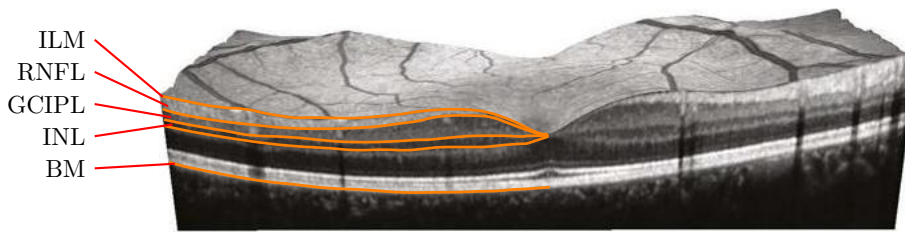
Abbildung 2 – 3D-OCT-Aufnahme mit Schnitt durch die Makula und Segmentierungslinien der für diese Arbeit wichtigsten relevanten Netzhautschichten. Abk.: (*inter limiting membrane*, ILM), (*retinal nerve fiber layer*, RNFL), (*ganglion cell/inner plexiform layer*, GCIPL), (*Inner nuclear layer*, INL)und (*Bruch's membran*, BM) siehe auch Tabelle 1. Quelle: Abgeleitet von `http://neurodial.de/2017/08/25/schematic-figure-macular-oct-with-intraretinal-layers/` Creative Commons Attribution 4.0 International License

Abk.	Beschreibung
ILM	Innere Grenzmembran (*Inter limiting membrane*), bildet den Übergang zwischen Glaskörper und Netzhaut.
RNFL	Nervenfaserschicht (*Retinal nerve fiber layer*), enthält die Nervenfasern
GCIPL	Ganglienzellschicht und innere plexiforme Schicht (*Ganglion cell/inner plexiform layer*), enthält die Zellkörper zu den Nervenfasern der RNFL
INL	Innere Körnerschicht (*Inner nuclear layer*), enthält die Zellkörper der Amakrin-, Bipolar- und Horizontalzellen für die Signalverarbeitung sowie Stützzellen
BM	Bruch-Membran (*Bruch's membran*), schließt die Netzhaut nach unten ab.

Tabelle 1 – Abkürzung und Beschreibung der für diese Arbeit wichtigsten Netzhautschichten. Siehe auch Abb. 1 und Abb. 2.

während der Messstrahl in das zu untersuchende Gewebe eingeleitet wird und dort je nach Gewebeart unterschiedlich gestreut wird. Die Reflexion beider Strahlen wird anschließend überlagert, wodurch ein Interferenzmuster entsteht. Aus dem so erhaltenen Interferenzmuster kann mittels Fouriertransformation das gesamte Tiefenprofil eines A-Scans mit einer Messung berechnet werden.

Die Eindringtiefe ist in den meisten Gewebearten durch Streuung und Absorption auf $2\,\mathrm{mm}$ bis $3\,\mathrm{mm}$ begrenzt, mit einer axialen Auflösung von $1\,\mathrm{\mu m}$ bis $15\,\mathrm{\mu m}$. [17, 18]

2.3 Anwendung der retinalen OCT

Die OCT wird seit Anfang des Jahrtausends verwendet, um die retinalen Veränderungen in neurologischen Erkrankungen zu quantifizieren [19]. Dies ist möglich, da die OCT besonders für die Untersuchung der Netzhaut geeignet ist, da der Glaskörper für das Laserlicht durchlässig und die Methode nicht invasiv ist. Durch die hohe Auflösung sind die einzelnen Netzhautschichten sichtbar und es können mögliche Veränderungen über die Zeit und Abweichungen von der Norm diagnostiziert werden.

In Abb. 2 ist ein 3D-OCT-Scan mit Schnitt durch die Makula mit den für diese Arbeit wichtigsten Schichten zu sehen. Die einzelnen Schichtdicken sowie das gesamte Volumen der Netzhaut im Bereich der Makula sind wichtige Messgrößen, da sie sich je nach Krankheit und dessen Verlauf verändern können und somit Hinweise auf Art und Schwere einer Krankheit liefern.
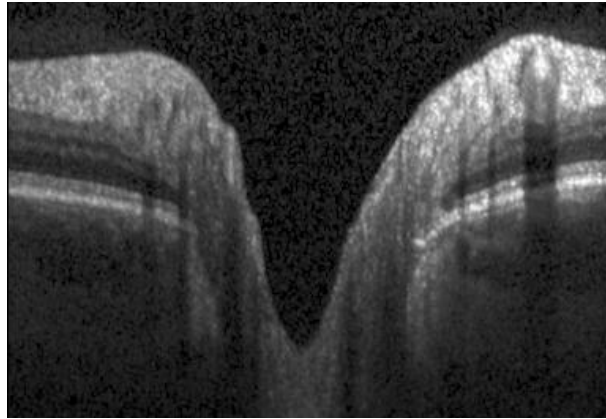
Abbildung 3 – OCT-Schnittbild im ONH-Bereich. Deutlich zu sehen ist die Auflösung der Schichtstruktur der Netzhaut und die Öffnung der BM am Austritt des Sehnervs (Bildmitte). Quelle: Studiendatenbank der AG Klinische Neuroimmunologie am NeuroCure Clinical Research Center der Charité – Universitätsmedizin Berlin

Im Bereich des Sehnervenkopfes löst sich die Schichtstruktur der Netzhaut auf, die BM öffnet sich und an dieser Stelle verlassen alle Nervenfasern das Auge als Sehnerv (Siehe Abb. 3 und 5 sowie Abb. 11 in [20]). Es ergibt sich eine weitere wichtige Messgröße, der minimale Randsaum zwischen dem Rand der BM-Öffnung und der ILM (*Bruch's membrane opening-minimum rim width*, BMO-MRW). Sie beschreibt den maximalen Querschnitt der Nervenfasern an dieser Stelle und ist somit von zentraler Bedeutung für die Diagnose vieler Erkrankungen des Sehnervs [20].

2.4 Probleme bei der Anwendung der retinalen OCT

Obwohl die OCT ein schonendes und kostengünstiges bildgebendes Verfahren ist, existieren einige Einschränkungen.

Um die OCT durchführen zu können, muss der Patient für die Länge der Messung (wenige Sekunden bis mehrere Minuten) ruhig schauen können, da ansonsten starke Artefakte bis hinzu unbrauchbaren Bildern möglich sind [2]. Durch moderne Techniken wie das Augentracking wird diese Einschränkung abgemildert.

Da OCT ein optisches Verfahren ist, darf das Auge keine starken Trübungen haben. Diese können zu starkem Rauschen führen, was eine Auswertbarkeit erschwert bzw. unmöglich macht.

Die für viele Auswertungen nötigen Segmentierungen der Gewebeschichten werden von der Gerätesoftware in der Regel automatisch erstellt. Diese arbeiten auf ungewöhnlichen Aufnahmen/einer atypischen Netzhaut oft unzuverlässig, so dass für eine akkurate Auswertung die Sichtung aller Schnittbilder und eventuell eine Korrektur der Segmentierungen notwendig ist. Dies ist zeitaufwändig und erfordert qualifiziertes Personal. Um diesem einen einheitliche Qualitätsbewertung zu ermöglichen, wurden die OSCAR-IB-Kriterien entwickelt [21, 22].

Da die Algorithmen meist für Makula-Aufnahmen optimiert sind, erfordert die Auswertung anderer Netzhautbereiche, insbesondere des ONH-Bereiches, weiteren Aufwand. Durch diese Einschränkung beschränkt sich die klinische Auswertung oft auf die Makula und wenige andere Parameter. [20]

Erschwerend kommt hinzu, dass die Hersteller ihre Geräte an ein geschlossenes Ökosystem binden, was die Entwicklung und den Einsatz geräteunabhängiger Segmentierungs- und Auswer-

tungsmethoden erschwert. Neben dem zusätzlichen Schulungsaufwand wird dadurch insbesondere die Vergleichbarkeit der Ergebnisse eingeschränkt.

2.5 Fragestellungen

Entscheidend für quantitative Auswertungen von retinalen OCT-Aufnahmen sind hochwertige Segmentierungen der unterschiedlichen Gewebeanteile sowie der ONH-Form [2, 20]. Ziel dieser Arbeit ist die Verbesserung solcher Segmentierungen und darauf aufbauender Auswertungen. Damit sollen die Möglichkeiten klinischer Analysen erweitert und ihre Zuverlässigkeit verbessert werden.

Bei der Segmentierung des ONH liefern die derzeit eingesetzten Methoden oft unbefriedigende Ergebnisse. Insbesondere wird die komplexe Topografie nicht immer korrekt abgebildet. Dies erschwert die Einbeziehung des ONHs in die Diagnose und Verlaufskontrolle von Krankheiten. Bei der intraretinalen Segmentierung ist meist eine zeitaufwändige Kontrolle und Nachbearbeitung nötig, die an die gerätespezifische Software gebunden ist.

Die vorliegende Arbeit beschäftigt sich mit der Segmentierung retinaler OCT-Aufnahmen und darauf aufbauenden medizinischen Anwendungen. Dabei wurden zwei medizinisch besonders relevante Netzhautgebiete, die Makula und der ONH, betrachtet und es wurden auf die jeweiligen Untersuchungsaspekte zugeschnittene Methoden entwickelt. Es ergaben sich dadurch zwei zentrale Fragestellungen, die im Rahmen von 4 Veröffentlichungen bearbeitet wurden:

1. Wie kann die komplexe Topografie des ONH beschrieben und analysiert werden?

2. Wie kann die intraretinale Schichtensegmentierung von Makula-OCT-Bildern und deren Auswertbarkeit verbessert werden?

Als Grundlage wurde ein Framework zur Verarbeitung von OCT-Aufnahmen entwickelt, und darauf aufsetzend wurden weitere Anwendungen erstellt. Eine dieser Anwendungen, der OCT-Marker, verfügt über eine grafische Benutzungsoberfläche, die das Erstellen manueller Segmentierungen und Markierungen innerhalb von OCT-Aufnahmen unterstützt. Der OCT-Marker wurde bei der Bearbeitung beider Fragestellungen verwendet.

In Rahmen der ersten Fragestellung wurde eine 3D-ILM-Segmentierung für ONH-Aufnahmen entwickelt [20], welche eine morphometrische Analyse des ONH ermöglicht [23]. Diese Analysemethode führte bereits zu ersten medizinisch relevanten Ergebnissen [24].

Für die intraretinale Schichtensegmentierung der Makulaaufnahmen wurde der OCT-Marker in einer Segmentierungspipeline (SAMIRIX) eingebunden. Mit Hilfe dieser Pipeline konnte ein normativer Datensatz aufgebaut werden und der Einfluss verschiedener demographischer Parameter auf die Schichten der Netzhaut untersucht werden [25]. SAMIRIX wurde in einer klinischen Beobachtungsstudie angewandt, um zu untersuchen, wie sich die retinalen Veränderungen bei MS im Zusammenhang mit ON auf die klinische Flimmerfrequenz auswirken [26].

3 Methodik

In diesem Abschnitt wird auf die verwendeten Bilddaten eingegangen und die eingesetzten Verfahren und Methoden werden erläutert. Dazu gehört die Auswertung der ONH-Morphometrie, der normative Datensatz sowie die klinische Beobachtungsstudie. Des Weiteren werden die in dieser Promotion entstandene OCT-Softwareplattform, das darauf aufbauende GUI-Programm zur manuellen Bearbeitung der OCT-Daten, die 3D-ILM-Segmentierung, die ONH-Morphometrie und die Schichtensegmentierungspipeline SAMIRIX beschrieben.

3.1 Bilddaten

Die in [20, 23, 25, 26] verwendeten OCT-Bilddaten entstammen der Studiendatenbank der AG Klinische Neuroimmunologie am NeuroCure Clinical Research Center der Charité – Universitätsmedizin Berlin. Sie wurden mit dem Gerät Spectralis-SD-OCT von Heidelberg Engineering (Heidelberg, Deutschland) aufgenommen. Die Studienprotokolle wurden von der lokalen Ethikkommission der Charité genehmigt und in Einklang mit der Deklaration von Helsinki (1964), den Richtlinien zur guten klinischen Praxis (ICH-GCP) und in Deutschland geltendem Recht durchgeführt. Alle Studienteilnehmer gaben ihr schriftliches Einverständnis zur Teilnahme.

Für die ILM-Segmentierung [20] und die Auswertung der ONH-Morphometrie [23] wurden Volumenscans des ONH mit einer Auflösung von $145 \times 384 \times 496$ Voxel verwendet. Diese wurden zentriert auf den ONH mit einem Abtastwinkel von $15° \times 15°$ aufgenommen, was einem Volumen von ca. $4{,}85\,mm \times 4{,}85\,mm \times 1{,}93\,mm$ entspricht.

Für SAMIRIX und die Auswertung des Zusammenhangs zwischen der kritischen Flimmerfrequenz und der Netzhautschichtdicken wurden Makula-OCT-Bilder mit einer Auflösung von $61 \times 768 \times 496$ Voxel und einem Abtastwinkel von $25° \times 30°$ verwendet[25]. Des Weiteren wurden für die Untersuchungen zur Flimmerfrequenz 12°-Ringscans um den ONH mit einer Auflösung von 1536×496 Pixel verwendet[26].

3.2 Statistische Analysen

Für die Durchführung der statistischen Analysen sowie für die Erstellung der Diagramme wurde R (Versionen 3.1.2, 3.3.2, 3.4.4) (R Core Team - `https://www.R-project.org`), GNU Octave 4.0.3 (`https://www.gnu.org/software/octave/`) und Matlab R2017a (The MathWorks, Inc. - `https://www.mathworks.de`) verwendet.

Messwerte wurden als Mittelwert mit Standardabweichung angegeben. Für die Untersuchung der Zuverlässigkeit von Messungen bei Wiederholung [26] sowie Konsistenz zwischen verschiedenen Ratern [25] wurde der Intraklassenkorrelationkoeffizient ((*Intra Class Correlation*, ICC), R-Paket „ICC") verwendet, wobei ein Wert größer als 0,9 als hoch und zwischen 0,8 und 0,9 als moderat bewertet wurde.

Bei allen Testverfahren wurde der Signifikanzlevel bei $p < 0{,}05$ festgelegt. In [26] wurden für den demographischen Vergleich des Geschlechts der χ^2-Test und für das Alter der nichtparametrische Mann-Whitney-U-Test verwendet. Bei Gruppenvergleichen und der Untersuchung von augenbezogenen Parametern wurden verallgemeinerte Schätzgleichungen (*Generalized estimating equations*, GEEs) verwendet, um Abhängigkeiten zwischen den Augen der Probanden zu berücksichtigen.

Für Regressionsanalysen kamen in [25] linear gemischte Modelle (*linear mixed effect models*, LMM) zum Einsatz (R-Pakete: „lme4" und „lmerTest").

Weitere statistische Analysemethoden werden in den Ergebnisteilen der Veröffentlichungen beschrieben.

3.3 OCT-Framework

Die Daten von OCT-Geräten liegen im Allgemeinen in einem proprietären Format vor oder das Auslesen der Bilddaten wurde bewusst erschwert. Bei den von den Herstellern angebotenen Exportformaten fehlen meist wichtige Metadaten und/oder die Export-Prozedur ist unnötig aufwändig. Aus diesen Gründen, und weil der OCT-Anwendungsbereich deutlich kleiner als z.B. der MRT-Anwendungsbereich (Magnetresonanztomographie) ist, haben sich kaum geräteunabhängige Lösungen für die Auswertung von OCT-Daten entwickelt. Diese wenigen Softwarepakete

sind auf spezielle Anwendungsgebiete zugeschnitten und stellen keine Schnittstellen für eigene Entwicklungen bereit.

Um diese Situation zu verbessern und eine eigene Auswertung und Verarbeitung der OCT-Bild- und Metadaten zu ermöglichen, wurde im Rahmen dieser Arbeit ein in der Programmiersprache C++ implementiertes Software-Framework geschaffen. Dies umfasst eine hierarchische Datenstruktur, die mehrere Scans inklusive aller wichtigen Parameter aufnehmen kann. Zum Framework gehören Importfilter für diverse OCT-Formate inklusive einiger gerätespezifische Rohdatenformate. Durch einen modularen Aufbau kann das Framework in verschiedene Anwendungen eingebunden werden.

Für das Framework werden die Bibliotheken OpenCV (`https://opencv.org/`), Boost (`https://www.boost.org/`) und für verschiedene OCT-Formate Zlib (`https://zlib.net/`), DCMTK (`https://dicom.offis.de/`) und OpenJPEG (`https://www.openjpeg.org`) benutzt.

3.4 OCT-Marker

Um Ergebnisse von Algorithmen validieren bzw. diese optimieren zu können, wird oft ein manuell erstellter Goldstandard eingesetzt. Für statistische Analysen müssen automatisch erstellte Segmentierungen manuell überprüft und bei Bedarf korrigiert werden.

Da keines der zur Verfügung stehenden Programme dies hinreichend leisten konnte, wurde, aufbauend auf dem OCT-Framework, ein GUI-Programm mithilfe der Qt-Bibliothek (`https://www.qt.io/`) realisiert. Mit diesem lassen sich die OCT-Daten auswerten und mit manuell erstellten Daten anreichern (siehe Abb. 4). Es ermöglichte außerdem das Erstellen von Zusatzinformationen wie einer A-Scan-bezogenen Scan-Qualität, das Markieren der Bereiche mit unklaren Gewebekanten, die Sichtung und Bearbeitung von automatisch erstellten Segmentierungen, sowie das Erstellen neuer Segmentierungen. Die zwei wichtigsten Funktionen des Programms sind:

Freiformsegmentierung Für das Erstellen eines Goldstandards für die ILM-Segmentierung (Fragestellung 1) wurde eine Segmentierungsmethode benötigt, die beliebige Konturen zulässt. Bei der ILM am ONH treten Überhänge und abstehende Gewebestücke auf. Beides kann zusätzlich im 2D-Schnittbild wie freistehende Gewebestücke oder Löcher wirken.

Diese Besonderheiten am ONH können mit klassischen, 1D-spline-basierten Methoden nicht segmentiert werden. Aufgrund dessen wurde eine pixelorientierte Freiformsegmentierung implementiert. Diese ermöglicht das Zuteilen jedes Pixels in ein Gebiet, z.B. Glaskörper und Gewebe. Diese Zuordnung eignet sich gut für die ILM-Segmentierung (siehe Abschnitt 3.5), da beim verwendeten Verfahren die gleiche Einteilung in zwei Gebiete vorgenommen wird und die Grenzschicht die gesuchte ILM ergibt.

Um die manuelle Segmentierung zu vereinfachen, kann vom Programm eine einfache Startsegmentierung mittels A-Scan-basierter Schwellwertsegmentierung erstellt werden. Dadurch wird eine grobe Trennung vom Glaskörper und dem restlichen Gewebe erreicht. Mittels speziell entworfenen manuellen Werkzeugen kann diese Segmentierung anschließend nachbearbeitet werden. Durch die Startsegmentierung muss meist nur der Bereich in der Nähe der ILM bearbeitet werden.

Programme zur Segmentierung aus dem MRT-Bereich arbeiten ähnlich, für die ILM-Segmentierung waren sie aber weniger geeignet. Diese können nicht mit den Dateiformaten aus dem OCT-Bereich umgehen und bieten nicht die für OCT-Aufnahmen optimierten Werkzeuge an.

Manuelle Schichtensegmentierung Bis dato wurde in der Arbeitsgruppe für die Sichtung und Nachbearbeitung der Schichtensegmentierung ausschließlich die jeweilige gerätespezifische Soft-
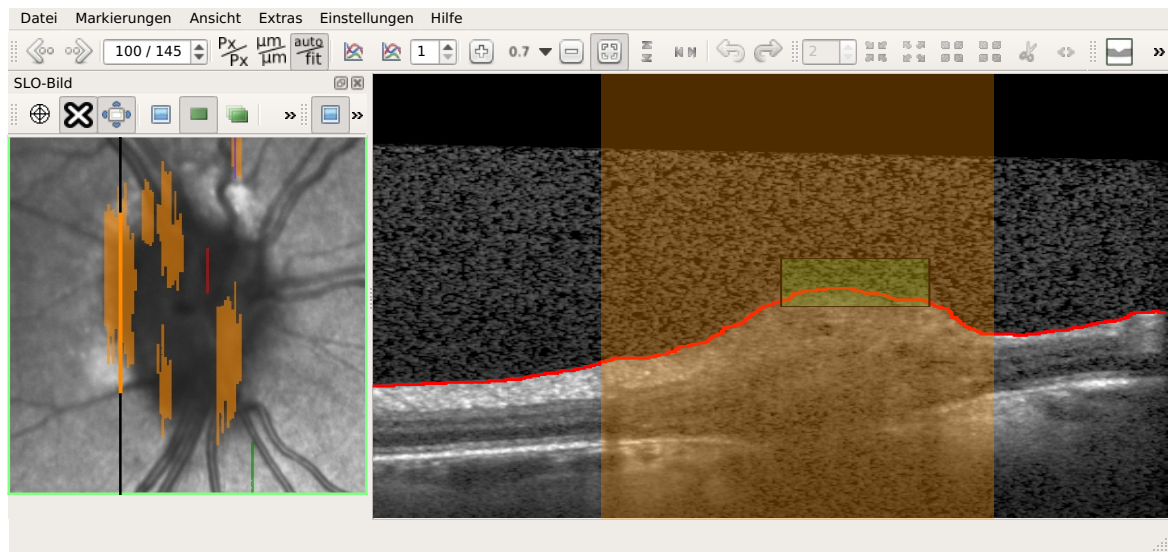
Abbildung 4 – OCT-Marker mit Markierungen für die Auswertung der ILM-Segmentierung. Zu sehen ist im rechten Hauptbereich (OCT-B-Scan) die manuell erstellte Segmentierung (rote Linie), die Markierung der unklaren Gewebekanten (grüner Kasten) und der Bereich mit hohem Rauschanteil (orange Markierung). Im linken Bereich (SLO-Bild) (*Scanning Laser Ophtalmoscope*) ist die A-Scan-basierte Qualitätsmarkierung (orange, rote und grüne Markierungen) der gesamten Aufnahme zu sehen. Quelle: Eigene Darstellung mit OCT-Bild aus der Studiendatenbank der AG Klinische Neuroimmunologie am NeuroCure Clinical Research Center der Charité – Universitätsmedizin Berlin

ware genutzt. Bei Nutzung verschiedener OCT-Geräte ist durch die unterschiedliche Bedienung und die unterschiedlichen Funktionsumfänge eine einheitliche Nachbearbeitung erschwert. Einige gerätespezifische Programme haben keine oder nur wenig Möglichkeit zur manuellen Nachkorrektur.

Zur Verbesserung dieser Situation wurde eine manuelle Schichtensegmentierung und -korrektur auf B-Scan-Basis implementiert. Diese Funktion wurde in der Software SAMIRIX (siehe Abschnitt 3.7) eingesetzt, welche eine Grundlage für die Veröffentlichungen [25] und [26] bildet.

3.5 ILM-Segmentierung

Um die Fragestellung 1, die Beschreibung der komplexen Topografie am ONH, zu bearbeiten, wurde ein aktives-Konturen-Verfahren zur ILM-Segmentierung am ONH-Bereich entwickelt. Beschrieben wurde dieses in [20], die dabei eingesetzten Methoden werden in diesem Abschnitt zusammengefasst. Die entwickelte ILM-Segmentierung basiert auf dem Chan-Vese-Verfahren[27] und der Erweiterung um eine lokale Anpassungsenergie[28].

Das Chan-Vese-Verfahren ist in der Bildsegmentierung ein weit verbreitetes Verfahren. Es wurde für die Segmentierung stark verrauschter Bilder entwickelt, benötigt keine scharfen Kanten und arbeitet auch auf komplexen Topografien zuverlässig. Das Verfahren arbeitet gebietsorientiert und segmentiert solche mit gleichen mittleren Grauwerten. Angewendet auf 3D-Bilddaten ergibt sich eine Trennkontur zwischen den Gebieten, welche im 3D-Raum eine Fläche beschreibt. [20]

Der ONH ist für eine ILM-Segmentierung eine besondere Herausforderung, da neben dem üblichen Rauschen auch eine komplexe Topografie vorhanden ist, die bei jedem Menschen unterschied-

lich ausfällt. Die Bandbreite reicht dabei von tiefen Aushöhlungen bis hin zu stark geschwollenen ONHs ohne Aushöhlung. Es finden sich auch Überhänge, die in einer 2D-Darstellung (B-Scans) wie Löcher oder freistehende Gewebestücke wirken können. Diese, schon bei gesunden Augen erhebliche Bandbreite an Topografien, wird durch Krankheiten weiter vergrößert und deren Ausprägungen werden verstärkt. Z.B. treten bei IIH Schwellungen auf, während es bei anderen zu Gewebeabbau kommt (Siehe Abschnitt 2.1). Aus diesen Gründen liefern etablierte Algorithmen, die in der Regel auf den einzelnen 2D-Schnittbildern arbeiten, oft nicht zufriedenstellende Ergebnisse. [20]

Das Chan-Vese-Verfahren ist dagegen besonders für diesen Anwendungsfall geeignet, da es für eine beliebig komplexe und unscharfe Kontur mit Bildrauschen entwickelt wurde. Durch die 3D-Berechnung können Strukturen, wie Überhänge oder abstehendes Gewebe, die in den einzelnen B-Scans nicht klar als solche erkenntlich sind, ebenfalls korrekt segmentiert werden.

Für die ILM-Segmentierung wird das Bild in zwei Teilgebiete aufgeteilt. Ein Gebiet bildet dabei den Glaskörper ab und das andere sämtliches andere Gewebe. Die Grenzschicht zwischen diesen Gebieten ist dann die gesuchte ILM. In den OCT-Aufnahmen erscheint der Glaskörper schwarz, die meisten Netzhautschichten grau bis weiß. Durch die begrenzte Eindringtiefe der OCT-Technik erscheinen die Gebiete unter der Netzhaut ebenfalls schwarz und auch die inneren Netzhautschichten sind teilweise recht dunkel. Da der Standard-Chan-Vese-Algorithmus für die Segmentierung von Gebieten mit gleicher mittlerer Helligkeit ausgelegt ist und dies bei der ILM-Segmentierung nicht der Fall ist, musste der Algorithmus grundlegend angepasst werden. [20]

Um ein praxistaugliches Verfahren zu erhalten, war außerdem eine sorgfältige, laufzeitoptimierte Implementierung notwendig. Diese umfasst neben angepassten Datenstrukturen auch die Begrenzung aller Energie-Berechnungen in einer Level-Set-Methode ausschließlich im Nahbereich der Kontur (Narrow-Band). Neben der kürzeren Rechenzeiten wird auch ein Überspringen der Kontur auf Glaskörperflocken und in die inneren Netzhautschichten vermieden. [20]

Für die Validierung des Algorithmus wurden 40 Scans, die eine möglichst große Bandbreite an ONH-Topologien abbilden, manuell mit dem OCT-Marker segmentiert. 20 zufällig ausgewählte Scans wurden dabei für eine Parameteroptimierung herangezogen. Durch den Vergleich mehrerer Optimierungsdurchgänge mit jeweils 10 Scans, die wiederum zufällig aus den 20 Scans ausgewählt wurden, konnten Parameter gefunden werden, die auf einer großen Bandbreite von Scans sehr gute Ergebnisse erzielten. [20]

Neben der Implementierung des Segmentierungsalgorithmus entstand ein Qt-basiertes GUI-Programm für die Analyse und Visualisierung des Algorithmus (siehe Abbildung 5) und ein Konsolenprogramm für die automatische Auswertung und den Batchbetrieb. Eine zusätzliche Schnittstelle für das Softwarepaket Octave wurde für die Parameteroptimierung genutzt. Die Implementierung erfolgte vollständig in der Programmiersprache C++ und wurde auf eine kurze Laufzeit hin optimiert.

3.6 ONH-Morphometrie

Für die Fragestellung 1 wurde weiter ein Verfahren in [23] entwickelt, um aus ONH-Aufnahmen mehrere Morphometrieparameter zu extrahieren. Diese können neben den etablierten Schichtdicken zur Diagnose und Verlaufsbeobachtung der oben beschriebenen Erkrankungen genutzt werden[23].

Zur Bestimmung der Parameter wird als erster Schritt eine Segmentierung der BM inklusive der BMO-Punkte (Bruch's membrane opening) durchgeführt. Der Algorithmus verarbeitet jeden B-Scan mit mehreren Filtern einzeln und berechnet eine initiale BM mittels einer A-Scan-weisen
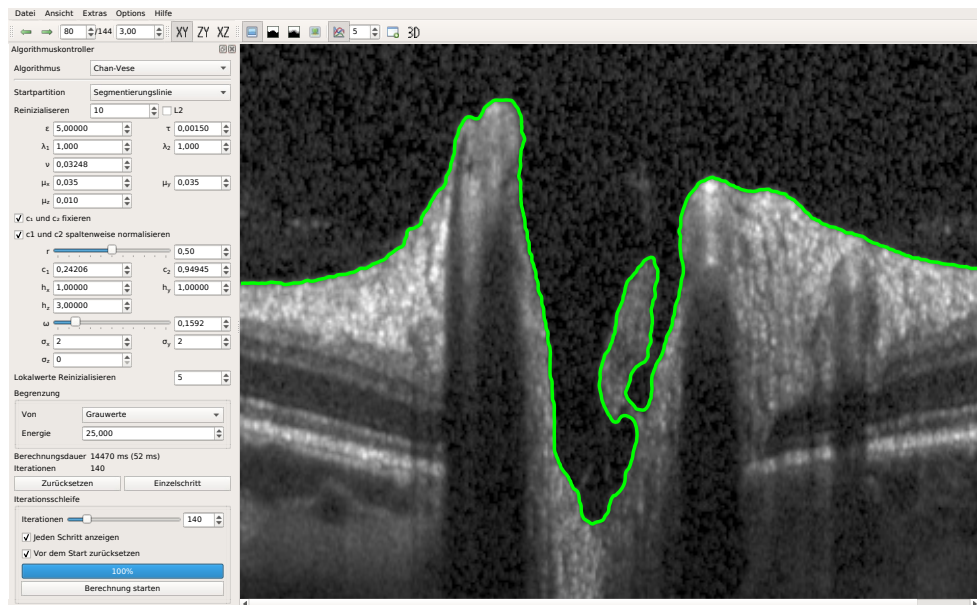
Abbildung 5 – Interaktive Oberfläche für die automatische Segmentierung mit dem Chan-Vese-Verfahren. Es lässt sich jeder Zeitschritt darstellen und bei Bedarf können jederzeit die Parameter anpasst werden. Quelle: Eigene Darstellung mit OCT-Bild aus der Studiendatenbank der AG Klinische Neuroimmunologie am NeuroCure Clinical Research Center der Charité – Universitätsmedizin Berlin

Heuristik. Eine anschließende Splineinterpolation füllt fehlende Bereiche, welche z.B. durch Blutgefäße und den Sehnerv entstehen. [23]

Die interpolierte BM wird anschließend benutzt, um durch weitere Verarbeitungsschritte in einem eingeschränkten Bereich die BMO-Punkte zu bestimmen. Die BMO-Punkte werden abschließend durch eine Ellipse approximiert, um Ausreißer zu entfernen und eine gute Darstellung für die weiteren Berechnungen zu haben. [23]

Als abschießender Schritt der BM-Segmentierung werden die Segmentierungen aller B-Scans mittels einer Flächeninterpolation basierend auf [29] zu einer finalen BM-Segmentierung zusammengesetzt. [23]

Für die Ableitung der Parameter wird neben der BM und den BMO-Punkten die ILM benötigt, welche durch das Verfahren aus Abschnitt 3.5 berechnet wird. Die erhaltene Fläche wird mit dem in [30] beschriebenen Verfahren für die weitere Verarbeitung geglättet. [23]

Zur Berechnung der Morphometrieparameter werden die erhaltenen BM, BMO und ILM zur Bestimmung von Volumina in verschiedenen Bereichen in und um den ONH und zur Berechnung einer Krümmungsenergie[31] der ILM genutzt. [23]

3.7 Schichtensegmentierungspipeline SAMIRIX

Zur Bearbeitung der Fragestellung 2, die Verbesserung der intraretinalen Schichtsegmentierung an Makula-OCT-Aufnahmen und deren Auswertbarkeit, wurde die Segmentierungspipeline »SAMIRIX« in [25] entwickelt. In diesem Abschnitt werden die Methoden aus [25] beschrieben.

Die meist eingesetzte gerätespezifische Software hat verschiedene Einschränkungen, die mit SAMIRIX adressiert wurden und aufgehoben werden konnten. Dazu gehört die durch das Lizenzmo-
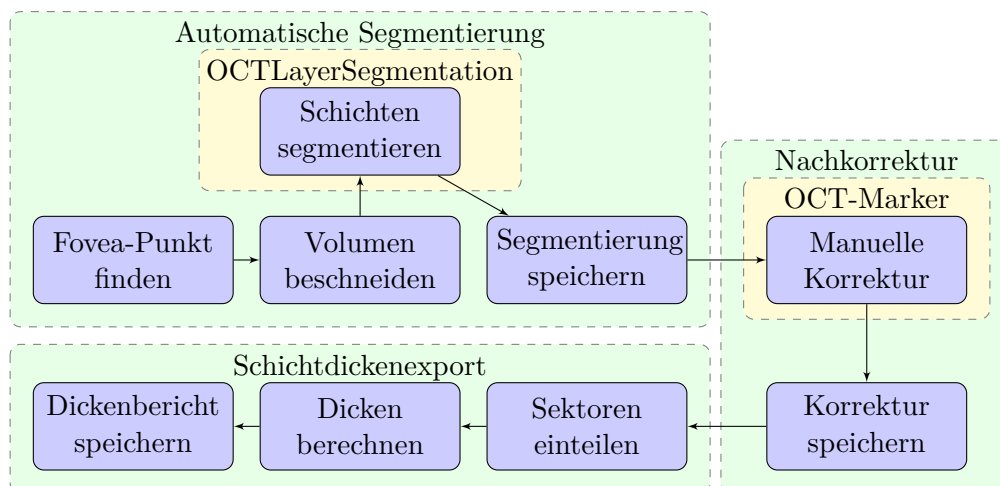
Abbildung 6 – Verarbeitungspipeline SAMIRIX. Zu sehen sind die 3 Verarbeitungsblöcke (Grün) mit den Unterpunkten (Blau). Die gelben Blöcke sind als eigenständige Programme eingebunden. Quelle: Adaptiert aus „Normative data and minimally detectable change for inner retinal layer thicknesses using a semi-automated OCT image segmentation pipeline" [25]

dell eingeschränkte Verwendungsmöglichkeit, sowie die fehlende Möglichkeit eigene Anpassungen und Erweiterungen vornehmen zu können.[25]

Die Segmentierungspipeline wurde sorgfältig auf die Anforderungen im Studienalltag zugeschnitten, kann durch den modularen Aufbau aber leicht an andere Anforderungen angepasst werden. SAMIRIX verarbeitet OCT-Datenformate verschiedener Geräte.[1] Der gesamte Verarbeitungsprozess setzt sich aus 3 Funktionsblöcken zusammen (siehe auch Abb. 6), welche sich auch getrennt nutzen lassen.

Der erste Block führt die automatische Schichtensegmentierung durch. Hier wird der Segmentierungsalgorithmus von OCTLayerSegmentation[2] aus [32] verwendet. Dieser erwartet den Volumen-Scan in einer bestimmten Größe mit dem Fovea-Punkt im Zentrum, welches durch eine Vorverarbeitung – Auffinden des Fovea-Punktes und Beschneidung des Volumens – sichergestellt wird. Als Nachverarbeitungsschritt wird die Segmentierung zusammen mit den Bilddaten in einer neuen Datei abgelegt. [25]

Der zweite Block ermöglicht eine manuelle Nachkorrektur der Segmentierung. Dazu wird der OCT-Marker (siehe Abschnitt 3.4) mit einer speziellen Oberfläche (siehe Abb. 7) gestartet, die eine Begutachtung der Segmentierung im gesamten Volumen und bei Bedarf eine Nachkorrektur ermöglicht. Nach dem Speichern der korrigierten Segmentierung und Beenden des Programms wird die Segmentierung in die Datei zurückgeschrieben. [25]

Der letzte Funktionsblock erstellt einen Schichtdickenbericht. Für diesen werden die Schichtdicken in den verschiedenen Netzhautsektoren berechnet und in einer CSV-Datei gespeichert. [25]

Dieses Verarbeitungs- und Auswerteprogramm ermöglichte unter anderem den erfolgreichen Aufbau eines normativen Datensatzes [25] und die Untersuchung des Einflusses der Schichtdicken auf die kritische Flimmerfrequenz [26] (siehe auch Abschnitt 3.9).

---

[1]In [25] konnten nur VOL-Dateien von HEYEX verarbeitet werden, dies wurde später erweitert.
[2]https://www.nitrc.org/frs/?group_id=905
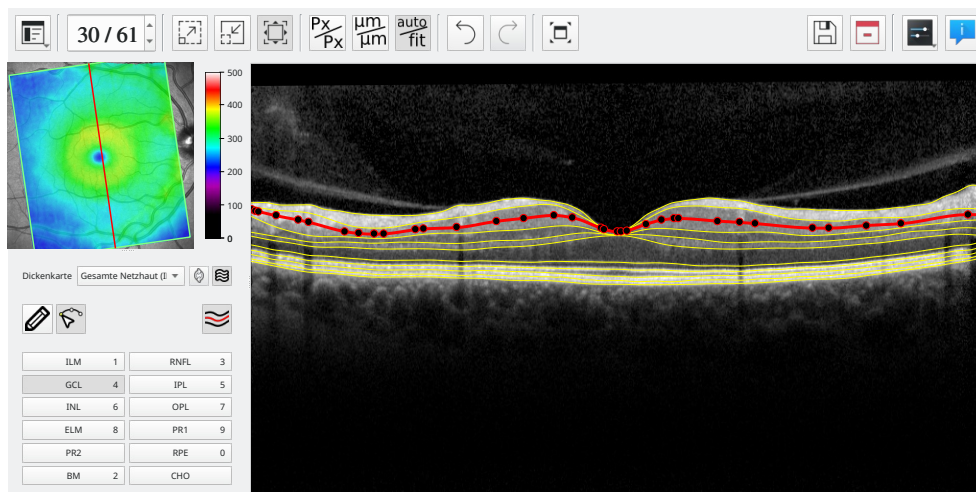
Abbildung 7 – OCT-Marker mit der speziell angepassten Schichtensegmentierungsoberfläche für die SAMIRIX-Pipeline. Die Oberfläche wurde auf das Nötigste reduziert und passend vorkonfiguriert, um einen guten Arbeitsfluss zu gewährleisten. Quelle: Eigene Darstellung mit OCT-Bild aus der Studiendatenbank der AG Klinische Neuroimmunologie am NeuroCure Clinical Research Center der Charité – Universitätsmedizin Berlin

3.8 Normativer Datensatz und kleinste detektierbare Veränderungen

Für Studien werden oft Vergleichsdaten von gesunden Kontrollen und/oder von Patienten mit anderen Krankheiten bzw. anderen Behandlungsmethoden benötigt. Damit diese Vergleichsdaten repräsentativ sind, sollten möglichst viele Personen mit unterschiedlichen Eigenschaften wie Alter und Geschlecht einbezogen werden. Da die Erstellung dieser Vergleichsdaten aufwändig und kostenintensiv ist, kann dies nicht für jede Studie getrennt durchgeführt werden. Aus diesem Grund werden normative Datensätze angelegt, für die diese Vergleichsdaten einmalig erhoben werden und anschließend mehrfach wiederverwendet werden. [25]

Zur Erstellung des Datensatzes mit der SAMIRIX-Pipeline wurden Untersuchungen an 218 gesunden Kontrollen (144 Frauen und 74 Männer) durchgeführt. Neben der Erstellung des Datensatzes war ein Ziel die Bestimmung des Einflusses von Alter, Geschlecht und den Refraktionsfehler auf die Netzhautschichtdicken bei gesunden Kontrollen sowie die Bestimmung der kleinsten Veränderung, die sich durch das Verfahren bestimmen lassen. Das Durchschnittsalter betrug $(36{,}5 \pm 12{,}3)$ Jahre im Bereich von 18 Jahre bis 69 Jahre. Ausschlusskriterien waren alle neurologischen Krankheiten, Krankheiten die bekanntermaßen Auswirkungen auf die Netzhaut haben (z.B. Diabetes, Glaukom), krankhafte Veränderungen, die während der Untersuchung aufgefallen sind, sowie ein Refraktionsfehler über ± 6. [25]

3.9 Retinalen Schichtdicken und kritische Flimmerfrequenz

In einer Studie [26], deren Methoden in diesen Abschnitt beschrieben werden, wurde der Zusammenhang der zeitlichen visuellen Auflösung, gemessen mit der kritischen Flimmerfrequenz (*critial flicker frequency*, CFF), und der Schädigung des visuellen Systems untersucht. Die CFF ist die Frequenz, ab der ein Flimmern als solches wahrgenommen werden kann. Die Messung erfolgte durch den Tastendruck des Patienten/Probanden sobald ein Flimmern wahrgenommen wurde. [26]

Es wurden dazu 39 MS-Patienten und 31 gesunde Kontrollen verglichen. Zusätzlich zur kritischen Flimmerfrequenz wurde das Hoch- und Niedrigkontrastsehen, ein Aufmerksamkeitstest und eine retinale OCT durchgeführt. Bei den Patienten mit MS wurden die visuell evozierten Potentiale gemessen und der Grad der Behinderung mit einer Skala (*expanded disability status scale*, EDSS) bewertet. [26]

Die Auswertung der OCT-Daten wurde mit SAMIRIX (Abschnitt 3.7) durchgeführt.

4 Ergebnisse

Beide Fragestellungen aus Abschnitt 2.5 konnten unter Benutzung der Methoden aus Abschnitt 3 erfolgreich in vier Publikationen bearbeitet werden. Die wichtigsten Ergebnisse werden im Folgenden kurz dargestellt:

4.1 Fragestellung: Wie kann die komplexe Topografie des ONH beschrieben und analysiert werden?

Auf Basis des Chan-Vese-Verfahrens konnte eine 3D-ILM-Segmentierung entwickelt werden, die die mitunter komplexe Topologie des ONH zuverlässig segmentieren kann. Die wichtigsten Ergebnisse aus [20] werden in den folgenden zwei Absätzen zusammengefasst.

Eine performante Umsetzung des Verfahrens ermöglicht eine praxistaugliche Laufzeit auf Standardrechnern[3] ($\approx 15{,}5\,$s pro OCT-Volumen [20]). Durch die dadurch mögliche Parameteroptimierung konnten Parameter gefunden werden, die auf einer großen Bandbreite an ONH-Aufnahmen sehr gute Ergebnisse liefern. Es konnte gezeigt werden, dass diese Methode mit den Parametern genauer und robuster als die ursprünglich eingesetzte Segmentierung ist. Auf unseren Datensatz mit 40 verschiedenen ONH-Formen konnten wir einen mittleren Fehler von $2{,}00\,\mu$m (Standardabweichung $5{,}46\,\mu$m) zum Goldstandard erreichen. Der Algorithmus der OCT-Geräte erreichte einen mittleren Fehler von $4{,}80\,\mu$m (Standardabweichung $12{,}7\,\mu$m). Auf das Volumen im Scanbereich ($27{,}2\,$mm^2) ergab dies einen Fehler von $\approx 35{,}7 \cdot 10^{-3}\,$mm^3 mit dem eigenen Verfahren im Vergleich zu $\approx 57{,}4 \cdot 10^{-3}\,$mm^3 mit dem Verfahren des Geräts. [20]

Insbesondere bei der Segmentierung in Bereichen mit schwieriger Topologie zeigt das Verfahren deutliche Vorteile, da senkrechte Gewebeabschnitte und Überhänge abgebildet werden können. Innerhalb des $1{,}50\,$mm-Radius ($\approx 7{,}07\,$mm^2) um das BMO-Zentrum, wo solche Topologien hauptsächlich auftreten, konnten wir mit einem mittleren Fehler von $11{,}1 \cdot 10^3$ Voxeln im Vergleich zu $18{,}7 \cdot 10^3$ Voxeln der Gerätesegmentierung eine deutliche Verbesserung erreichen. Dies entspricht einer Abweichung von $\approx 18{,}3 \cdot 10^{-3}\,$mm^3 im Vergleich zu $\approx 30{,}9 \cdot 10^{-3}\,$mm^3 bei der Gerätesoftware. [20]

In [23] wurde mittels des generierten 3D-Modells aus der 3D-ILM-Segmentierung, einer Segmentierung der BM und der BMO-Punkte automatisch verschiedene Form-Parameter abgeleitet. Im Folgenden werden einige Ergebnisse aus dieser Veröffentlichung zusammengefasst.

Die Form-Parameter umfassen Flächen-, Volumen- und Abstandsmaße in verschiedenen ONH-Regionen und zusätzlich ein Maß für die Glattheit des ONHs. Diese Parameter erwiesen sich als robust und zuverlässig bei wiederholten Aufnahmen bei einer hohen Bandbreite an ONH-Topologien. In einer ersten Untersuchung konnte gezeigt werden, dass sich die Parameter zur Unterscheidung von gesunden Kontrollen, Patienten mit ON, IIH und entzündlichen Autoimmunkrankheiten (MS und NMOSD) eignen. Für jede Gruppe konnten mehr als 4 Parameter mit

---

[3]Intel Core i7-5600U ($2 \times 2{,}60\,$GHz) mit Debian 9 und gcc 6.3.0

14

	Mean $\pm$ SD	CV (%)	Min - Max	1 - 99 Perzentil	5 - 95 Perzentil
MT	$313{,}70 \pm 12{,}02$	3,83	281 - 362	287 - 340	294 - 333
mRNFL	$39{,}53 \pm 3{,}57$	9,03	30,2 - 54,4	32,4 - 49,2	34,4 - 45,7
GCIPL	$70{,}81 \pm 4{,}87$	6,87	56,6 - 86,0	59,0 - 83,6	63,2 - 78,0
INL	$35{,}93 \pm 2{,}34$	6,52	28,3 - 41,9	31,0 - 41,0	32,1 - 39,9

Tabelle 2 – Durchschnittliche Schichtdicken (in µm) im Radius von 6 mm um die Makula bei 218 gesunden Kontrollen [25]. Abkürzungen: MT: Makulardicke (*macular thickness*), mRNFL: *macular retinal nerve fiber layer*, GCIPL: *combined ganglion cell and plexiform layer*, INL: *inner nuclear layer*, CV: *coefficient of variation*, Min: Minimum, Max: Maximum.

einer Signifikanz von $p < 1 \cdot 10^{-3}$ (Siehe Tabelle 3 in [23]) durch Analyse mit der verallgemeinerten Schätzungsgleichung für die Unterscheidung identifiziert werden. [23]

In einer späteren Analyse zeigten sich bereits spezifische Unterschiede bei AQP4-IgG positiven NMOSD-Patienten im Vergleich zu MS-Patienten. Diese ist möglicherweise durch ein erhöhtes AQP4-Aufkommen in diesem Bereich erklärbar und hat damit hohe differentialdiagnostische Relevanz. [24]

4.2 Fragestellung: Wie kann die intraretinale Schichtensegmentierung von Makula-OCT-Bildern und deren Auswertbarkeit verbessert werden?

Für diese Fragestellung wurde eine interaktive Toolbox zum Aufbau eines normativen Datensatzes für verschiedene Bevölkerungsteilmengen entwickelt. Die wichtigsten Ergebnisse dieser Toolbox und dem Datensatz werden im Folgenden aus [25] zusammengefasst.

Es wurde ein Datensatz von Makula-Volumen-Scans von 218 gesunden Kontrollen (144 Frauen und 74 Männer, Durchschnittsalter $(36{,}5 \pm 12{,}3)$ Jahre im Bereich von 18 Jahre bis 69 Jahre) verwendet. Die dabei bestimmten durchschnittlichen Schichtdicken im Radius von 6 mm um die Fovea können Tabelle 2 entnommen werden[25]. Es konnte beobachtet werden, dass alle Schichten mit zunehmendem Alter geringfügig dünner werden. Bei Männern zeigte sich eine höhere Dicke der Makula und der GCIPL. [25]

Die Zuverlässigkeit bei wiederholten Messungen war ausgezeichnet (ICC > 0,993). Die dabei minimal feststellbaren Veränderungen der Schichtdicken lag über den typischen klinischen Veränderungen in der progressiven Neurodegeneration bei MS, jedoch innerhalb des Bereichs der Schäden, die typischerweise mit akuten Optikusneuritiden verbunden sind[25]. (Siehe Tabelle 2 in [25])

In der klinischen Beobachtungsstudie[26] konnte gezeigt werden, dass die CFF bei Patienten mit MS geringer $((40{,}9 \pm 4{,}4)\,\text{Hz})$ gegenüber gesunden Kontrollen $((44{,}8 \pm 4{,}4)\,\text{Hz})$ ist. Eine ON hat dagegen keinen Einfluss auf die CFF. Ein Einfluss der RNFL-Schichtdicke sowie des GCIP-, INL- und des totalen Makulavolumens auf die CFF konnte nicht nachgewiesen werden[26]. Die ermittelten OCT-Messwerte können Tabelle 3 entnommen werden und decken sich mit den bekannten Werten aus der Literatur [10].

SAMIRIX sowie der OCT-Marker inklusive des darunterliegenden Frameworks wurden als Open-Source-Software unter freien Lizenzen (LGPL3, GPL3 und MIT) veröffentlicht[4] und somit weiteren Forschungsvorhaben zur Verfügung gestellt.

---

[4] https://github.com/neurodial

	ON-Augen	NON-Augen	HC-Augen
pRNFL	$2{,}18 \pm 0{,}37$	$2{,}57 \pm 0{,}39$	$2{,}66 \pm 0{,}22$
GCIP	$1{,}68 \pm 0{,}19$	$1{,}91 \pm 0{,}23$	$1{,}96 \pm 0{,}12$
INL	$1{,}04 \pm 0{,}07$	$1{,}03 \pm 0{,}09$	$0{,}99 \pm 0{,}05$
TMV	$8{,}18 \pm 0{,}39$	$8{,}52 \pm 0{,}53$	$8{,}62 \pm 0{,}34$

Tabelle 3 – Schichtvolumen in mm^3 bei der OCT-Auswertung zur Untersuchung der Parameter zur kritischen Flimmerfrequenz [26]. Abkürzungen: ON-Augen: Augen mit ON, NON-Augen: Augen ohne vorherige ON, HC: *healthy control* ; pRNFL: *peripheral retinal nerve fiber layer*, GCIP: *ganglion cell/inner plexiform layer*, INL: *inner nuclear layer*, TMV: Absolutes Macularvolumen (*total macular volumen*)

5 Diskussion

Die Arbeit präsentiert eine neue Methode für die automatische ILM-Segmentierung des ONH auf Basis aktiver Konturen [20]. Mithilfe dieser lassen sich morphometrische Parameter ableiten, die die Unterscheidung verschiedener Krankheiten (durchgeführt für ON, IIH, MS und NMOSD) ermöglicht [23]. Die ebenfalls in dieser Arbeit entwickelte automatische Segmentierungspipeline mit manueller Nachkorrektur ermöglicht eine komfortable und einheitliche Schichtensegmentierung von Makulaaufnahmen. Insbesondere ist diese Pipeline hervorragend für die Verwendung in größeren Studien geeignet. Im Rahmen dieser Arbeit wurde sie verwendet, um einen normativen Datensatz zu erstellen [25] sowie in einer klinischen Beobachtungsstudie den Zusammenhang zwischen der CFF und den Schichtdicken zu untersuchen [26].

Die implementierte ILM-Segmentierung ermöglicht beim ONH eine automatische, akkurate ILM-Segmentierung trotz der dort auftretenden komplexen Topologie. Gegenüber der ursprünglich genutzten, gerätespezifischen Segmentierung konnte eine deutliche Verbesserung erzielt werden. Auf den genutzten Testdaten konnte der mittlere Fehler mit dem Verfahren von 4,80 μm auf 2,00 μm reduziert werden. [20]

Im Unterschied zu den oft eingesetzten Graph-Cut-Methoden[33, 34] setzt das neue Verfahren auf einen 3D-Energieansatz, wodurch Zusammenhänge zwischen benachbarten B-Scans berücksichtigt werden und somit eine echte 3D-Fläche erzeugt wird. Da wenig OCT-spezifische Vorinformationen im Verfahren eingesetzt werden, lassen sich vielfältige Topologien segmentieren. Insbesondere Überhänge, Ausbuchtungen und verbundene Gewebestücke werden überwiegend sehr gut segmentiert. [20]

Im Rahmen der vorliegenden Arbeit wurde eine beschränkte Anzahl von Volumenscans eines Gerätetyps zur Untersuchung verwendet. Später vorgenommene Versuche mit Daten von anderen Gerätetypen zeigten vielversprechende Ergebnisse, welche weiter analysiert werden sollten. Damit stünde dann eine geräteunabhängige, auch für ONH-Volumensans sehr zuverlässige ILM-Segmentierung zur Verfügung, was insbesondere für Multi-Center-Studien von großem Vorteil wäre.

Neben einer Übertragung auf andere Gerätetypen erlaubt das Verfahren auch Anpassungen für andere Scanarten. So könnte eine Segmentierung auf einem Radialscan, ohne eine Interpolation auf ein kartesisches Gitter und die damit verbundene Einbuße an Genauigkeit, berechnet werden, indem die dem Verfahren zugrundeliegende Level-Set-Gleichung in Zylinderkoordinaten gelöst wird.

Liegen gute Segmentierungsdaten vor, können morphometrische Parameter aus den ONH-OCT-Scans abgeleitet und mit diesen Patienten mit ON, IIH und entzündlichen Autoimmunkrankheiten

sowie gesunde Kontrollen unterschieden werden. Zur Unterscheidung konnten dabei jeweils mehrere Parameter zur Unterscheidung mit einer Signifikanz von $p < 1 \cdot 10^{-3}$ ermittelt werden. Sie könnten damit wertvoll für die Differentialdiagnostik zwischen den Erkrankungen sein. [23]

Im Gegensatz zur erarbeiteten ONH-Morphometrie leiten ältere Ansätze zur Parameterableitung aus ONH-Scans nur wenige Parameter wie z.B. das Volumen und die BMO-MRW ab, benötigen eine manuelle Segmentierung und nutzen nicht die 3D-Struktur der Scandaten aus. [23]

Mithilfe der SAMIRIX-Toolbox konnte eine signifikante Verbesserung der intra-retinalen Segmentierung in Forschungsanwendungen erreicht werden [25]. Sie bietet eine für die Aufgabe optimierte Bedienung und der modulare Aufbau ermöglicht ein einfaches Ersetzen von Komponenten, wie den Segmentierungsalgorithmus oder die manuelle Nachkorrektur, um auch in Zukunft neueren Entwicklungen gerecht zu werden.

Da der verwendete Segmentierungsalgorithmus[34] neben Spectralis-Aufnahmen auch Bildaufnahmen von weiteren Geräten verarbeitet und die andere Software geräteneutral entwickelt wurde, konnten mit Daten von OCT-Geräten von Carl Zeiss Meditec AG (Deutschland, `https://www.zeiss.de/`) und Topcon Corporation (Japan, `https://global.topcon.com/`) erste Tests durchgeführt werden. Dies erforderte nur geringe Anpassungen und lieferte vielversprechende Ergebnisse. Können diese verifiziert werden, so kann der Segmentierungsprozess über mehrere Gerätetypen hinweg vereinheitlicht werden, was Vorteile beim Zeitaufwand, der Qualität und vor allem bei der Vergleichbarkeit von Untersuchungsergebnissen verspricht.

Der aufgebaute normative Datensatz wird als erweiterbare Referenz für Studien dienen, in denen normative Daten nicht anders gewonnen werden. Insbesondere der Einfluss krankheitsunabhängiger Faktoren wie Alter, Geschlecht und Refraktion konnten durch den Datensatz berücksichtigt werden. Mit Makula-Scans von 218 gesunden Kontrollen von 18 bis 69 Jahre bietet sie dafür eine umfangreiche Grundlage. Um diese weiter zu verbessern sollte die Normkohorte noch weiter vergrößert werden, insbesondere auch durch Hinzunahme weiteren Ethnien. Außerdem sollten Untersuchungen mit weiteren OCT-Geräten unterschiedlicher Hersteller, sowie mit weiteren Scanprotokollen durchgeführt werden, um mögliche Abhängigkeiten zu der genutzten Scanart zu vermeiden. [25]

Für die CROCTINO-Studie, eine retrospektive OCT-Studie mit 539 NMOSD-Patienten, wurde die SAMIRIX-Toolbox zur Auswertung der OCT-Daten benutzt [35, 36, 37].

Durch die Anwendung der hier entwickelten Software in klinischen Studien konnte diese gut getestet und ihre Bedienung verbessert werden. Dies und die freie Verfügbarkeit als Open-Source-Software[5] ist eine gute Voraussetzung für die Anwendung in weiteren Studien. Diese Arbeit liefert somit wichtige Bausteine für die weitere Forschung über die direkt erzielten Erkenntnisse hinaus.

Die mit Hilfe der SAMIRIX-Pipeline gewonnen OCT-Schichtdicken (Tabelle 3) sind in guter Übereinstimmung mit der Literatur [10]. Frühere Studien bestätigend konnte gezeigt werden, dass die CFF bei Patienten mit MS und ON signifikant herabgesetzt ist. Die Ergebnisse zeigen weiter, dass es keinen signifikanten Zusammenhang der CFF mit den retinalen Schichtdicken gibt. Dies weist darauf hin, dass eine neuroaxonale Schädigung der Netzhaut keinen signifikanten Einfluss auf die CFF bei MS-Patienten hat. Um andere Einflussfaktoren zu ermitteln, sollten MRT-Parameter hinzugezogen sowie eine Langzeitbeobachtung durchgeführt werden. [26]

Die Ergebnisse dieser Arbeit leisten insgesamt einen wertvollen Beitrag für die Nutzung retinaler OCT in der neurologischen Forschung und können so deren Translation in die klinische Routine unterstützen.

---

[5]betrifft SAMIRIX, OCT-Marker, OCT-Framework

6 Literaturverzeichnis

[1] Anat London, Inbal Benhar und Michal Schwartz. „The retina as a window to the brain—from eye research to CNS disorders". In: *Nature Reviews Neurology* 9.1 (2013), S. 44. DOI: 10.1038/nrneurol.2012.227.

[2] Hanna G Zimmermann, Alexander U Brandt und Friedemann Paul. „Optische Kohärenztomografie in der Neurologie–Methodik und Anwendung in Forschung und Klinik". In: *Klinische Neurophysiologie* 48.04 (2017), S. 211–225. DOI: 10.1055/s-0043-118781.

[3] Frederike C. Oertel, Hanna G. Zimmermann, Alexander U. Brandt und Friedemann Paul. „Novel uses of retinal imaging with optical coherence tomography in multiple sclerosis". In: *Expert Review of Neurotherapeutics* 19.1 (2019). PMID: 30587061, S. 31–43. DOI: 10.1080/14737175.2019.1559051.

[4] Timm Oberwahrenbrock, Ghislaine L. Traber, Sebastian Lukas, Iñigo Gabilondo, Rachel Nolan, Christopher Songster, Lisanne Balk, Axel Petzold, Friedemann Paul, Pablo Villoslada, Alexander U. Brandt, Ari J. Green und Sven Schippling. „Multicenter reliability of semiautomatic retinal layer segmentation using OCT". In: *Neurology - Neuroimmunology Neuroinflammation* 5.3 (2018). DOI: 10.1212/NXI.0000000000000449.

[5] Claudia F. Lucchinetti Daniel S. Reich und Peter A. Calabresi. „Multiple Sclerosis". In: *New England Journal of Medicine* 378 (2018), S. 169–180. DOI: 10.1056/nejmra1401483.

[6] Stefan M Gold, Anne Willing, Frank Leypoldt, Friedemann Paul und Manuel A Friese. „Sex differences in autoimmune disorders of the central nervous system". In: *Seminars in immunopathology*. Bd. 41. 2. Springer. 2019, S. 177–188. DOI: 10.1007/s00281-018-0723-8.

[7] Nadja Borisow, Andrea Döring, Caspar F Pfueller, Friedemann Paul, Jan Dörr und Kerstin Hellwig. „Expert recommendations to personalization of medical approaches in treatment of multiple sclerosis: an overview of family planning and pregnancy". In: *EPMA Journal* 3.1 (2012), S. 9. DOI: 10.1186/1878-5085-3-9.

[8] Markus Bock, Alexander U Brandt, Jan Dörr, Helga Kraft, Nicholetta Weinges-Evers, Gunnar Gaede, Caspar F Pfueller, Katja Herges, Helena Radbruch, Stephanie Ohlraun, Judith Bellmann-Strobl, Jörn Kuchenbecker, Frauke Zipp und Friedemann Paul. „Patterns of retinal nerve fiber layer loss in multiple sclerosis patients with or without optic neuritis and glaucoma patients". In: *Clinical neurology and neurosurgery* 112.8 (2010), S. 647–652. DOI: 10.1016/j.clineuro.2010.04.014.

[9] Hanna G Zimmermann, Benjamin Knier, Timm Oberwahrenbrock, Janina Behrens, Catherina Pfuhl, Lilian Aly, Miriam Kaminski, Muna-Miriam Hoshi, Svenja Specovius, René M Giess, Michael Scheel, Mark Mühlau, Judith Bellmann-Strobl, Klemens Ruprecht, Bernhard Hemmer, Thomas Korn, Friedemann Paul und Alexander U Brandt. „Association of retinal ganglion cell layer thickness with future disease activity in patients with clinically isolated syndrome". In: *JAMA neurology* 75.9 (2018), S. 1071–1079. DOI: 10.1001/jamaneurol.2018.1011.

[10] Axel Petzold, Laura J Balcer, Peter A Calabresi, Fiona Costello, Teresa C Frohman, Elliot M Frohman, Elena H Martinez-Lapiscina, Ari J Green, Randy Kardon, Olivier Outteryck, Friedemann Paul, Sven Schippling, Patrik Vermersch, Pablo Villoslada und Lisanne J Balk. „Retinal layer segmentation in multiple sclerosis: a systematic review and meta-analysis". In: *The Lancet Neurology* 16.10 (2017), S. 797–812. DOI: 10.1016/S1474-4422(17)30278-8.

[11] Kerstin Soelberg, Svenja Specovius, Hanna G Zimmermann, Jakob Grauslund, Jesper J Mehlsen, Clement Olesen, Allan SB Neve, Friedemann Paul, Alexander U Brandt und Nasrin Asgari. „Optical coherence tomography in acute optic neuritis: A population-based study". In: *Acta Neurologica Scandinavica* 138.6 (2018), S. 566–573. DOI: 10.1111/ane.13004.

[12] Vanda A Lennon, Dean M Wingerchuk, Thomas J Kryzer, Sean J Pittock, Claudia F Lucchinetti, Kazuo Fujihara, Ichiro Nakashima und Brian G Weinshenker. „A serum autoantibody marker of neuromyelitis optica: distinction from multiple sclerosis". In: *The Lancet* 364.9451 (2004), S. 2106–2112. DOI: 10.1016/S0140-6736(04)17551-X.

[13] Frederike C Oertel, Hanna Zimmermann, Friedemann Paul und Alexander U Brandt. „Optical coherence tomography in neuromyelitis optica spectrum disorders: potential advantages for individualized monitoring of progression and therapy". In: *EPMA Journal* 9.1 (2018), S. 21–33. DOI: 10.1007/s13167-017-0123-5.

[14] JL Bennett, J De Seze, M Lana-Peixoto, J Palace, A Waldman, S Schippling, S Tenembaum, B Banwell, B Greenberg, M Levy, K Fujihara, KH Chan, HJ Kim, N Asgari, DK Sato, A Saiz, J Wuerfel, H Zimmermann, A Green, P Villoslada, F Paul und GJCF-ICC&BR. „Neuromyelitis optica and multiple sclerosis: seeing differences through optical coherence tomography". In: *Multiple Sclerosis Journal* 21.6 (2015), S. 678–688. DOI: 10.1177/1352458514567216.

[15] Philipp Albrecht, Christine Blasberg, Marius Ringelstein, Ann-Kristin Müller, David Finis, Rainer Guthoff, Ella-Maria Kadas, Wolf Lagreze, Orhan Aktas, Hans-Peter Hartung, Friedemann Paul, Alexander U. Brandt und Axel Methner. „Optical coherence tomography for the diagnosis and monitoring of idiopathic intracranial hypertension". In: *Journal of neurology* 264.7 (2017), S. 1370–1380. DOI: `10.1007/s00415-017-8532-x`.

[16] Falko Kaufhold, Ella Maria Kadas, Christoph Schmidt, Hagen Kunte, Jan Hoffmann, Hanna Zimmermann, Timm Oberwahrenbrock, Lutz Harms, Konrad Polthier, Alexander U Brandt und Friedemann Paul. „Optic nerve head quantification in idiopathic intracranial hypertension by spectral domain OCT". In: *PLoS One* 7.5 (2012), e36965. DOI: `10.1371/journal.pone.0036965`.

[17] James G Fujimoto. „Optical coherence tomography for ultrahigh resolution in vivo imaging". In: *Nature biotechnology* 21.11 (2003), S. 1361–1367. DOI: `10.1038/nbt892`.

[18] Markus Bock, Alexander Ulrich Brandt, Jan Dörr, Caspar F Pfueller, Stephanie Ohlraun, Frauke Zipp und Friedemann Paul. „Time domain and spectral domain optical coherence tomography in multiple sclerosis: a comparative cross-sectional study". In: *Multiple Sclerosis Journal* 16.7 (2010), S. 893–896. DOI: `10.1177/1352458510365156`.

[19] Jennifer B Fisher, Dina A Jacobs, Clyde E Markowitz, Steven L Galetta, Nicholas J Volpe, M Ligia Nano-Schiavi, Monika L Baier, Elliot M Frohman, Heather Winslow, Teresa C Frohman, Peter A Calabresi, Maureen G Maguire, Gary R Cutter und Laura J Balcer. „Relation of visual function to retinal nerve fiber layer thickness in multiple sclerosis." In: *Ophthalmology* 113.2 (Feb. 2006), S. 324–332. DOI: `10.1016/j.ophtha.2005.10.040`.

[20] Kay Gawlik, Frank Hausser, Friedemann Paul, Alexander Ulrich Brandt und Ella Maria Kadas. „Active contour method for ILM segmentation in ONH volume scans in retinal OCT". In: *Biomed. Opt. Express* 9.12 (Dez. 2018), S. 6497–6518. DOI: `10.1364/BOE.9.006497`.

[21] Prejaas Tewarie, Lisanne Balk, Fiona Costello, Ari Green, Roland Martin, Sven Schippling und Axel Petzold. „The OSCAR-IB consensus criteria for retinal OCT quality assessment". In: *PloS one* 7.4 (2012), e34823. DOI: `10.1371/journal.pone.0034823`.

[22] S. Schippling, L. Balk, F. Costello, P. Albrecht, L. Balcer, P. Calabresi, J. Frederiksen, E. Frohman, A. Green, A. Klistorner, O. Outteryck, F. Paul, G. Plant, G. Traber, P. Vermersch, P. Villoslada, S. Wolf und A. Petzold. „Quality control for retinal OCT in multiple sclerosis: validation of the OSCAR-IB criteria". In: *Multiple sclerosis journal* 21.2 (2015), S. 163–170. DOI: `10.1177/1352458514538110`.

[23] Sunil Kumar Yadav, Ella Maria Kadas, Seyedamirhosein Motamedi, Konrad Polthier, Frank Haußer, Kay Gawlik, Friedemann Paul und Alexander Ulrich Brandt. „Optic nerve head three-dimensional shape analysis". In: *Journal of Biomedical Optics* 23 (2018), S. 23 - 23 –13. DOI: `10.1117/1.JBO.23.10.106004`.

[24] S Motamedi, FC Oertel, S Yadav, N Siebert, J Bellmann-Strobl, K Ruprecht, EM Kadas, F Paul, HG Zimmermann und AU Brandt. „Altered optic nerve head morphology in aquaporin-4 igg seropositive neuromyelitis optica". In: Bd. 25. 2019, S. 484–485.

[25] Seyedamirhosein Motamedi, Kay Gawlik, Noah Ayadi, Hanna Gwendolyn Zimmermann, Susanna Asseyer, Charlotte Bereuter, Janine Mikolajczak, Friedemann Paul, Ella Maria Kadas und Alexander Ulrich Brandt. „Normative data and minimally detectable change for inner retinal layer thicknesses using a semi-automated OCT image segmentation pipeline". In: *Frontiers in Neurology* 10 (2019), S. 1117. DOI: `10.3389/fneur.2019.01117`.

[26] Noah Ayadi, Jan Dörr, Seyedamirhosein Motamedi, Kay Gawlik, Judith Bellmann-Strobl, Janine Mikolajczak, Alexander Ulrich Brandt, Hanna Gwendolyn Zimmermann und Friedemann Paul. „Temporal visual resolution and disease severity in MS". In: *Neurology - Neuroimmunology Neuroinflammation* 5 (Sep. 2018), e492. DOI: `10.1212/NXI.0000000000000492`.

[27] Tony F Chan und Luminita A Vese. „Active contours without edges". In: *IEEE Transactions on image processing* 10.2 (2001), S. 266–277. DOI: `10.1109/83.902291`.

[28] Li Wang, Chunming Li, Quan-Sen Sun, De-Shen Xia und Chiu-Yen Kao. „Active contours driven by local and global intensity fitting energy with application to brain MR image segmentation." In: *Comp. Med. Imag. and Graph.* 33.7 (2009), S. 520–531. DOI: `10.1016/j.compmedimag.2009.04.010`.

[29] Mona K Garvin, Michael D Abràmoff, Randy Kardon, Stephen R Russell, Xiaodong Wu und Milan Sonka. „Intraretinal layer segmentation of macular optical coherence tomography images using optimal 3-D graph search". In: *IEEE transactions on medical imaging* 27.10 (2008), S. 1495–1505. DOI: `10.1109/tmi.2008.923966`.

[30] Sunil Yadav, Ulrich Reitebuch und Konrad Polthier. „Robust and High Fidelity Mesh Denoising". In: *IEEE Transactions on Visualization and Computer Graphics* PP (Apr. 2018). DOI: 10.1109/TVCG.2018.2828818.

[31] Sunil Yadav, Konrad Polthier und Ulrich Reitebuch. „Mesh Denoising Based on Normal Voting Tensor and Binary Optimization". In: *IEEE Transactions on Visualization and Computer Graphics* 24 (Juli 2016). DOI: 10.1109/TVCG.2017.2740384.

[32] Andrew Lang, Aaron Carass, Matthew Hauser, Elias S Sotirchos, Peter A Calabresi, Howard S Ying und Jerry L Prince. „Retinal layer segmentation of macular OCT images using boundary classification". In: *Biomedical optics express* 4.7 (2013), S. 1133–1152. DOI: 10.1364/BOE.4.001133.

[33] Mohammad Saleh Miri, Victor A Robles, Michael D Abràmoff, Young H Kwon und Mona K Garvin. „Multimodal graph-theoretic approach for segmentation of the internal limiting membrane at the optic nerve head". In: (2015). DOI: 10.17077/omia.1027.

[34] Andrew Lang, Aaron Carass, Elias Sotirchos, Peter Calabresi und Jerry L Prince. „Segmentation of retinal OCT images using a random forest classifier". In: *Medical Imaging 2013: Image Processing*. Bd. 8669. International Society for Optics und Photonics. 2013, 86690R. DOI: 10.1117/12.2006649.

[35] S. Specovius, H. G. Zimmermann, C. Chien, F. C. Oertel, L. Cooke, E. H. Martinez-Lapiscina, M. A. Lana-Peixoto, M. A. Fontenelle, J. Palaces, A. Roca-Fernandez, A. Rubio Diaz, M. I. Leiter, S. M. Sharma, S. Siritho, A. Altintas, R. Yildirim, U. Tanriverdi, A. Jacob, S. Huda, R. Marignier, E. Nerrant, A. Cobo-Calvo, J. de Seze, T. Senger, L. Pandit, A. Dcunha, I. Soto de Castillo, D. Bichuetti, I. Maynart Tavares, E. F. May, C. Tongco, J. Havla, L. Leocani, M. Pisa, M. Radaelli, O. Aktas, M. Ringelstein, J. Rybak, P. Albrecht, H. J. Kim, J. -W. Hyun, N. Asgari, K. Soelberg, Y. Mao-Draayer, H. Stiebel-Kalish, I. Kister, Z. Rimler, A. Reid, A. U. Brandt, F. Paul und GJCF-ICC. „The CROCTINO project: an international retrospective multi-center study of retinal optical coherence tomography in 501 patients with neuromyelitis optica spectrum disorders". In: Bd. 24. Suppl. 2. 34th Congress of the European-Committee-for-Treatment-and-Research-in-Multiple-Sclerosis (ECTRIMS), Berlin, GERMANY, OCT 10-12, 2018; Conference date: 10-10-2018 Through 12-10-2018. SAGE Publications, Okt. 2018, S. 642–644.

[36] F. C. Oertel, S. Specovius, H. G. Zimmermann, C. Chien, S. Motamedi, L. Cook, E. H. Martinez-Lapiscina, M. A. Lana Peixoto, M. A. Fontenelle, J. Palace, A. Roca-Fernandez, S. Siritho, A. Altintas, U. Tanriverdi, A. Jacob, S. Huda, R. Marignier, E. Nerrant, A. Cobo Calvo, J. de Seze, T. Senger, L. Pandit, A. Dcunha, I. S. de Castillo, D. Bichuetti, M. Tavares, E. F. May, C. Tongco, J. Havla, L. Leocani, M. Pisa, F. Ashtari, R. Kafieh, O. Aktas, M. Ringelstein, P. Albrecht, H. J. Kim, J. -W. Hyun, N. Asgari, K. Soelberg, Y. Mao-Draayer, H. Stiebel-Kalish, Z. Rimler, A. Reid, M. Yeaman, T. J. Smith, A. U. Brandt, F. Paul und GJCF Int Clinical Consortium NMOSD. „An international retrospective multi-center study of retinal optical coherence tomography in neuromyelitis optica spectrum disorders: the CROCTINO study". In: Bd. 25. 2 Suppl. 1. 35th Congress of the European-Committee-for-Treatment-and-Research-in-Multiple-Sclerosis (ECTRIMS) / 24th Annual Conference of Rehabilitation in MS, Stockholm, SWEDEN, SEP 11-13, 2019; Conference date: 11-09-2019 Through 13-09-2019. SAGE Publications, Sep. 2019, S. 709–711. DOI: 10.1177/1352458519868081.

[37] Svenja Specovius, Hanna G Zimmermann, Frederike Cosima Oertel, Claudia Chien, Charlotte Bereuter, Lawrence J Cook, Marco Aurélio Lana Peixoto, Mariana Andrade Fontenelle, Ho Jin Kim, Jae-Won Hyun, Su-Kyung Jung, Jacqueline Palace, Adriana Roca-Fernandez, Alejandro Rubio Diaz, Maria Isabel Leite, Srilakshmi M Sharma, Fereshte Ashtari, Rahele Kafieh, Alireza Dehghani, Mohsen Pourazizi, Lekha Pandit, Anitha Dcunha, Orhan Aktas, Marius Ringelstein, Philipp Albrecht, Eugene May, Caryl Tongco, Letizia Leocani, Marco Pisa, Marta Radaelli, Elena H Martinez-Lapiscina, Hadas Stiebel-Kalish, Mark Hellmann, Itay Lotan, Sasitorn Siritho, Jérôme de Seze, Thomas Senger, Joachim Havla, Romain Marignier, Caroline Tilikete, Alvaro Cobo Calvo, Denis Bernardi Bichuetti, Ivan Maynart Tavares, Nasrin Asgari, Kerstin Soelberg, Ayse Altintas, Rengin Yildirim, Uygur Tanriverdi, Anu Jacob, Saif Huda, Zoe Rimler, Allyson Reid, Yang Mao-Draayer, Ibis Soto de Castillo, Michael R Yeaman, Terry J Smith, Alexander U Brandt und Friedemann Paul. „Cohort profile: a collaborative multicentre study of retinal optical coherence tomography in 539 patients with neuromyelitis optica spectrum disorders (CROCTINO)". In: *BMJ Open* 10.10 (2020). ISSN: 2044-6055. DOI: 10.1136/bmjopen-2019-035397.

[38] Mehreen Adhi, Sumbul Aziz, Kashif Muhammad und Mohammad I Adhi. „Macular thickness by age and gender in healthy eyes using spectral domain optical coherence tomography". In: *PLoS One* 7.5 (2012), e37638. DOI: 10.1371/journal.pone.0037638.

Eidesstattliche Versicherung

„Ich, Kay Gawlik, versichere an Eides statt durch meine eigenhändige Unterschrift, dass ich die vorgelegte Dissertation mit dem Thema: »Neue Methoden der Nachbearbeitung und Analyse retinaler optischer Kohärenztomografieaufnahmen bei neurologischen Erkrankungen«/»New methods of postprocessing and analysis of retinal optical coherence tomography images in neurological neurological diseases« selbstständig und ohne nicht offengelegte Hilfe Dritter verfasst und keine anderen als die angegebenen Quellen und Hilfsmittel genutzt habe. Alle Stellen, die wörtlich oder dem Sinne nach auf Publikationen oder Vorträgen anderer Autoren/innen beruhen, sind als solche in korrekter Zitierung kenntlich gemacht. Die Abschnitte zu Methodik (insbesondere praktische Arbeiten, Laborbestimmungen, statistische Aufarbeitung) und Resultaten (insbesondere Abbildungen, Graphiken und Tabellen) werden von mir verantwortet.

Meine Anteile an etwaigen Publikationen zu dieser Dissertation entsprechen denen, die in der untenstehenden gemeinsamen Erklärung mit dem Erstbetreuer, angegeben sind. Für sämtliche im Rahmen der Dissertation entstandenen Publikationen wurden die Richtlinien des ICMJE (International Committee of Medical Journal Editors; www.icmje.og) zur Autorenschaft eingehalten. Ich erkläre ferner, dass ich mich zur Einhaltung der Satzung der Charité – Universitätsmedizin Berlin zur Sicherung Guter Wissenschaftlicher Praxis verpflichte.

Weiterhin versichere ich, dass ich diese Dissertation weder in gleicher noch in ähnlicher Form bereits an einer anderen Fakultät eingereicht habe.

Die Bedeutung dieser eidesstattlichen Versicherung und die strafrechtlichen Folgen einer unwahren eidesstattlichen Versicherung (§§156, 161 des Strafgesetzbuches) sind mir bekannt und bewusst."

_____   _____

Berlin, 18. Februar 2021   Kay Gawlik

Ort, Datum

Anteilserklärung an den erfolgten Publikationen

Kay Gawlik hatte folgenden Anteil an den folgenden Publikationen:

Publikation 1: ONH-ILM-Segmentierung [20]

Titel	Active contour method for ILM segmentation in ONH volume scans in retinal OCT
Autoren	**Kay Gawlik**, Frank Haußer, Friedemann Paul, Alexander U. Brandt, Ella Maria Kadas
Veröffentlicht in	Biomedical Optics Express, 2018 *Impact Factor: 3.910*

Beitrag im Einzelnen:

- Konzeption der Segmentierungsstrategie und Implementierung aller verwendeten Bildverarbeitungsalgorithmen sowie Anpassung für OCT-ONH-Aufnahmen

- Entwicklung der Visualisierungkomponente und Analysierung des Segmentierungsverlaufes

- Erstellung des GUI-Programmes (OCT-Marker) für die manuelle Segmentierung und Durchführung dieser

- Implementierung des Optimierungsframeworks sowie Durchführung und Auswertung der Optimierung

- Auswertung der Ergebnisse und Durchführung aller statistischen Analysen mit Ausnahme der Wilcoxon-Signed-Rank-Tests

- Erstellung sämtlicher Grafiken, Verfassen von Teilen des Manuskripts

Publikation 2: ONH-Morphometrie [23]

Titel	Optic nerve head three-dimensional shape analysis
Autoren	Sunil Kumar Yadav, Ella Maria Kadas, Seyedamirhosein Motamedi, Konrad Polthier, Frank Haußer, **Kay Gawlik**, Friedemann Paul, Alexander Brandt
Veröffentlicht in	Journal of Biomedical Optics, 2018 *Impact Factor: 2.555*

Beitrag im Einzelnen:

- Anpassung des ONH-ILM-Segmentierungsalgorithmus (siehe Abschnitt 2.4) für Batch-Verarbeitung

- Integration des Marching-Cube-Algorithmus in der ONH-ILM-Segmentierung zur Extraktion der ILM als triangulierte 3D-Fläche

- Implementierung des Exportes der triangulierten ILM im STL-Format für die Weiterverarbeitung

- Kritisches Gegenlesen des Manuskripts

Publikation 3: SAMIRIX und normative Datenbank [25]

Titel	Normative data and minimally detectable change for inner retinal layer thicknesses using a semi-automated OCT image segmentation pipeline
Autoren	Seyedamirhosein Motamedi, **Kay Gawlik**, Noah Ayadi, Hanna G. Zimmermann, Susanna Asseyer, Charlotte Bereuter, Janine Mikolajczak, Friedemann Paul, Ella-Maria Kadas, Alexander Ulrich Brandt
Veröffentlicht in	Frontiers in Neurology, 2019 *Impact Factor: 2.889*

Beitrag im Einzelnen:

- Konzeption und Implementierung der manuellen Nachkorrektur innerhalb vom GUI-Programm OCT-Marker (siehe Abschnitt 2.3.2)
  - Einbau des PCIP-Algorithmus und Entwicklung der Spline-Reapproximation aus den diskreten Segmentierungspunkten
- Konzeption und Entwicklung der OCT-Marker-Schnittstellen für den Datenaustausch mit SAMIRIX
- Entwurf und Umsetzung einer speziell für SAMIRIX angepassten Benutzungsoberfläche
- Kritisches Gegenlesen des Manuskripts

Publikation 4: Assoziation der retinalen Schichtdicken mit der kritischen Flimmerfrequenz [26]

Titel	Temporal visual resolution and disease severity in MS
Autoren	Noah Ayadi, Jan Dörr, Seyedamirhosein Motamedi, **Kay Gawlik**, Judith Bellmann-Strobl, Janine Mikolajczak, Alexander U. Brandt, Hanna Zimmermann, Friedemann Paul
Veröffentlicht in	Neurology: Neuroimmunology & Neuroinflammation MS, 2018 *Impact Factor: 7.353*

Beitrag im Einzelnen:

- Unterstützung der OCT-Daten-Analyse mittels SAMIRIX/des OCT-Markers
- Schulung zur Benutzung des OCT-Markers
- Anpassungen und Fehlerbehebungen beim OCT-Marker
- Kritisches Gegenlesen des Manuskripts

_____

Unterschrift, Datum und Stempel des betreuenden Hochschullehrers

_____

Unterschrift des Doktoranden

Druckexemplare der ausgewählten Publikationen

Active contour method for ILM segmentation in ONH volume scans in retinal OCT

KAY GAWLIK,[1,2] FRANK HAUSSER,[1] FRIEDEMANN PAUL,[2,3] ALEXANDER U. BRANDT,[2,4,*] AND ELLA MARIA KADAS[2]

[1]*Beuth-Hochschule für Technik Berlin - University of Applied Sciences, Berlin, Germany*
[2]*NeuroCure Clinical Research Center, Charité - Universitätsmedizin Berlin, corporate member of Freie Universität Berlin, Humboldt-Universität zu Berlin, and Berlin Institute of Health, Berlin, Germany*
[3]*Experimental and Clinical Research Center, Max Delbrück Center for Molecular Medicine and Charité - Universitätsmedizin Berlin, Germany*
[4]*Department of Neurology, University of California Irvine, CA, USA*
[*]*Corresponding author: alexander.brandt@charite.de*

Abstract: The optic nerve head (ONH) is affected by many neurodegenerative and autoimmune inflammatory conditions. Optical coherence tomography can acquire high-resolution 3D ONH scans. However, the ONH's complex anatomy and pathology make image segmentation challenging. This paper proposes a robust approach to segment the inner limiting membrane (ILM) in ONH volume scans based on an active contour method of Chan-Vese type, which can work in challenging topological structures. A local intensity fitting energy is added in order to handle very inhomogeneous image intensities. A suitable boundary potential is introduced to avoid structures belonging to outer retinal layers being detected as part of the segmentation. The average intensities in the inner and outer region are then rescaled locally to account for different brightness values occurring among the ONH center. The appropriate values for the parameters used in the complex computational model are found using an optimization based on the differential evolution algorithm. The evaluation of results showed that the proposed framework significantly improved segmentation results compared to the commercial solution.

References and links

1. A. London, I. Benhar, and M. Schwartz, "The retina as a window to the brain—from eye research to CNS disorders," Nat. Rev. Neurol. **9**, 44–53 (2012).
2. T. Oberwahrenbrock, M. Ringelstein, S. Jentschke, K. Deuschle, K. Klumbies, J. Bellmann-Strobl, J. Harmel, K. Ruprecht, S. Schippling, H.-P. Hartung, O. Aktas, A. U. Brandt, and F. Paul, "Retinal ganglion cell and inner plexiform layer thinning in clinically isolated syndrome," Multiple Scler. J. **19**, 1887–1895 (2013).
3. T. Oberwahrenbrock, S. Schippling, M. Ringelstein, F. Kaufhold, H. Zimmermann, N. Keser, K. L. Young, J. Harmel, H.-P. Hartung, R. Martin, F. Paul, O. Aktas, and A. U. Brandt, "Retinal damage in multiple sclerosis disease subtypes measured by high-resolution optical coherence tomography," Multiple Scler. Int. **2012**, 530305 (2012).
4. E. Schneider, H. Zimmermann, T. Oberwahrenbrock, F. Kaufhold, E. M. Kadas, A. Petzold, F. Bilger, N. Borisow, S. Jarius, B. Wildemann, K. Ruprecht, A. U. Brandt, and F. Paul, "Optical coherence tomography reveals distinct patterns of retinal damage in neuromyelitis optica and multiple sclerosis," PLOS ONE **8**, 1–10 (2013).
5. F. C. Oertel, J. Kuchling, H. Zimmermann, C. Chien, F. Schmidt, B. Knier, J. Bellmann-Strobl, T. Korn, M. Scheel, A. Klistorner, K. Ruprecht, F. Paul, and A. U. Brandt, "Microstructural visual system changes in AQP4-antibody–seropositive NMOSD," Neurol. - Neuroimmunol. Neuroinflammation **4**, e334 (2017).
6. F. C. Oertel, H. Zimmermann, J. Mikolajczak, M. Weinhold, E. M. Kadas, T. Oberwahrenbrock, F. Pache, J. Bellmann-Strobl, K. Ruprecht, F. Paul, and A. U. Brandt, "Contribution of blood vessels to retinal nerve fiber layer thickness in NMOSD," Neurol. - Neuroimmunol. Neuroinflammation **4**, e338 (2017).
7. M. Ringelstein, P. Albrecht, I. Kleffner, B. Bühn, J. Harmel, A.-K. Müller, D. Finis, R. Guthoff, R. Bergholz, T. Duning, M. Krämer, F. Paul, A. Brandt, T. Oberwahrenbrock, J. Mikolajczak, B. Wildemann, S. Jarius, H.-P. Hartung, O. Aktas, and J. Dörr, "Retinal pathology in susac syndrome detected by spectral-domain optical coherence tomography," Neurology **85**, 610–618 (2015).

8. A. U. Brandt, T. Oberwahrenbrock, F. Costello, M. Fielden, K. Gertz, I. Kleffner, F. Paul, R. Bergholz, and J. Dörr, "Retinal lesion evolution in Susac syndrome," Retina **36**, 366–374 (2016).

9. N. M. Roth, S. Saidha, H. Zimmermann, A. U. Brandt, J. Isensee, A. Benkhellouf-Rutkowska, M. Dornauer, A. A. Kühn, T. Müller, P. A. Calabresi, and F. Paul, "Photoreceptor layer thinning in idiopathic Parkinson's disease," Mov. Disord. **29**, 1163–1170 (2014).

10. C. Y. lui Cheung, M. K. Ikram, C. Chen, and T. Y. Wong, "Imaging retina to study dementia and stroke," Prog. Retin. Eye Res. **57**, 89–107 (2017).

11. D. Huang, E. Swanson, C. Lin, J. Schuman, W. Stinson, W. Chang, M. Hee, T. Flotte, K. Gregory, C. Puliafito, and J. G. Fujimoto, "Optical coherence tomography," Science **254**, 1178–1181 (1991).

12. M. Bock, A. U. Brandt, J. Dörr, C. F. Pfueller, S. Ohlraun, F. Zipp, and F. Paul, "Time domain and spectral domain optical coherence tomography in multiple sclerosis: a comparative cross-sectional study," Multiple Scler. J. **16**, 893–896 (2010).

13. A. Lang, A. Carass, M. Hauser, E. S. Sotirchos, P. A. Calabresi, H. S. Ying, and J. L. Prince, "Retinal layer segmentation of macular OCT images using boundary classification," Biomed. Opt. Express **4**, 1133 (2013).

14. A. Petzold, L. J. Balcer, P. A. Calabresi, F. Costello, T. C. Frohman, E. M. Frohman, E. H. Martinez-Lapiscina, A. J. Green, R. Kardon, O. Outteryck, F. Paul, S. Schippling, P. Vermersch, P. Villoslada, L. J. Balk, O. Aktas, P. Albrecht, J. Ashworth, N. Asgari, G. Black, D. Boehringer, R. Behbehani, L. Benson, R. Bermel, J. Bernard, A. Brandt, J. Burton, J. Calkwood, C. Cordano, A. Courtney, A. Cruz-Herranz, R. Diem, A. Daly, H. Dollfus, C. Fasser, C. Finke, J. Frederiksen, E. Garcia-Martin, I. G. Suárez, G. Pihl-Jensen, J. Graves, J. Havla, B. Hemmer, S.-C. Huang, J. Imitola, H. Jiang, D. Keegan, E. Kildebeck, A. Klistorner, B. Knier, S. Kolbe, T. Korn, B. LeRoy, L. Leocani, D. Leroux, N. Levin, P. Liskova, B. Lorenz, J. L. Preiningerova, J. Mikolajczak, X. Montalban, M. Morrow, R. Nolan, T. Oberwahrenbrock, F. C. Oertel, C. Oreja-Guevara, B. Osborne, A. Papadopoulou, M. Ringelstein, S. Saidha, B. Sanchez-Dalmau, J. Sastre-Garriga, R. Shin, N. Shuey, K. Soelberg, A. Toosy, R. Torres, A. Vidal-Jordana, A. Waldman, O. White, A. Yeh, S. Wong, and H. Zimmermann, "Retinal layer segmentation in multiple sclerosis: a systematic review and meta-analysis," The Lancet Neurol. **16**, 797–812 (2017).

15. E. H. Martinez-Lapiscina, S. Arnow, J. A. Wilson, S. Saidha, J. L. Preiningerova, T. Oberwahrenbrock, A. U. Brandt, L. E. Pablo, S. Guerrieri, I. Gonzalez, O. Outteryck, A.-K. Mueller, P. Albrecht, W. Chan, S. Lukas, L. J. Balk, C. Fraser, J. L. Frederiksen, J. Resto, T. Frohman, C. Cordano, I. Zubizarreta, M. Andorra, B. Sanchez-Dalmau, A. Saiz, R. Bermel, A. Klistorner, A. Petzold, S. Schippling, F. Costello, O. Aktas, P. Vermersch, C. Oreja-Guevara, G. Comi, L. Leocani, L. Garcia-Martin, F. Paul, E. Havrdova, E. Frohman, L. J. Balcer, A. J. Green, P. A. Calabresi, and P. Villoslada, "Retinal thickness measured with optical coherence tomography and risk of disability worsening in multiple sclerosis: a cohort study," The Lancet Neurol. **15**, 574–584 (2016).

16. A. Cruz-Herranz, L. J. Balk, T. Oberwahrenbrock, S. Saidha, E. H. Martinez-Lapiscina, W. A. Lagreze, J. S. Schuman, P. Villoslada, P. Calabresi, L. Balcer, A. Petzold, A. J. Green, F. Paul, A. U. Brandt, and P. Albrecht, "The APOSTEL recommendations for reporting quantitative optical coherence tomography studies," Neurology. **86**, 2303–2309 (2016).

17. T. C. Chen, "Spectral domain optical coherence tomography in glaucoma: Qualitative and quantitative analysis of the optic nerve head and retinal nerve fiber layer (an AOS thesis)," Transactions Am. Ophthalmol. Soc. **107**, 254–281 (2009).

18. F. Pollet-Villard, C. Chiquet, J.-P. Romanet, C. Noel, and F. Aptel, "Structure-function relationships with spectral-domain optical coherence tomography retinal nerve fiber layer and optic nerve head measurements structure-function relationships with SD-OCT," Investig. Ophthalmol. Vis. Sci. **55**, 2953 (2014).

19. B. C. Chauhan, V. M. Danthurebandara, G. P. Sharpe, S. Demirel, C. A. Girkin, C. Y. Mardin, A. F. Scheuerle, and C. F. Burgoyne, "Bruch's membrane opening minimum rim width and retinal nerve fiber layer thickness in a normal white population," Ophthalmology. **122**, 1786–1794 (2017).

20. P. Enders, W. Adler, F. Schaub, M. M. Hermann, T. Dietlein, C. Cursiefen, and L. M. Heindl, "Novel Bruch's membrane opening minimum rim area equalizes disc size dependency and offers high diagnostic power for glaucoma," Investig. Opthalmology & Vis. Sci. **57**, 6596 (2016).

21. F. Kaufhold, E. M. Kadas, C. Schmidt, H. Kunte, J. Hoffmann, H. Zimmermann, T. Oberwahrenbrock, L. Harms, K. Polthier, A. U. Brandt, and F. Paul, "Optic nerve head quantification in idiopathic intracranial hypertension by spectral domain OCT," PLOS ONE **7**, 1–6 (2012).

22. P. Albrecht, C. Blasberg, M. Ringelstein, A.-K. Müller, D. Finis, R. Guthoff, E.-M. Kadas, W. Lagreze, O. Aktas, H.-P. Hartung, F. Paul, A. U. Brandt, and A. Methner, "Optical coherence tomography for the diagnosis and monitoring of idiopathic intracranial hypertension," J. Neurol. **264**, 1370–1380 (2017).

23. S. L. Galetta, P. Villoslada, N. Levin, K. Shindler, H. Ishikawa, E. Parr, D. Cadavid, and L. J. Balcer, "Acute optic neuritis," Neurol. - Neuroimmunol. Neuroinflammation **2**, e135 (2015).

24. A. Petzold, M. P. Wattjes, F. Costello, J. Flores-Rivera, C. L. Fraser, K. Fujihara, J. Leavitt, R. Marignier, F. Paul, S. Schippling, C. Sindic, P. Villoslada, B. Weinshenker, and G. T. Plant, "The investigation of acute optic neuritis: a review and proposed protocol," Nat. Rev. Neurol. **10**, 447–458 (2014).

25. S. B. Syc, C. V. Warner, S. Saidha, S. K. Farrell, A. Conger, E. R. Bisker, J. Wilson, T. C. Frohman, E. M. Frohman, L. J. Balcer, and P. A. Calabresi, "Cup to disc ratio by optical coherence tomography is abnormal in multiple sclerosis," J. Neurolog. Sci. **302**, 19–24 (2011).

26. A. Shah, J. K. Wang, M. K. Garvin, M. Sonka, and X. Wu, "Automated surface segmentation of internal limiting

membrane in spectral-domain optical coherence tomography volumes with a deep cup using a 3D range expansion approach," in *2014 IEEE 11th International Symposium on Biomedical Imaging (ISBI)* (2014), pp. 1405–1408.

27. M. S. Miri, V. A. Robles, M. D. Abràmoff, Y. H. Kwon, and M. K. Garvin, "Incorporation of gradient vector flow field in a multimodal graph-theoretic approach for segmenting the internal limiting membrane from glaucomatous optic nerve head-centered SD-OCT volumes," Comput. Med. Imaging Graph. **55**, 87–94 (2017).

28. F. A. Almobarak, N. O'Leary, A. S. C. Reis, G. P. Sharpe, D. M. Hutchison, M. T. Nicolela, and B. C. Chauhan, "Automated segmentation of optic nerve head structures with optical coherence tomography segmentation of optic nerve head structures," Investig. Ophthalmol. Vis. Sci. **55**, 1161 (2014).

29. B. Keller, D. Cunefare, D. S. Grewal, T. H. Mahmoud, J. A. Izatt, and S. Farsiu, "Length-adaptive graph search for automatic segmentation of pathological features in optical coherence tomography images," J. Biomed. Opt. **21**, 076015 (2016).

30. J. Novosel, K. A. Vermeer, J. H. de Jong, Z. Wang, and L. J. van Vliet, "Joint segmentation of retinal layers and focal lesions in 3-D OCT data of topologically disrupted retinas," IEEE Transactions on Med. Imaging **36**, 1276–1286 (2017).

31. J. Novosel, G. Thepass, H. G. Lemij, J. F. de Boer, K. A. Vermeer, and L. J. van Vliet, "Loosely coupled level sets for simultaneous 3D retinal layer segmentation in optical coherence tomography," Med. Image Analysis **26**, 146–158 (2015).

32. J. Novosel, Z. Wang, H. de Jong, K. A. Vermeer, and L. J. van Vliet, "Loosely coupled level sets for retinal layers and drusen segmentation in subjects with dry age-related macular degeneration," in *Medical Imaging 2016: Image Processing,* M. A. Styner and E. D. Angelini, eds. (SPIE, 2016).

33. J. Novosel, Z. Wang, H. de Jong, M. van Velthoven, K. A. Vermeer, and L. J. van Vliet, "Locally-adaptive loosely-coupled level sets for retinal layer and fluid segmentation in subjects with central serous retinopathy," in *2016 IEEE 13th International Symposium on Biomedical Imaging (ISBI)* (IEEE, 2016).

34. A. Carass, A. Lang, M. Hauser, P. A. Calabresi, H. S. Ying, and J. L. Prince, "Multiple-object geometric deformable model for segmentation of macular OCT," Biomed. Opt. Express **5**, 1062 (2014).

35. L. Fang, D. Cunefare, C. Wang, R. H. Guymer, S. Li, and S. Farsiu, "Automatic segmentation of nine retinal layer boundaries in OCT images of non-exudative AMD patients using deep learning and graph search," Biomed. Opt. Express **8**, 2732 (2017).

36. A. G. Roy, S. Conjeti, S. P. K. Karri, D. Sheet, A. Katouzian, C. Wachinger, and N. Navab, "ReLayNet: retinal layer and fluid segmentation of macular optical coherence tomography using fully convolutional networks," Biomed. Opt. Express **8**, 3627 (2017).

37. H. Noh, S. Hong, and B. Han, "Learning deconvolution network for semantic segmentation," in *2015 IEEE International Conference on Computer Vision (ICCV)* (IEEE, 2015).

38. O. Ronneberger, P. Fischer, and T. Brox, "U-net: Convolutional networks for biomedical image segmentation," in *Lecture Notes in Computer Science* (Springer International Publishing, 2015), pp. 234–241.

39. Y. He, A. Carass, Y. Yun, C. Zhao, B. M. Jedynak, S. D. Solomon, S. Saidha, P. A. Calabresi, and J. L. Prince, "Towards topological correct segmentation of macular OCT from cascaded FCNs," in *Fetal, Infant and Ophthalmic Medical Image Analysis* (Springer International Publishing, 2017), pp. 202–209.

40. T. F. Chan and L. A. Vese, "Active contours without edges," IEEE Trans. Image Process. **10**, 266–277 (2001).

41. L. Wang, C. Li, Q.-S. Sun, D.-S. Xia, and C.-Y. Kao, "Active contours driven by local and global intensity fitting energy with application to brain MR image segmentation," Comp. Med. Imag. Graph. **33**, 520-–531 (2009).

42. M. Kass, A. Witkin, and D. Terzopoulos, "Snakes: Active contour models," International Journal of Computer Vision **1**, 321–331 (1988).

43. D. Mumford and J. Shah, "Optimal approximations by piecewise smooth functions and associated variational problems," Commun. Pure Appl. Math. **42**, 577–685 (1989).

44. J. Sethian, "Level Set Methods: An Act of Violence," American Scientist (1997).

45. J. Sethian, *Level Set Methods and Fast Marching Methods: Evolving Interfaces in Computational Geometry, Fluid Mechanics, Computer Vision, and Materials Science*, Cambridge Monographs on Applied and Computational Mathematics (Cambridge University Press, 1999).

46. A. A. Taha and A. Hanbury, "Metrics for evaluating 3D medical image segmentation: analysis, selection, and tool," BMC Med. Imaging **15**, 29 (2015).

47. S. Das, A. Abraham, U. K. Chakraborty, and A. Konar, "Differential Evolution Using a Neighborhood-Based Mutation Operator," IEEE Trans. Evol. Comput. **13**, 526-—553 (2009).

48. C. Jansen, M. Witt, and D. Krefting, *Employing Docker Swarm on OpenStack for Biomedical Analysis* (Springer International Publishing, 2016), p. 303-–318.

49. J. W. Eaton, D. Bateman, S. Hauberg, and R. Wehbring, *GNU Octave version 4.0.0 manual: a high-level interactive language for numerical computations* (2015).

50. R Core Team, *R: A Language and Environment for Statistical Computing*, R Foundation for Statistical Computing, Vienna, Austria (2017).

51. M. K. Garvin, M. D. Abramoff, X. Wu, S. R. Russell, T. L. Burns, and M. Sonka, "Automated 3-d intraretinal layer segmentation of macular spectral-domain optical coherence tomography images," IEEE Transactions on Med. Imaging **28**, 1436–1447 (2009).

52. Z. Hu, M. D. Abràmoff, Y. H. Kwon, K. Lee, and M. K. Garvin, "Automated segmentation of neural canal opening

and optic cup in 3d spectral optical coherence tomography volumes of the optic nerve head," Investig. Ophthalmol. Vis. Sci. **51**, 5708 (2010).

53. K. Lee, M. Niemeijer, M. K. Garvin, Y. H. Kwon, M. Sonka, and M. D. Abràmoff, "Segmentation of the optic disc in 3-D OCT scans of the optic nerve head," IEEE Trans Med Imaging **29**, 159–168 (2010).

54. B. J. Anthony, M. D. Abràmoff, K. Lee, P. Sonkova, P. Gupta, Y. Kwon, M. Neimeijer, Z. Hu, and M. K. Garvin, "Automated 3D segmentation of intraretinal layers from optic nerve head optical coherence tomography images," Proc. SPIE **7626**, 76260 (2010).

55. B. J. Antony, M. S. Miri, M. D. Abràmoff, Y. H. Kwon, and M. K. Garvin, "Automated 3d segmentation of multiple surfaces with a shared hole: Segmentation of the neural canal opening in SD-OCT volumes," Med Image Comput. Comput. Assist. Interv **17**, 739–746 (2014).

56. M. S. Miri, K. Lee, M. Niemeijer, M. D. Abràmoff, Y. H. Kwon, and M. K. Garvin,

    Multimodal segmentation of optic disc and cup from stereo fundus and SD-OCT images, Proc. SPIE **8669**, 86690 (2013).

57. M. S. Miri, M. D. Abràmoff, K. Lee, M. Niemeijer, J. K. Wang, Y. H. Kwon, and M. K. Garvin, "Multimodal segmentation of optic disc and cup from SD-OCT and color fundus photographs using a machine-learning graph-based approach," IEEE Transactions on Med. Imaging **34**, 1854–1866 (2015).

58. B. J. Antony, M. D. Abràmoff, M. M. Harper, W. Jeong, E. H. Sohn, Y. H. Kwon, R. Kardon, and M. K. Garvin, "A combined machine-learning and graph-based framework for the segmentation of retinal surfaces in SD-OCT volumes," Biomed. Opt. Express **4**, 2712 (2013).

59. E. M. Kadas, F. Kaufhold, C. Schulz, F. Paul, K. Polthier, and A. U. Brandt, *3D Optic Nerve Head Segmentation in Idiopathic Intracranial Hypertension* (Springer Berlin Heidelberg, 2012), pp. 262–267.

60. P. Albrecht, C. Blasberg, S. Lukas, M. Ringelstein, A.-K. Müller, J. Harmel, E.-M. Kadas, D. Finis, R. Guthoff, O. Aktas, H.-P. Hartung, F. Paul, A. U. Brandt, P. Berlit, A. Methner, and M. Kraemer, "Retinal pathology in idiopathic moyamoya angiopathy detected by optical coherence tomography," Neurology **85**, 521–527 (2015).

1. Introduction

The eye's retina is part of the central nervous system (CNS) and as such features a similar cellular composition as the brain [1]. Accordingly, many chronic brain conditions lead to retinal changes. For example, retinal alterations have been described in clinically isolated syndrome [2], multiple sclerosis [3], neuromyelitis optica spectrum disorders [4–6], Susac's symdrome [7,8], Parkinson's disease [9], and Alzheimer's dementia [10] .

The retina is the only part of the CNS that is readily accessible by optical imaging, putting great potential into its imaging in the context of these disorders. Currently, spectral domain optical coherence tomography (SD-OCT) is the method of choice to acquire retinal 3D images in μm resolution [11, 12].

The human retina demonstrates two macroscopic landmarks, whose analysis is especially promising in the context of neurological disorders. The *macula* around the fovea is the visual field's center and contains the highest density of retinal ganglion cells. Macular SD-OCT images can be analysed quantitatively with intra-retinal segmentation [13]. The derived thickness or volume changes can then be used to quantify neuro-axonal damage in neurological disorders, e.g. in multiple sclerosis [14–16].

The second landmark is the *optic nerve head (ONH)*, where all axons from retinal ganglion cells leave the eye towards the brain, thereby forming the optic nerve.

Two membranes define the ONH region and limit the ONH towards the inner and outer eye: the inner limiting membrane (ILM) and the Bruch's membrane (BM) (Fig. 1). Segmenting both structures provides an important starting point for calculating imaging biomarkers of the ONH. Yet, development of suitable segmentation approaches is still an active research topic since ONH segmentation presents several difficult challenges for image analysis. An example where the commercial device fails is shown in Fig. 1. At the ONH, ILM segmentation is particularly challenging because of the broad range of ILM topologies in highly swollen to shallow ONH, ONH with deep cupping, and in some cases even with ILM overhangs. Segmentation is further complicated by a dense vasculature with often loose connective tissue, which can cause ILM surfaces with vastly irregular shapes, see Fig. 10.

A simplified ONH parameter is e.g. the peripapillary retinal nerve fiber layer thickness
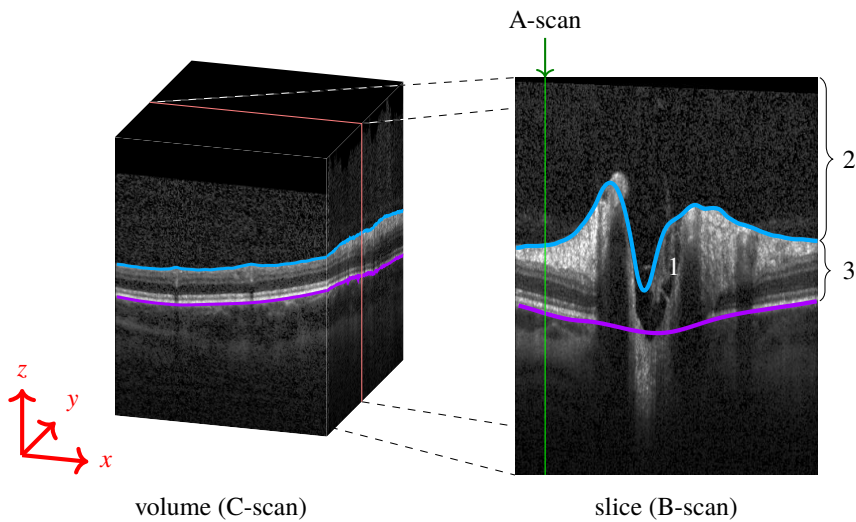
Fig. 1. (Left) Volume scan (C-Scan) of the optic nerve head (ONH). (Right) The volume scan consists of slices (B-scans), where each column is an axial depth scan (A-Scan). The ONH typically has a cup in its center (1). The blue line marks the inner limiting membrane (ILM) separating the vitreous body (2) from retinal tissue (3). The magenta line represents the Bruch's membrane (BM). Note how the blue line failed to correctly detect the ILM, and misses the vessel at the left top, as well as the deep cuping.

(pRNFL), which is measured in a circular scan with 12° diameter around the ONH, thereby avoiding direct ONH analysis. Certainly though, the ONH 3D structure itself contains potentially highly diagnostically relevant information as well, as it e.g. has been shown in glaucoma [17–20]. However, in applications concerning neurological disorders we need not only the minimum distance from the BMO points to the ILM, the so called BMO minimum rim width parameter (BMO-MRW), an already established parameter in the research of glaucoma [17–20], but also several others that incorporate various regions, volumes and areas. These will be able to capture the changes that ONH undergoes in form of swelling, as for example in idiopathic intracranial hypertension [21, 22], as well as in form of atrophy after optic neuritis [23, 24] or other optic neuropathies, for example, in the context of multiple sclerosis [25] or neuromyelitis optica spectrum disorders [5].

1.1. State of the art and proposed solution

One of the most frequently applied methods for retinal layer and ILM segmentation is based on graph-cuts [13], which works nicely in conditions with smooth surfaces, e.g. at the macula. Despite these important advances, the main drawback of graph-cuts based segmentation is that finding the shortest path through a graph is often implemented via Dijkstra's algorithm, which results are retrieved as a graph function, which can only have one coordinate per axial depth scan (A-scan). This makes it impossible to correctly segment structures passing one A-scan more than once, e.g. by ILM overhangs at the ONH. Another disadvantage is that the employed constraints defined in most of the graph-cuts construction can result in underestimating extreme shapes, which regularly occur at the ONH, e.g. deep cups.

An attempt to overcome this problem was presented by [26] by incorporating a convex function in the graph-cut approach, which allowed detection of steep transitions, while keeping the ILM surface smooth. Furthermore, in order to allow the segmentation result to have several coordinates

per A-scan, [27] employed a gradient vector flow field in the construction of the columns used in the graph-theoretic approach.

However, these recent advances still do not consider features of the ONH shape like overhangs. As a consequence, a tedious and time consuming manual ILM segmentation correction is necessary before ONH shape parameters can be derived in scans with deep ONH cupping or steep forms [28].

Recently Keller et al. [29] addressed this issue as well by introducing a new length-adaptive graph search metric. This approach is employed though to delineate the retina/vitreous boundary of a different application and region of the retina, namely for patients with full-thickness macular holes.

Novosel et al. [30] proposed a 3D approach to jointly segment retinal layers and lesions in eyes with topology-disrupting retinal diseases that can handle local intensity variations as well as the presence or absence of pathological structures in the retina. This method extends and generalizes the existing framework of loosely coupled level set, previously developed for the simultaneous segmentation of interfaces between retinal layers in macular and peripapillary scans of healthy and glaucoma subjects [31], drusen segmentation in subjects with dry age-related macular degeneration [32] and fluid segmentation in subjects with central serous rethinopathy [33]. Some of these methods are still 2D based, [32, 33], and all mainly focus on the macula. Carass et al [34] proposed a 3D level set approach based on multiple-object geometric deformable model that overcomes the voxel precision restrictions that are present in the aforementioned methods. This method also focused on macula scans, and included only images without strong pathological changes.

More recently, deep learning emerged as a possible alternative to established graph-cuts, promising a flexible framework for retina analysis. Fang et al. [35] used a convolutional neural network to predict the central pixel label of a given image patch, and subsequently used the graph based approach to finalize the segmentation, while Roy et al. [36] designed a fully convolutional network (FCN) to segment retinal layers and fluid filled cavities in OCT images, partly based on [37] and [38]. These methods are all based on pixel-wise labelling without using topological relationships between layers or layer shape, which can lead to errors in the segmentation. He et al. [39] proposed a framework to correct topological defects by cascading two FCNs. This method was also applied and tested only on macula scans.

In order to address this issue, we here propose a modified Chan-Vese (CV) based segmentation method with sub-pixel accuracy that is fast, robust and able to correctly detect 3D ILM surfaces regardless of ONH shape complexity or overhangs.

Key features of the developed framework are:

- This approach addresses the issue of ILM A-scan overhangs, which are frequently seen in eyes from patients with neurologic or autoimmune neuroinflammatory diseases.

- We include an additional lower boundary constraint in the Chan-Vese method in order to avoid the level set evolution in tissue regions with low contrast.

- The parameters c_1 and c_2 from the level set equation [40] were obtained as a result of an optimization process and further modified after several iteration steps by a scaling factor that incorporates the data locally. This greatly increased the segmentation accuracy.

- We adapted a local fitting intensity energy introduced by [41] into the narrow-band context.

- One of the most important aspects of our work is the thorough investigation and automatic setting of parameters involved in the level set equation through an optimization process. Thus, we optimized and validated our approach using 3D ONH scans from a heterogeneous data set of 40 eyes of healthy controls and patients with autoimmune neuroinflammatory diseases.

- We further validated our segmentation and investigated the influence of image quality on the results using 100 randomly chosen scans from a large database that included 416 ONH volumes of healthy controls and patients with autoimmune neuroinflammatory diseases.

In the following we describe the algorithmic approach as well as its optimization for segmentation performance and computation time in detail.

2. Methods

2.1. Region based active contour methods

Active contours have been introduced by [42] as powerful methods for image segmentation. A contour C (also called a snake) is moved over the image domain Ω, where the dynamics are defined by the gradient flow of some suitable energy functional $F = F[C]$. Here, $F[C]$ depends on the intensity function $I = I(x) \in [0, 1]$ of the given gray scale image. Thus, the final segmentation is obtained by finding the energy minimizing contour C for the given image I. In region-based methods, the two regions defined by the contour C are used to model the energy function F, as proposed in a general setting by [43].

Let Ω denote the image domain. In the context of OCT volumes, Ω is 3D, and we are looking for a surface C, that divides the retinal tissue from the vitreous body, i.e. the final contour should be the segmented ILM, satisfying:

$$\text{inside } (C) = \Omega_1 \simeq \text{the retinal tissue} \tag{1}$$

$$\text{outside}(C) = \Omega_2 \simeq \text{the vitreous body} \tag{2}$$

The classical CV model [40] approximates the intensity function $I(x)$ by some piecewise constant function with values c_1 and c_2 in Ω_1 and Ω_2, respectively, $x = (x, y, z)$ is a voxel in the image I. The energy F^{cv} is defined as the weighted sum of a region based *global intensity fitting (gif) energy* F^{gif}, penalizing deviations of $I(x)$ from the corresponding value c_i, $i \in 1, 2$, a surface energy F^{surf} given by the surface area of C, and a volume energy F^{vol} given by the volume of Ω_1:

$$F^{\text{cv}}[C] = F^{\text{gif}} + \mu F^{\text{surf}} + \nu F^{\text{vol}}, \tag{3}$$

$$F^{\text{gif}} = \lambda_1 \int_{\Omega_1} |I(x) - c_1|^2 \, dx + \lambda_2 \int_{\Omega_2} |I(x) - c_2|^2 \, dx, \tag{4}$$

$$F^{\text{surf}} = \int_C ds, \quad ds \text{ is the area element} \tag{5}$$

$$F^{\text{vol}} = \int_{\Omega_1} 1 \, dx. \tag{6}$$

Note that by minimizing F^{cv}, the surface energy F^{surf} leads to a smooth contour surface C, whereas the volume energy F^{vol} yields a balloon force. Moreover, minimizing F^{cv} with respect to the values of c_1 and c_2 results in choosing c_1 and c_2 as the average intensities in the regions Ω_1 and Ω_2, respectively. The positive weighting parameters λ_1, λ_2, μ, ν control the influence of the corresponding energy term. Finding good values for these parameters is crucial for obtaining the desired results. Usually the parameters λ_1 and λ_2 are taken to be equal and may therefore be set to $\lambda_1 = \lambda_2 = 1$. In section 3.5 it will be explained how values for several parameters of our final model were established.

2.2. Challenges in OCT images

The classical CV model [40] is robust in segmenting noisy images, without clearly defined boundaries. Moreover, complicated shapes such as overhangs, various connected components,

(a)　　　　　　　　　　(b)　　　　　　　　　　(c)
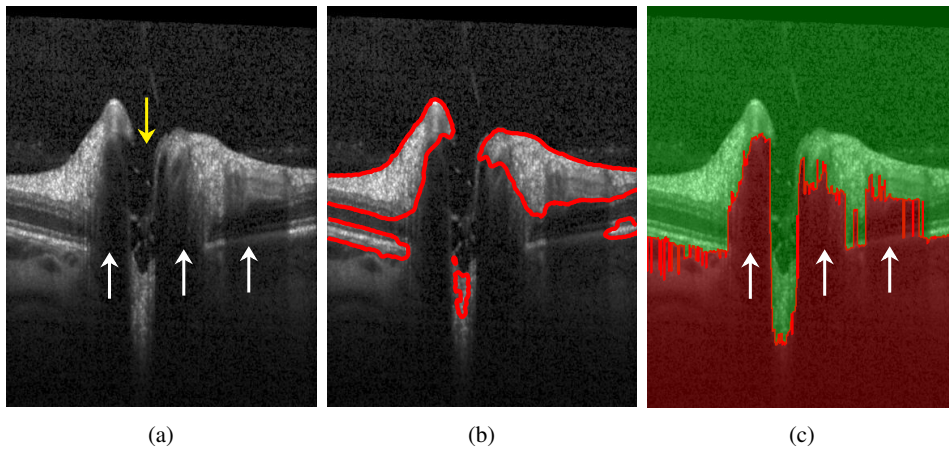
Fig. 2. a) B-scan presenting several challenges for ILM segmentation using the original CV model: the yellow arrow shows the ONH region with no retinal layer information except several tissue remaining from nerve fibers and the ILM; the white arrows show shadows caused by the presence of large blood vessels. b) B-scan showing segmentation results using the original CV model. c) Boundary potential V on a sample B-scan. In the red area, $V(\mathbf{x}) = \rho$, whereas in the green area $V(\mathbf{x}) = 0$.

even topological changes are handled naturally. However, applying the original formulation of CV to OCT scans does not yield good results. As already discussed in the literature, see e.g. [41], CV fails to provide good segmentation if the two delineated regions, in our case, Ω_1 and Ω_2, are strongly non-uniform in their gray values. Performance gets even worse in the presence of very dark regions inside the tissue, see Figs. 2(a) and 2(b), where a slice (B-scan) of a typical OCT volume scan is depicted, or in regions with extreme high intensities inside the tissue or the vitreous. As a consequence, using local image averages, as proposed in the classical CV model, is not able to provide a satisfactory segmentation.

In the following, we address these problems by adapting the global fitting energy to a local one in the narrow band setting [41] and by using a boundary potential to prevent the contour to move into certain regions. These modifications result in a very stable segmentation algorithm for OCT scans provided that the coefficients weighting the energy terms are chosen suitably.

2.2.1. Global fitting energy

We adapt the global values c_1 and c_2, obtained after optimization (see subsection 3.5), column-wise (per A-scan) in order to obtain correct segmentation results at the ONH, where the tissue has very low intensity and little contrast to the vitreous, see Fig. 3(a). We scale the values on each column using the formula:

$$\hat{c}_i = \frac{c_i}{2}\left(1 + \max_{k \in M} I(\mathbf{x}_{kl})\right) \qquad i \in \{1, 2\}\,, l \in N\,, \tag{7}$$

where $M \times N$ is the size of a B-scan. This significantly improves the segmentation results, see Fig. 3(b). Additionally, in order to prevent the contour to penetrate the retina in regions with dark upper but hyperintense lower layers, see see Fig. 3(c), we rescale these values again, after the interface has almost reached the desired ILM contour. The factor used is computed with the same formula as in Eq. (7), but the maximum intensity considers only voxels from the top of the volume to 77 µm (20 px) below the current interface position. Segmentation results obtained after this scaling step are shown in Fig. 3(d).

(a)   (b)   (c)   (d)
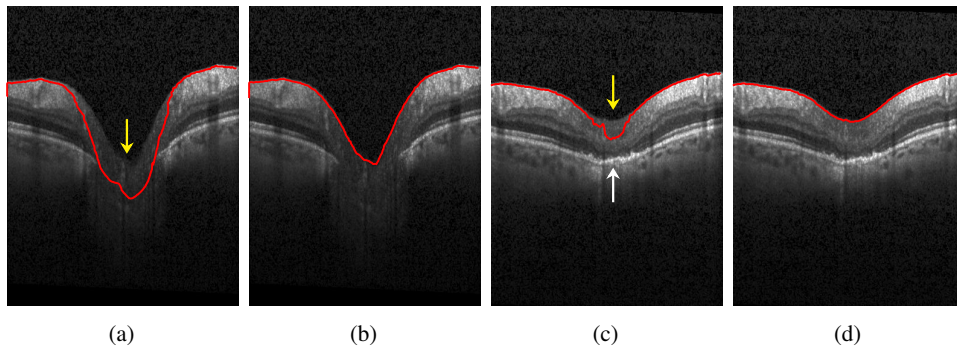
Fig. 3. a) Example of an ONH region with very low contrast compared to the vitreous (yellow arrow). This leads to the contour leaking into the tissue. b) The same scan with correctly detected ILM after scaling the values for c_1 and c_2 according to equation 7; c) Example of an ONH region with low intensity values at the inner layers (yellow arrow) compared to the dark vitreous as well as to the hyperintense outer layers (white arrow). This causes the contour to falsely detect parts of the lower layers as vitreous. d) The same scan with correctly detected ILM by rescaling values c_1 and c_2 after the interface has almost reached the desired ILM contour.

We choose to rescale the values of c_1 and c_2 instead of rescaling the column intensities, since the latter would also influence the local fitting energy (lif), presented in section 2.2.3.

2.2.2. Boundary potential

To prevent the contour C, at the ONH, from evolving into dark areas, caused by absence of retinal layers and presence of large vessels, characteristic to this region (see Fig. 2(a)), we introduce a local boundary potential $V(\mathbf{x})$:

$$F^{\text{bound}} = \int_{\Omega_1} V(\mathbf{x}) \, d\boldsymbol{x} \,. \tag{8}$$

This potential is set to a very high value ρ at these dark regions, detected as follows: in each column, starting from bottom to top, $V(\mathbf{x})$ is set to ρ until the first gray value $I(\boldsymbol{x})$ is larger than 45 % of the maximum gray value in that column. All the other voxels are set to 0, see Fig. 2(c) for an example.

2.2.3. Local intensity fitting energy

In images with large intensity inhomogeneities, e.g. caused by varying illumination, it is not sufficient to minimize only a global intensity fitting energy. In order to achieve better segmentation results, [41] introduced two fitting functions $f_1(\boldsymbol{x})$ and $f_2(\boldsymbol{x})$, which are supposed to locally approximate the intensity $I(\mathbf{x})$ in Ω_1 and Ω_2, respectively. The local intensity fitting energy functional is defined as:

$$
\begin{aligned}
F^{\text{lif}} = \lambda_1 \int \int_{\Omega_1} K_\sigma(\boldsymbol{x} - \boldsymbol{y}) |I(\boldsymbol{y}) - f_1(\boldsymbol{x})|^2 \, d\boldsymbol{y} \, d\boldsymbol{x} \\
+ \lambda_2 \int \int_{\Omega_2} K_\sigma(\boldsymbol{x} - \boldsymbol{y}) |I(\boldsymbol{y}) - f_2(\boldsymbol{x})|^2 \, d\boldsymbol{y} \, d\boldsymbol{x} \,.
\end{aligned}
\tag{9}
$$

Similar to the global constants c_1, c_2, explicit formulas for functions f_1 and f_2 are obtained by energy minimization [41]. Since all calculations are restricted to a narrow band along the contour in our approach, we used compact support kernels for K_σ based on a binomial distribution with

σ representing the kernel size. The adapted formula for calculating f_1 and f_2 is presented in Appendix 7.2. Note, that these modifications also considerably reduce the computation time as compared to a global convolution.

2.3. Our energy model

In a final step, the influence of the local and global intensity fitting energy, are combined similar to the work presented in [41] by introducing another weight parameter ω and to arrive at our modified CV functional F:

$$F = \omega\, F^{\text{gif}} + (1 - \omega)F^{\text{lif}} + \mu\, F^{\text{surf}} + \nu\, F^{\text{vol}} + F^{\text{bound}}. \tag{10}$$

2.4. Level set formulation

To solve the minimization of the above energy functional, the level set method [40] is used, which replaces the unknown surface C by the level set function $\phi(\mathbf{x})$, considering that $\phi(\mathbf{x}) > 0$ if the point $\mathbf{x}$ is inside C, $\phi(\mathbf{x}) < 0$ if $\mathbf{x}$ is outside C, and $\phi(\mathbf{x}) = 0$ if $\mathbf{x}$ is on C. Energy minimization is then obtained by solving the following gradient descent flow equation for ϕ to steady state:

$$\frac{\partial \phi}{\partial t} = \delta_\varepsilon(\phi) \left[-(1 - \omega)F_{local}(\mathbf{x}) - \omega\, F_{global}(\mathbf{x}) + \mu \operatorname{div}\left(\frac{\nabla\phi}{|\nabla\phi|}\right) - \nu - V(\mathbf{x}) \right] \tag{11}$$

$$\text{with} \qquad F_{global}(\mathbf{x}) = -(I(\mathbf{x}) - c_1(\mathbf{x}))^2 + (I(\mathbf{x}) - c_2(\mathbf{x}))^2. \tag{12}$$

$F_{local}(\mathbf{x})$, adapted to our narrow band approach, is given in detail in appendix 7.2. In the above Formula, δ_ε denotes the smoothed Dirac delta function having compact support on the narrow band of width ε, see appendix 7.1, and $k = \operatorname{div}\left(\frac{\nabla\phi}{|\nabla\phi|}\right)$ is the mean curvature of the corresponding levelset surface.

3. Implementation

3.1. Initial contour

For initialization we developed a basic 2D segmentation algorithm to create a start contour (start segmentation). In a first step, morphological filters (erosion and subsequent dilation with 15×7 ellipse structure element) and a smoothing filter (Gaussian blur with kernel size 15×7 and variance $\sigma_x = 6, \sigma_z = 3$) are used, to reduce speckle noise. In the next step, we set each pixel with at least 35 % of the maximum column intensity to white. The remaining pixels are set to black. To keep only the tissue connected to the retina, enhanced at the previous step, we set the pixel values of all connected components consisting of less than 2,400 pixels, which corresponds to 0.11 mm^2 in the used OCT data sets, to gray. Finally, in each column the contour is set at the first white pixel from top to bottom. If no white pixel exists, the first gray pixel is taken instead. These processing steps are exemplified in Fig. 4.

3.2. Narrow band and reinitialization

Starting with the initial contour, the signed distance function and the reinitialization of the 3D level set function is computed using fast marching [44, 45, s. 86]. We use the L^1 norm to achieve faster calculation time. For the same reason the reinitialization process is done only every 10th iteration step, while the computation for f_1 and f_2 each 5th iteration step. All computation is done on the narrow band around the zero level set of width $\varepsilon + \max(\sigma_x, \sigma_y, \sigma_z)$, where σ is the kernel size of K_σ, see Eq. (9), ε represents the regularization value for the smooth Heaviside function H_ε and Dirac delta function δ_ε. Our value for ε is 5.

(a)	(b)	(c)
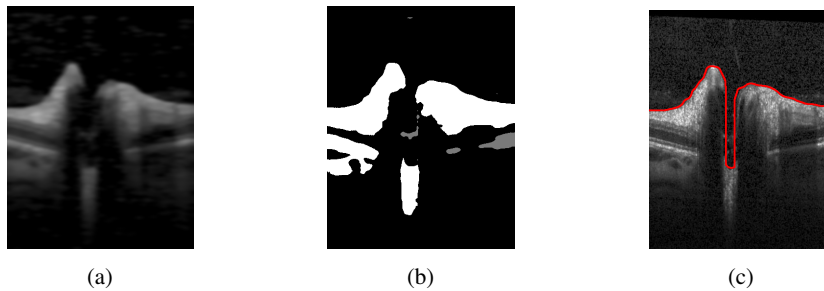
Fig. 4. Three processing steps to obtain initial segmentation: a) filtering with morphological and Gauss filter b) thresholding, neglecting small connected components c) the initial contour

3.3. Removal of non-connected volume parts

A bad initial contour can produce non connected volumes in the tissue and in the vitreous. To improve the segmentation we remove these volumes from the final result, as well as ignore a small area around the image border, where unnatural connectivities might occur due to low contrast or missing image information.

3.4. Numerical implementation and computation time

To solve the gradient flow equation, an explicit first order time discretization is used, where for the spatial finite difference discretization we followed [40]. Note, the volume scan has different resolution in the two lateral directions, see below, section 3.5.1. We accounted for this by choosing different spatial mesh sizes $h_x = h_z = 1$ and $h_y = 3$. The higher value in y direction reduces the influence of differences between the B-scans, especially near the cup, and reduces computation time. Also, curvature weight parameters, $\mu_x = \mu_z = 3.5\,\mu_y$, are direction dependent in order to create a smooth contour. The lower resolution in y direction is forces the segmentation to include even small tissue that is still connected to the retina. For the chosen parameters see Table 4.

The computation time depends on the initial contour and on the shape of the ONH, and takes on average 14.2 s (minimum time is 12.8 s, maximum 15.9 s) on a standard PC (Intel Core i7-5600U (2×2.6 GHz) with Debian 9 and gcc 6.3.0). For the ONH scan shown in Fig. 12(a) 15.5 s were needed (0.2 s for creating the initial contour and 15.3 s for segmentation using the proposed CV method). The OCT image size was $384 \times 496 \times 145$ voxels.

3.5. Parameter optimization

We used an automatic parameter optimization procedure to find values for the parameters v, ω, c_1 and c_2 for our computational model (11).

3.5.1. OCT image data

Image data consisted of 3D ONH scans obtained with a spectral-domain OCT (Heidelberg Spectralis SDOCT, Heidelberg Engineering, Germany) using a custom ONH scan protocol with 145 B-scans, focusing the ONH with a scanning angle of $15° \times 15°$ and a resolution of 384 A-scans per B-scan. The spatial resolution in x direction is $\approx 12.6\,\mu m$, in axial direction $\approx 3.9\,\mu m$ and the distance between two B-scans $\approx 33.5\,\mu m$. Our database consists of 416 ONH volume scans that capture a wide spectrum of ONH topological changes specific to neuroinflammatory disorders (71 healthy control eyes, 31 eyes affected by idiopathic intracranial hypertension, 60 eyes from neuromyelitis optica spectrum disorders, and 252 eyes of multiple sclerosis patients). We have chosen 140 scans randomly from this database, which presented different characteristics, from scans with good quality up to noisy ones, from healthy but also eyes from patients with

different neurological disorders, in order to cover a broad range of shapes. 40 ONH scans were manually segmented and used as ground truth for the optimization process. These will be called the *group40*. The remaining 100 scans – in the following referred to as the *group100* – were used for the validation of the segmentation results and assessment of image quality influence on the segmentation results.

Incomplete volume scans as well as those with retinas damaged by other pathologies were not included.

3.5.2. Error measurement

All 40 scans of the *group40* were manually segmented and checked by an experienced grader. From this dataset, 20 images were used for optimization, while the other 20 for validating the results. For one optimization run, 10 files were randomly chosen from the optimization set. The measure used for the minimization process was defined as the sum of the errors for the parameter v, ω, c_1 and c_2. An error metric similar to the one described in [46] was employed, where the error is defined as the number of wrongly assigned voxels, i.e. the sum of the number of false positive and false negative. Note that this metric does not depend on the position of the retina. In order to compare different optimization results, the accumulated error of all the 20 scans of the optimization set was used.

3.5.3. Optimization algorithm

The method chosen is the multi-space optimization *differential evolution algorithm* as provided by GNU Octave [47].

This algorithm creates a starting population of 40 individuals with random values. In our case, an individual represents a parameter set for v, ω, c_1 and c_2 together with the accumulated segmentation error of the 10 selected volume scans. During optimization, the algorithm crosses and mutates the individuals to create new ones, and drops out newly created or old ones depending on which exhibits larger errors. We allowed for at most 2000 iterations and set box constraints for all four parameters. Note that for each newly created individual, the cost function (error) has to be evaluated by first performing 10 segmentations for the randomly chosen OCT-scans, then calculating the error by comparing with results from manual segmentation. Thus, each iteration step is computationally demanding. The differential evolution algorithm has been chosen since it is derivative free and supports the setting of specific bounds for the parameters. Moreover, we observed a high reproducibility of the finally obtained optimal parameter set. To perform the optimization, we used the Docker Swarm on OpenStack infrastructure from [48], which allowed to do parallel computations on a PC cluster.

4. Results

4.1. Optimization results

In Table 1, the results of all 10 optimization runs sorted in increasing order of the total error are presented. The parameters given in the first line, namely $v = 0.03248, \omega = 0.15915, c_1 = 0.24206, c_2 = 0.94945$ have been chosen for all subsequent calculations.

Note that the four parameters v, ω, c_1, c_2 are not independent from each other as it can be seen in the definition of the energy functional. The parameter that shows the largest variation is the balloon force weight parameter v. This variation is highly influenced by the presence or absence of one specific volume scan in the randomly chosen optimization set (subset of 10 out of 20), which appears as outlier with highest error in all 10 error distributions as shown in Fig. 5. This occurs because the parameters will account for this particular scan if it is contained in the optimization set.
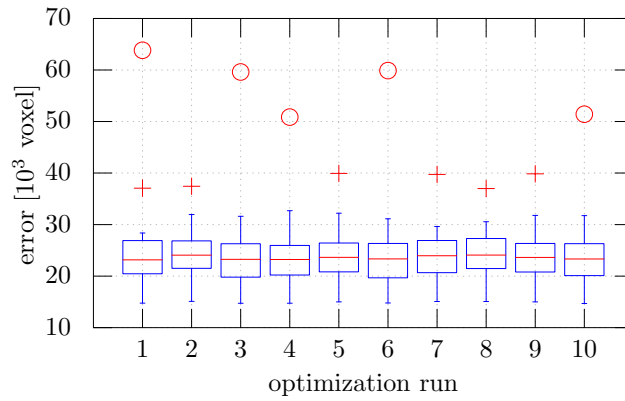
Fig. 5. Error distribution over 20 scans represented as box plots for the 10 optimization runs. The + symbol and the ○ symbol denote outliers with an error deviating more than $1.5 \times STD$ and more than $3.0 \times STD$ from the mean, respectively.
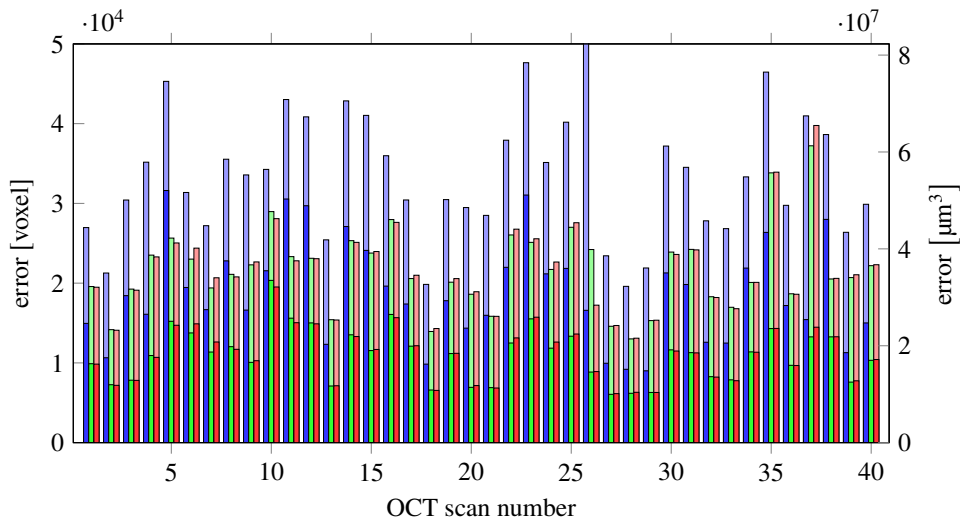
Fig. 6. Errors of the complete data set (40 scans): segmentation of the device (blue), proposed algorithm with the segmentation of the device as initial contour (green) and proposed algorithm with own initial contour (red). The lower bars show the error in the inner 1.5 mm circle of the ONH. The device error of scan 26 is very high (110 508 voxels) because the segmentation was completely wrong on some B-scans.

Table 1. Total error and parameter values as obtained in 10 optimization runs, sorted in ascending order of the error. Total error represents the accumulated error of the 20 scans in the optimization set.

opt run	error voxel	error mm^3	ν	ω	c_1	c_2
9	481 105	0.791 99	0.032 48	0.159 15	0.242 06	0.949 45
5	481 749	0.793 05	0.033 20	0.165 73	0.256 22	0.940 07
7	483 610	0.796 11	0.026 97	0.138 75	0.237 06	0.942 65
8	483 995	0.796 75	0.024 83	0.124 19	0.148 03	0.973 19
2	484 557	0.797 67	0.027 73	0.186 85	0.276 64	0.859 89
4	486 982	0.801 66	0.047 25	0.213 80	0.291 79	0.968 95
10	487 606	0.802 69	0.045 57	0.215 77	0.278 02	0.962 55
3	495 657	0.815 95	0.052 70	0.224 31	0.273 95	0.998 17
6	496 627	0.817 54	0.051 71	0.225 65	0.291 19	0.989 22
1	506 210	0.833 32	0.066 50	0.315 48	0.329 14	0.949 59

4.2. Evaluation of segmentation performance

Our results are summarized in Fig. 6. For each scan, numbered from 1-40, the first bar (blue) represents the segmentation error given by ILM segmentation implemented in the device, the second bar (green) is the error of our segmentation method starting with an initial contour given by the device's segmentation, and the last bar (red) represents the error of our segmentation method starting with an initial contour calculated as described in subsection 3.1. The lower bars represents the amount of error at the ONH region.

For evaluation and analysis of our results, we used GNU Octave version 4.0.3 [49] and R version 3.3.2 [50]. Our segmentation method outperforms the segmentation available from the device (Wilcoxon Signed-Rank Test p-value = 1.837×10^{-10} at 0.05 confidence interval).

To check the influence of the initial contour, we compared the results of our segmentation method, obtained starting either with our own initial contour (mean / STD = 21 707 / 5365, STD represents standard deviation) or with the segmentation given by the device (mean / STD = 21 715 / 5152; Wilcoxon Signed-Rank Test p-value = 0.3007 at 0.05 confidence interval). Our model outperforms again the segmentation of the device (error of the segmentation of the device mean / STD = 34 884 / 14 062; Wilcoxon Signed-Rank Test p-value = 1.819×10^{-12} at 0.05 confidence interval). Moreover, starting with two different initializations, the results of our method are very close to each other (bars 2 and 3), therefore showing that our method is independent on a given rough estimation of the ILM.

We then looked at the error contribution of the central region around the ONH consisting of all A-Scans within a radius of 1.5 mm. Around 50 % of the total error is represented by the errors in the ONH centered region, which usually presents the strongest topological challenges. When evaluating the same comparison with the ILM segmentation computed by the device, our algorithm again performed considerably better (error inside the center region with our algorithm mean / STD = 11 092 / 3306, as compared to the error of the device mean / STD = 18 744 / 6328; Wilcoxon Signed-Rank Test p-value = 1.819×10^{-12} at 0.05 confidence interval).

Lastly, we evaluated the local error size distribution, i.e. the local Euclidean distance between manual and our automatic segmentation on each B-scan of all 40 scans, see Fig. 7 and mean error as well as 10 %, 50 % and 90 % quantile of the error distribution, see Table 2. Here we have calculated the distance of each line segment of the calculated segmentation line to the ground truth segmentation line at each OCT slice. Note that the manual segmentation is pixel based whereas our proposed method has subpixel accuracy. We can see a large majority of these local
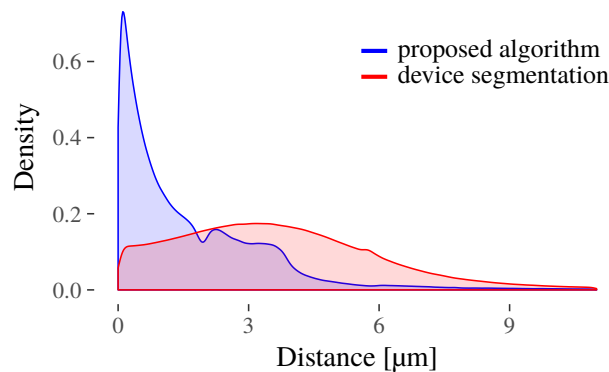
Fig. 7. Normalized distribution of local Euclidean distances between manual and automatic segmentation.

Table 2. Mean error, and 10 %, 50 % and 90 % quantile of the error distribution computed as the euclidian distance between automatic (proposed, device) and manual segmentation.

	Mean Error (μm)	10 % Quantile (μm)	50 % Quantile (μm)	90 % Quantile (μm)
Proposed	1.9982	0.1206	1.0792	3.8167
Device	4.8001	0.8846	3.5335	7.2878

errors are less than 2 μm, followed by a range from 2 μm to 4 μm for most of the remaining ones.

4.3. Segmentation validation

To evaluate the performance of our segmentation method in a clinical setting, we analyzed the 100 OCT scans described in section 3.5.1, denoted as *group100*. An experienced grader manually checked all scans and corrected the segmentation, if necessary. Besides segmentation results, the influence of scan quality on the segmentation was assessed. To this end, another experienced grader labeled regions in all scans (initial *group40* see section 3.5.2, and the aforementioned *group100*) according to the following criteria:

- Incomplete scan (top)
- Incomplete scan (bottom)
- Missing signal
- Low SNR
- Bad illumination
- More than one of the above criteria

Figure 8 shows a B-scan with the labeled A-scans that suffer from low SNR, and the corresponding SLO image with a projected map of all A-scans labeled according to these quality criteria.

Table 3 shows all A-scans of *group100* that have been assessed according to the quality criteria, as well as the number of their corresponding corrected A-scans. It can be seen, that less than 0.2 % of all A-Scans had to be corrected. Note, that scan quality does influence the segmentation results, yet only a smaller percentage of bad quality regions presented also an erroneous ILM: 13.3 % of the A-scans having low SNR and 6.2 % of the ones with low illumination. In the concrete clinical application context a user would be interested on his workload in number of B-scans that must be corrected. The modified A-Scans in Table 3 represent 724 B-scans, a rather
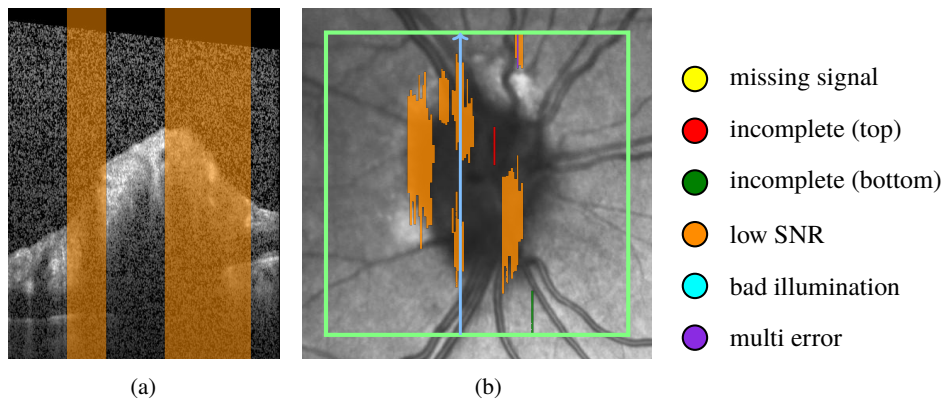
Fig. 8. Quality assessment of a volume scan: (a) B-scan with low SNR region in orange, (b) corresponding SLO image with quality assessment map, color coded according to the criteria shown at the right hand side of the map; green rectangle delimits the scan area; blue arrow shows the B-scan position.

Table 3. Overview of scan quality (with corresponding labels) and segmentation corrections, as well as voxel error of the corrections made for 100 volume scan, randomly selected from a large database.

quality label	multi error	cut lower	cut upper	low SNR	bad illumination	no label
all A-scans	230	49	2782	11 563	6189	5 315 187
modified A-scans	0	0	20	1541	381	8557
modified A-scans in %	0.00	0.00	0.72	13.33	6.16	0.16
mean voxel error of modified A-scans	0.00	0.00	13.75	5.49	1.02	6.37

low fraction (5.0 %) of the total number of 14 500 evaluated.

Furthermore, Fig. 9 shows the error distribution in μm^3 for all B-scans of *group40* and *group100*, respectively. Although the two groups underwent a different segmentation correction process the results presented in these two figures are similar. Most of the scans present small errors, with few larger outliers. 77.15 % of *group40* and 99.3 % of *group100* are below 0.0003 mm^3. To understand the magnitude of these outliers, note that the average volume of a healthy control is (1.80 ± 0.49) [21]. The maximum error per volume for *group40*, 0.065 46 mm^3, represents 3.6 % of an average volume, while 90 % of all volumes have an error less or equal to 0.0454 mm^3, e.g. 2.52 % of the average volume. For *group100* the maximum error per volume is 0.012 59 mm^3, 0.69 % of an average volume, while the error for 90 % of all volumes is less or equal to 0.0025 mm^3, which represents 0.138 %.

We emphasize again a very important aspect of the ONH OCT scans. Due to the anatomy of the ONH and blood vessels, the contrast between tissue and vitreous is often insufficient to precisely delimit the retinal tissue even for an experienced grader. To investigate the segmentation goodness in these ambiguous parts, a second experienced grader labeled these in all scans of *group100*. The results showed that, from all the corrected voxels, approximately 25 % were contained in these labeled areas.

4.4. ILM segmentation

We present several challenging examples selected from the larger database presented in subsection 4.3. Figure 10 shows a case where a hole in 3D is formed. Our segmentation (red line) is able to correctly detect the ILM, whereas the device implemented method fails. Also Fig. 11 shows several cases where our method manages to detect all visible tissue being connected to
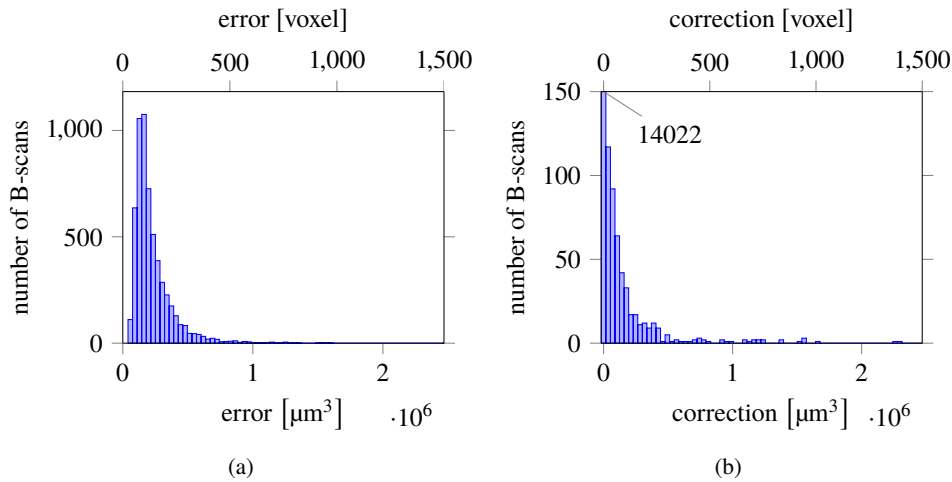
Fig. 9. Distribution of errors per B-Scan (a) (*group40*) obtained by comparing with manual segmentations, (b) (*group100*) as obtained by the corrections performed by an experienced grader.
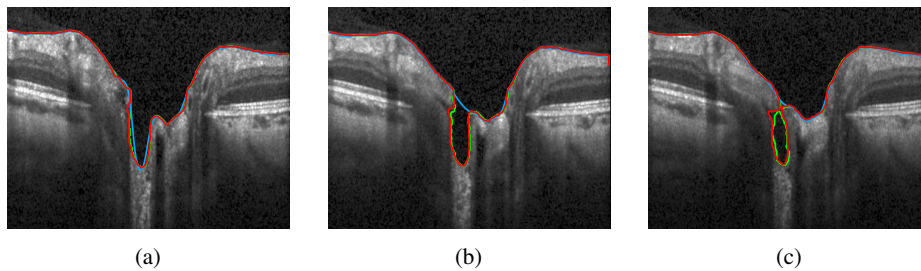
Fig. 10. Segmentation of three neighboring B-scans obtained from the 3D segmentation of the volume scan. The green line depicts the manual segmentation, the red our proposed method, and the blue line the segmentation as given by the device.

the ILM. To emphasize the 3D nature of our method, we present in Fig. 12 rendered surfaces obtained from the segmentation result. It can be clearly seen, that overhangs in the cup create special topologies, that were not properly handled by previous methods.

5. Discussion

We developed and implemented a method for segmenting the ILM surface from ONH centered 3D OCT volume scans utilizing a modified CV model. We optimized, tested and validated the method on scans presenting a variety of ONH shapes found in healthy persons and patients with autoimmune neuroinflammatory disorders.

Our method is providing ILM segmentation that handles not only steep cups, but also challenging topological structures, i.e. overhangs. To achieve this we performed several modifications to the original CV approach, which enabled us to account for low contrast regions especially at the limit between vitreous and retina, for strong inhomogeneities throughout a single B-scan, but also throughout the entire volume by introducing a local fitting energy additionally to the global one. Wang et al. [41] introduced an energy functional with a local fitting term and an auxiliary global intensity fitting one and showed the advantages of using such an approach in terms of
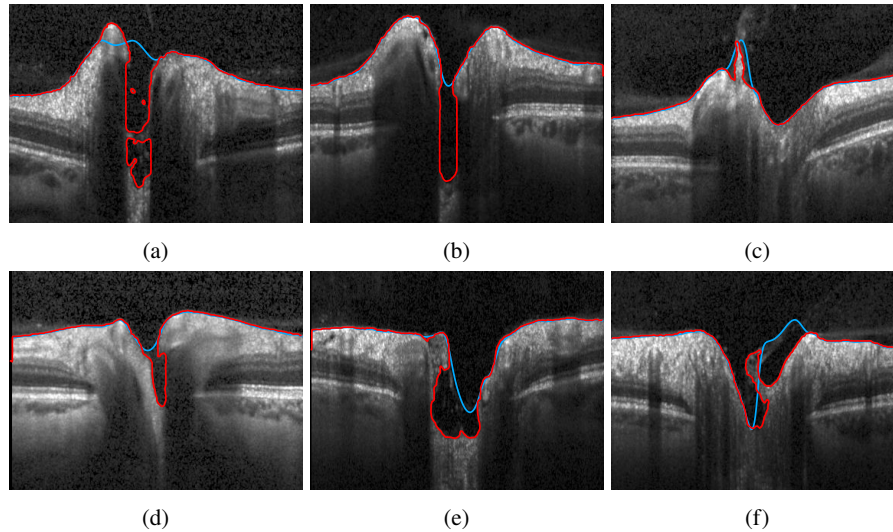
Fig. 11. Segmentation results, showing B-scans that present particular challenges: deep cups - (a), (b), and (e); overhangs - (a), (d), (e), and (f); tissue still connected to ILM: (c). The red line depicts our proposed method, and the blue line the segmentation given by the device.
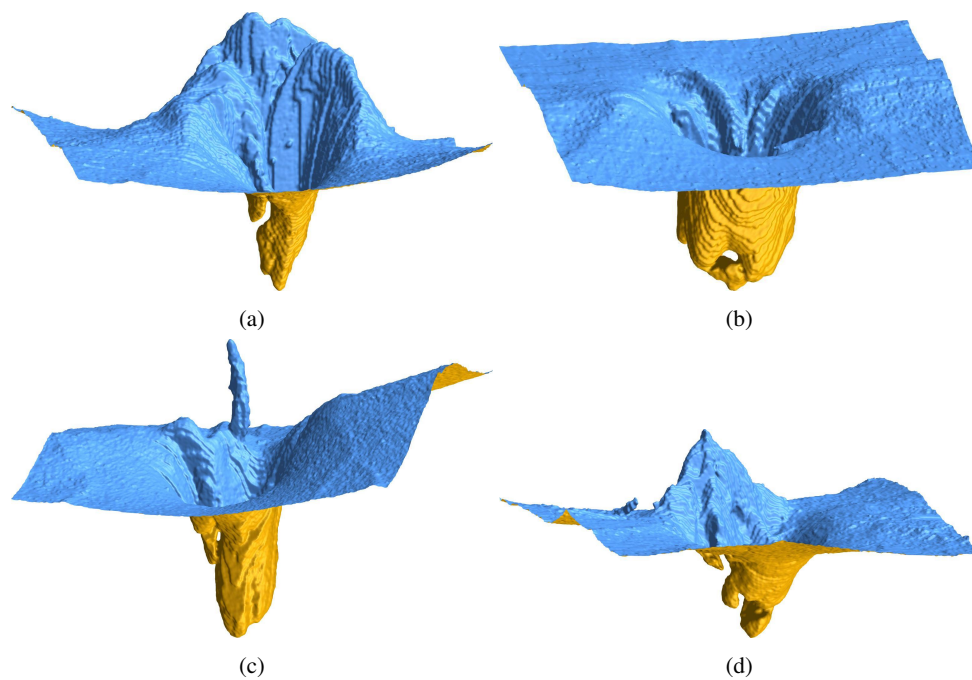
Fig. 12. 3D view of the ILM segmentation results showing particularly interesting topologies at the ONH.

accuracy and robustness in inhomogeneous regions. Our method further expands this approach by incorporating this energy formulation in a computational efficient narrow-band method. By locally rescaling the two parameters c_1 and c_2 in the global energy definition (see subsection 2.1 and 2.2.1) we further stop the interface from entering inside retinal tissue. Furthermore, the introduction of a boundary potential successfully accounts for shadows cast by the presence of large blood vessels at the ONH. Not the least, we carefully chose key parameters ω, ν, c_1 and c_2 as a result of an extensive optimization process.

As a result, the performance of the proposed multi-energy segmentation framework significantly improved segmentation results compared to the one integrated in the commercial device. Furthermore, our approach's results were independent from the initialization contour.

We did not compare our method with other retinal segmentation methods found in the literature, since each method was evaluated on different types of retinal images, different metrics for the accuracy measurement. However, to our knowledge, none of the existing methods, i.e. when based on graph-cuts, tackles the challenge of segmenting overhangs present especially at the ONH region [27, 51–57].

Of note, although the length-adaptive method introduced by Keller et al. [29] and evaluated in pathologic eyes in the macula region performed better than the shortest path algorithm, it was not able to successfully segment every feature of the pathology presented. Here, especially weak gradients caused segmentation challenges. Again, a direct comparison with this method is difficult since this approach was applied to the macula region. Also, it is not clear how this approach would handle overhangs that present as several holes in one B-scans.

Several level-sets methods have also been employed in retinal layer segmentation, most of which are related to the macula region and, or specific pathologies in this region [30–34]. [32, 33] use 2D segmentation, which limits their capabilities in capturing challenging 3D structures, as seen at the ONH. Furthermore, most of these methods focus on the macula, except [31] which also provides data on ONH scans, although as the authors stated themselves, this algorithm would need further modifications to account for difficult topologies. To overcome the intensity variation and disruptive pathological changes caused by several diseases, [30] proposed a 3D approach steered by local differences in the signal between adjacent retina layers. It is not clear how this approach would perform at the ONH, especially in low contrast between vitreous and interface, since this might be the reason why drusen, especially small ones were not so accurately detected. Another question that arises is, to which extend is the segmentation affected by noise, since the later is highly dependent on the contrast between layers in the attenuation coefficient values.

Deep learning based methods are an important advancement, which might lead to powerful segmentation approaches of retinal tissue [35, 36, 39]. Their performance is highly dependent on the training dataset [58], and thus their applicability to a broad clinical spectrum of retinal changes remains to be shown. It will be interesting to see first applications of this potentially very promising approach for segmenting ONH scans.

A limitation of our method lies in the successful detection of an initial contour. This failed in one case among the investigated 40 scans used in the optimization process, which was caused by weak image quality and an grossly uneven image contrast. For practical use, a minimum image quality might prevent such errors.

We also tested the performance of our segmentation on a larger database, containing 100 volume scans of healthy controls and several different neurological disorders and investigated the influence of image quality on the goodness of the segmentation. The results have shown that our proposed segmentation is robust against scan image quality (like noise, and bad illumination) with only a small percentage of the total segmentation having to be corrected in these cases. Additionally, overall the amount of error was small, with few outliers, which represented a small amount of the total volume of a complete scan. Therefore, our segmentation represents a considerable improvement over the current commercial solution. Furthermore, it can be employed

in the clinical routine.

Our method may present a key component in future approaches to analyze overall ONH structure and volume in health and disease. For this, an accurate detection of tissue between ILM and BM is necessary. Further, detection of the ONH center and the ocular axis are required to establish coordinate origin and scan rotation. We previously developed a 2D based segmentation approach for ONH volume computation [59], which was able to robustly detect the BM as lower boundary in healthy people as well as in patients suffering from various neurological disorders [21, 22, 60]. However, in this method the other key surface for volume computation - the ILM - was taken from the device itself, which led to erroneous boundary definitions in many cases. Thus, with the proposed modified CV based method, ILM detection for ONH volume computation may be further optimized.

6. Conclusion

It is crucial to have a robust ILM segmentation for the analysis of ONH structure in both neurologic and ophthalmologic conditions. A better insight in morphometric changes of the ONH could potentially improve diagnosis and the understanding of diseases like multiple sclerosis, neuromyelitis optica spectrum disorders, Parkinson's disease and Alzheimer's dementia.

Our approach provides a flexible and accurate computational method to segment the ILM in 3D OCT volume scans. We could show the superiority in performance of the proposed CV model compared to a standard commercial software method and its robustness against the large variations in the ONH topology. Furthermore, our method is fast and allows for flexible initialization. Thus, it shows great potential for clinical use as it is capable to robustly handle ONH data of both healthy controls and patients suffering from different neurological disorders. We hope that similar concepts, especially the optimization framework, will be applied in other applications as well.

7. Formula

7.1. Regularized Heaviside and delta function

For numerical calculation we use the approximated Heaviside function H_ε

$$H_\varepsilon(z) = \begin{cases} 1 & z > \varepsilon \\ 0 & z < -\varepsilon \\ \frac{1}{2}\left[1 + \frac{z}{\varepsilon} + \frac{1}{\pi}\sin\left(\frac{\pi z}{\varepsilon}\right)\right] & |z| \leq \varepsilon \end{cases} \tag{13}$$

with corresponding smoothed Dirac delta function δ_ε

$$\delta_\varepsilon(z) = \begin{cases} 0 & |z| > \varepsilon \\ \frac{1}{2\varepsilon}\left[1 + \cos\left(\frac{\pi z}{\varepsilon}\right)\right] & |z| \leq \varepsilon \,. \end{cases} \tag{14}$$

We made this choice in order to have compact support of δ_ε, being the narrow band of width 2ε.

7.2. Convolution with compact support kernel

The calculation of the local intensity fitting force involves convolutions which have been adapted for allowing to consequently use the narrow band. Here, not all values are well defined and therefore the convolution formula has to be modified.

The definition of the local intensity averages are modified according to (*nan* means *not a*

number)

$$f_1(x) = \begin{cases} \frac{K_\sigma(x) * [H_\epsilon(\phi(x)) I(x)]}{K_\sigma(x) * H_\epsilon(\phi(x))} & K_\sigma(x) * H_\epsilon(\phi(x)) > 0 \\ nan & \text{other} \end{cases} \tag{15}$$

$$f_2(x) = \begin{cases} \frac{K_\sigma(x) * [(1 - H_\epsilon(\phi(x))) I(x)]}{K_\sigma(x) * [1 - H_\epsilon(\phi(x))]} & K_\sigma(x) * [1 - H_\epsilon(\phi(x))] > 0 \\ nan & \text{other} \end{cases} \tag{16}$$

Now the local fitting forces are calculated as follows:
If $\int_{f_1(y) \neq nan} K_\sigma(y - x) > 0$ and $\int_{f_2(y) \neq nan} K_\sigma(y - x) > 0$, then

$$F_{local}(x) = \left[-\lambda_1 \frac{\int_{f_1(y) \neq nan} K_\sigma(y - x) |I(x) - f_1(y)|^2 \, \mathrm{d}y}{\int_{f_1(y) \neq nan} K_\sigma(y - x)} + \lambda_1 \frac{\int_{f_2(y) \neq nan} K_\sigma(y - x) |I(x) - f_2(y)|^2 \, \mathrm{d}y}{\int_{f_2(y) \neq nan} K_\sigma(y - x)} \right] \tag{17}$$

in other case, set

$$F_{local}(x) = 0 \tag{18}$$

7.3. Parameters

All parameter values of our computational model are shown in Table 4.

Table 4. Parameter values; x, y, z denote coordinate directions horizontal, axial (A-scan), and lateral (between B-scans).

Symbol	Explanation	Value
ν	weight parameter of balloon force	0.03248
ω	local energy weight	0.15915
$1 - \omega$	global energy weight	
c_1	global fitting gray value in Ω_1	0.24206
c_2	global fitting gray value in Ω_2	0.94945
μ	weight parameter of curvature	$\mu_x = 0.035$ $\mu_y = 0.010$ $\mu_z = 0.035$
τ	time step	0.0015
n	number of iterations (time steps)	140
λ_1	tissue area weight	1
λ_2	vitreous body area weight	1
ε	half of narrow band width	5
ρ	boundary potential value	25
σ	local energy convolution kernel size	$\sigma_x = 2$ $\sigma_y = 0$ $\sigma_z = 2$
h	spatial mesh size	$h_x = 1$ $h_y = 3$ $h_z = 1$

Disclosures

A patent application has been submitted for the method described in this paper. KG: (P); FH: (P); FP: (P); AUB: (P), Nocturne UG (I); EMK (P), Nocturne UG (I,E). F. Paul serves on the scientific advisory board for the Novartis OCTIMS study; received speaker honoraria and travel funding from Bayer, Novartis, Biogen Idec, Teva, Sanofi-Aventis/Genzyme, Merck Serono, Alexion, Chugai, MedImmune, and Shire; is an academic editor for PLoS ONE; is an associate editor for Neurology Neuroimmunology and Neuroinflammation; consulted for Sanofi Genzyme, Biogen Idec, MedImmune, Shire, and Alexion; and received research support from Bayer, Novartis, Biogen Idec, Teva, Sanofi-Aventis/Genzyme, Alexion and Merck Serono. A.U. Brandt served on the scientific advisory board for the Biogen Vision study; received travel funding and/or speaker honoraria from Novartis Pharma, Biogen , Bayer and Teva; has consulted for Biogen, Nexus, Teva and Motognosis, Nocturne.

Optic nerve head three-dimensional shape analysis

Sunil Kumar Yadav
Ella Maria Kadas
Seyedamirhosein Motamedi
Konrad Polthier
Frank Haußer
Kay Gawlik
Friedemann Paul
Alexander Brandt

Optic nerve head three-dimensional shape analysis

Sunil Kumar Yadav,[a,b,c,†] Ella Maria Kadas,[a,b,*,†] Seyedamirhosein Motamedi,[a,b] Konrad Polthier,[c] Frank Haußer,[d] Kay Gawlik,[a,b,d] Friedemann Paul,[e] and Alexander Brandt[a,b]
[a]Charité – Universitätsmedizin Berlin, NeuroCure Clinical Research Center, Corporate Member of Freie Universität Berlin, Humboldt – Universität zu Berlin, and Berlin Institute of Health, Berlin, Germany
[b]Charité – Universitätsmedizin, Experimental and Clinical Research Center, Max Delbrück Center for Molecular Medicine, Berlin, Germany
[c]Freie Universität Berlin, Mathematical Geometry Processing Group, Berlin, Germany
[d]Beuth University of Applied Sciences, Berlin, Germany
[e]Charité – Universitätsmedizin Berlin, Department of Neurology, Berlin, Germany

Abstract. We present a method for optic nerve head (ONH) 3-D shape analysis from retinal optical coherence tomography (OCT). The possibility to noninvasively acquire *in vivo* high-resolution 3-D volumes of the ONH using spectral domain OCT drives the need to develop tools that quantify the shape of this structure and extract information for clinical applications. The presented method automatically generates a 3-D ONH model and then allows the computation of several 3-D parameters describing the ONH. The method starts with a high-resolution OCT volume scan as input. From this scan, the model-defining inner limiting membrane (ILM) as inner surface and the retinal pigment epithelium as outer surface are segmented, and the Bruch's membrane opening (BMO) as the model origin is detected. Based on the generated ONH model by triangulated 3-D surface reconstruction, different parameters (areas, volumes, annular surface ring, minimum distances) of different ONH regions can then be computed. Additionally, the bending energy (roughness) in the BMO region on the ILM surface and 3-D BMO-MRW surface area are computed. We show that our method is reliable and robust across a large variety of ONH topologies (specific to this structure) and present a first clinical application. © The Authors. Published by SPIE under a Creative Commons Attribution 3.0 Unported License. Distribution or reproduction of this work in whole or in part requires full attribution of the original publication, including its DOI. [DOI: 10.1117/1.JBO.23.10.106004]

Keywords: optical coherence tomography; shape analysis; optic nerve head; mesh surface; bending energy; volume.

Paper 180331R received Jun. 5, 2018; accepted for publication Aug. 6, 2018; published online Oct. 12, 2018.

1 Introduction

Many neurological and ophthalmological conditions affect the retina. Two landmark structures of this affection are the macula and the optic nerve head (ONH). Parameters describing the shape of these structures, especially 3-D parameters, are gaining more and more importance in understanding normative data and disease-specific changes, in form of additional information along with traditional quantitative ones. For example, in the case of the macula, several studies and approaches have already been published in order to provide a better insight into the definition of healthy structure and shape.[1–5] ONH represents the part in which all retinal ganglion cell axons gather to leave the eye toward the brain. As such, investigating the ONH is central to the diagnosis of many disorders affecting the optic nerve like glaucoma,[6] idiopathic intracranial hypertension (IIH),[7,8] optic neuritis (ON),[9,10] and optic neuropathies of other etiology, for example, in the context of multiple sclerosis (MS) or neuromyelitis optica spectrum disorders (NMOSD).[11–13]

The advent of fast spectral domain optical coherence tomography (OCT) recently allows *in vivo* 3-D imaging of retinal structures, including the ONH. While high-resolution ONH images can now be taken in 3-D, the complex ONH shape has so far made automatic image analysis challenging.

Main focus of this work is to fill in this gap by presenting and validating a robust and fully automatic method that is capable of analyzing ONH shape over a range of conditions. Our approach includes a fully automatic 3-D shape analysis pipeline, with various techniques that will be presented throughout the paper. The algorithm is shown to be stable to various 3-D ONH scans and is—to our knowledge—the first approach that fully exploits the 3-D nature of the ONH for computational image analysis.

1.1 Related Work

Analyzing tissue damage and structural changes in the ONH is one of the key goals to improve the diagnosis and understanding of diseases related to this structure. The main focus of ONH research lies in the field of ophthalmology, the most prominent topic being glaucoma. The most common parameters utilized include length, areas, volumes, or ratios to quantify various regions of the ONH. The main anatomical structures needed to compute these parameters are the inner limiting membrane (ILM), Bruch's membrane or the lower boundary of the retinal pigment epithelium (denoted throughout the paper, for simplicity, by RPE) and the Bruch's membrane opening (BMO) points. The first two structures comprise the retina, and the BMO points have recently gained more and more attention since Reis et al.[14] introduced these as being the true anatomical structure defining the optic disc as to the clinically identified margin using fundus photography. Following this work, several other groups[15,16] proved BMO-based parameters superiority in reliability compared to cup-to-disk ratio.

For ONH analysis, Enders et al.[17] and Muth and Hirnei[18] used manual segmentation of the BMO points and minimal rim width (BMO-MRW), as well as commercially available ILM surface detection with manual correction to study the

---

*Address all correspondence to: Ella Maria Kadas, E-mail: ella-maria.kadas@charite.de

†Sunil Kumar Yadav and Ella Maria Kadas contributed equally.

correlation between visual fields and structural ONH changes. Chauhan et al.[19] proposed BMO-MRW as a marker for early glaucoma detection also using manual segmented BMO points and BMO-MRW measurements, while Pollet-Villard[20] used a similar manual process to prove that structure–function relationship was significantly stronger using BMO-MRW over other ONH parameters derived from spectral-domain OCT. Furthermore, several studies focused on the description of normative values that characterize the shape of the ONH. Chauhan et al.[21] analyzed BMO-MRW, the orientation of the long axis of BMO in a normal population, while Enders et al.[17] described BMO-MRW in micro- and macrodiscs.[22] BMO minimum rim area (BMO-MRA) correlates with the total number of nerve fibers traversing the optic nerve and was introduced and investigated in Refs. 23 and 24. Both studies have shown BMO-MRA's high diagnostic power for glaucoma. All these studies used commercial available OCT software to retrieve the ILM surface and BMO points, which were then manually controlled and corrected by experienced graders.

Another important parameter is the ONH volume, previously analyzed mainly in relation to conditions characterized by ONH swelling. To this end, a 2-D segmentation has been previously developed by our group. The method[25] is able to robustly detect the lower boundary of the RPE in healthy as well as in ONHs from patients suffering from various neurological disorders that lead to swelling of the ONH. Several other publications investigating the same condition[26,27] followed, all using a graph-cut based approach to segment the ILM and BM at the ONH. Lee et al.[28] introduced an end-to-end pipeline to compute several morphometric parameters (volumes in different ONH regions and related area parameters). Furthermore, a surface correspondences approach to create a normalized space was presented. However, this pipeline is semiautomatic and needs manual segmentation of the ILM, BM, and BMO points. For the development of the mean surfaces, an accurate registration between the ONH surfaces is needed. Gibson et al.[29] introduced an ONH registration algorithm to compute the one-to-one correspondence between two ONH surfaces using the hemispherical surface and volume registration. Later, Lee et al.[30] proposed a more sophisticated registration algorithm based on surface currents and hemispherical demons. Recently, the shape variability of retinal nerve fiber layer (RNFL)-choroidal thickness was investigated using a nonrigid surface registration for longitudinal analysis.[31]

In general, most of the published methods related to ONH morphometry are computing the traditional parameters (lengths, widths, and volumes) and performing layers segmentation either manually or semiautomatically. To the best of our knowledge, none of the published ONH morphometry methods use proper manifold 3-D ILM or BM surfaces but rather a 2.5D surface (i.e., a graph function on an XY-grid).

1.2 Contribution

In this paper, we propose a fully automatic 3-D shape analysis of the ONH region and introduce 3-D shape parameters along with

commonly used ones. The objective of our proposed method is to retrieve robust and reliable 3-D quantitative measurements that describe different aspects of the various shapes of the ONH. Specifically:

- We introduce a fully automatic pipeline for 3-D shape analysis of the ONH region.
- We automatically segment ILM and the lower boundary of RPE along with BMO points.
- We compute triangulated 3-D surfaces of the ILM and the lower boundary of RPE.
- We introduce several 3-D shape analysis parameters, along with traditional parameters.
- We prove the robustness of our algorithm for repeated measurements in healthy control (HC) data.
- We provide quantitative parameters for different ONH regions in healthy people with normal vision, as well as in a dataset with clinical relevance for ONH swelling and atrophy.

2 Method

In this section, we explain the procedure to compute several 3-D shape parameters of the ONH including the preprocessing of the ILM and the RPE surfaces and correspondence between them. Figure 1 shows the algorithm pipeline, where an OCT volume scan is the input of the algorithm. Next, we compute the triangulated ILM and RPE surfaces along with the BMO points. These three structures represent the ONH 3-D shape and serve as inputs for further shape analysis of the ONH. In the remainder of the paper, the ILM and the RPE surfaces will be represented as $\mathcal{M}_{\text{ILM}}$ and $\mathcal{M}_{\text{RPE}}$, respectively, and the BMO points are denoted by $\mathcal{P}$. The ILM and the RPE surfaces are triangulated manifold surfaces and can be written in terms of the set of vertices and faces (triangles):

$$\mathcal{M}_{\text{ILM}} = \{\mathbf{V}_{\text{ILM}}, \mathbf{F}_{\text{ILM}}\} \quad \text{and} \quad \mathcal{M}_{\text{RPE}} = \{\mathbf{V}_{\text{RPE}}, \mathbf{F}_{\text{RPE}}\}.$$

These two surfaces can have different numbers of vertices and triangles. Let us consider that n_{ILM} and m_{ILM} represent the numbers of vertices and faces in the ILM surfaces. Similarly, n_{RPE} and m_{RPE} denote the size of $\mathbf{V}_{\text{RPE}}$ and $\mathbf{F}_{\text{RPE}}$, respectively. The BMO points are represented as $\mathcal{P} = \{\mathbf{p}_i \in \mathbb{R}^3 | i = 1 \cdots n_p\}$, where n_p is the number of the BMO points.

2.1 OCT Image Data

Our algorithm has as input 3-D ONH scans obtained with a spectral-domain OCT (Heidelberg Spectralis SDOCT, Heidelberg Engineering, Germany) using a custom protocol with 145 B-scans, focusing the ONH with a scanning angle of 15 deg ×15 deg and a resolution of 384 A-scans per B-scan. The spatial resolution in x direction is ≈12.6 μm, in
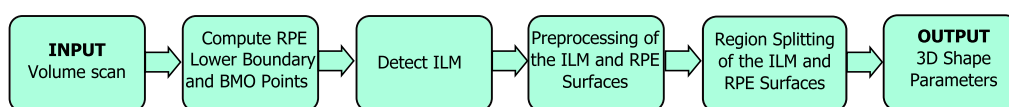

Fig. 1 The pipeline of the proposed algorithm.

axial direction ≈ 3.9 μm, and the distance between two B-scans is ≈ 33.5 μm.

2.2 RPE Lower Boundary Surface Computation

2.2.1 Smoothing and intensity normalization

The RPE lower boundary represents the termination of the retina and is therefore an important parameter in several morphometric computations. In this subsection, we present our RPE segmentation approach based on the method presented in Ref. 25. First, several preprocessing steps are performed, often employed in OCT images. Consider $I(q_{xy})$ the intensity of a pixel q_{xy}. Our algorithm starts by applying a large Gaussian smoothing filter ($\sigma = 5$ pixels isotropic with kernel size = (10 μm $\times$ 14 μm) on each B-scan separately. The smoothing operation not only reduces speckle noise present in most OCT data but also facilitates the approximation of the two most hyperintense layers, the RNFL and the RPE. Then, to address varying intensities, a contrast rescaling on each slice (B-scan) is performed. Contrast inhomogeneities can occur in the form of a B-scan having regions with different illumination or as several B-scans of the same volume with very different intensity ranges. Specifically, a histogram-based amplitude normalization method[32] is used to map the signals in the original image linearly between [0, 1] using as low cutoffs the first, 66th percentiles and as high cutoff the 99th percentile on the histogram of the B-scan, where the sampled column (A-scan) is located. Figure 2(b) shows one B-scans of the resulting smoothed and normalized original volume. Figure 2(a) shows the same B-scan with its original gray values.

2.2.2 RPE approximation

First, we start by approximating ILM as the upper boundary. At each A-scan, we detect the first pixel from top in the smoothed and normalized volume, I_{SN}, higher than 1/3 of the maximum value in the B-scan containing the A-scan. This gives us a set of initial estimate points for the ILM, denoted by ILM_{init}. Next, we approximate the upper boundary of RPE. First, we compute the image derivative, ∇I_{SN}, of each B-scan (vertical gradient) using a Sobel kernel. Looking along each A-scan, starting from the ILM_{init} set, we perform several intermediate steps for the RPE upper boundary approximation. We estimate inner and outer segment junction regions (ISOS) by finding the first set of points p, as shown in Fig. 2(c):

$$p_{xy} = \{\nabla I_{SN}(q_{ixy}) < (\nabla I_{SN}(s_{xy})/3)\}, \quad s_{xy} \in ILM_{init}. \quad (1)$$

Starting from the set p_{xy}, RPE upper boundary is approximated:

$$RPE_{upper} = \max[\nabla I_{SN}(\tilde{p}_{xy})], \quad (2)$$

where we only consider the points below IS/OS:

$$\tilde{p}_{xy} \in \{\|s_{ixy} - p_{ixy}\| < 60 \ \mu m\}. \quad (3)$$

At this stage, our input is a list of points that belong to the upper boundary of RPE in each B-scan. This list comprises among the points correctly positioned at the upper RPE boundary, also several outliers, especially in the presence of shadows cast by blood vessels, as well as at the region of the ONH. In order to remove these, we make use of the observation that the first and last third of each B-scan most probably lie outside the
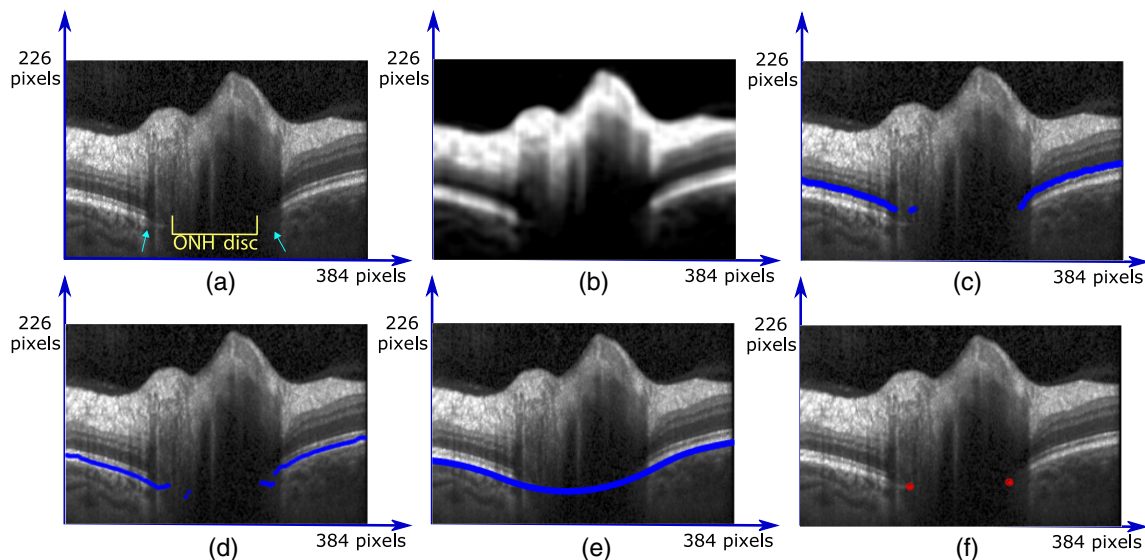
Fig. 2 The first step in our pipeline, specifically the RPE lower boundary surface and BMO points detection exemplified using a B-scans. (a) One B-scan of the original volume (cyan arrows indicate blood vessels and the shadow artifacts these produce; the region delimited by the yellow line is part of the ONH disc). (b) After applying smoothing and intensity normalization. (c) Approximated ISOS junction points (blue points) after removing outliers. As a convention in our computation, the outliers detected at this step are set to have in the axial (z) direction the coordinate equal to 1. (d) Approximated upper boundary RPE points (blue points). (e) Smoothed 2-D RPE lower boundary (blue line). (f) BMO points (red dots); even in the presence of blood vessel the BMO points can still be detected. 384 pixels represent ≈ 4402.80 μm and 226 pixels ≈ 881.40 μm.

optic nerve hear area. This is an observation valid for all the ONH centered scans independently of device or scan settings. Even in these two parts, outliers caused by shadows of blood vessels might be present. To remove these, we take the gradient of the line consisting of the position of upper RPE points and compute the mean value of these from coordinates that most likely belong to the correct upper RPE points. These coordinates represent RPE boundary points that form the largest part of the gradient line between outliers (outliers in the gradient are considered to be >40 μm). The first seed point is then detected as the one closest to the mean value. Starting from this seed q_{seed}, we iteratively remove outliers from RPE_{upper} (points where $\|q_{seed} - q_{new}\| > 70$ μm). Analog outliers from the last third of the B-scan are removed. The resulting point set of one B-scan is shown by the blue points in Fig. 2(d). The points removed from the RPE_{upper} roughly estimate the ONH region, as well as the BMO area (BMOA). Note that ILM can have a very complex topology, whereas other retinal layers are missing in this area. We create a mask of the ONH from the removed RPE_{upper} part by fitting an ellipse to its contour, A_{ONH}.

2.2.3 *RPE lower boundary detection*

The final step consists in the RPE lower boundary detection, RPE_{lower}. We take the points with the largest negative gradient below RPE_{upper}, closest to the RPE_{upper} (i.e., if several minimum points have similar values, the point with the smallest distance to the corresponding RPE_{upper} is taken). Using only the maximum gradient values leads to spurious points along each surface. Correction of these errors is done by applying a cubic smoothing spline with a high smoothing parameter. Note that in the case of presence of blood vessels, large regions of missing coordinates for the RPE might occur and the cubic spline can present deviations from the desired smooth contour.

2.2.4 *TPS fitting to the RPE lower boundary surface*

Finally, to account for motion artifacts in consecutive B-scans, but also for the natural curvature of the retina, we propose an efficient two-stage thin-plate spline fitting (TPS), which improves the approach proposed by Ref. 33 without making use of the orthogonal scans presented in the work of Ref. 34. First, TPS least-square approximation is performed. The number of control points used is determined by the size of the surface along each axial dimension. At this stage, the number is set to 25% in the slow scan direction, 15%, respectively, and the control points are evenly distributed along each direction. This enables the TPS, in combination with a smoothing parameter, α, see Ref. 35 set to 0.85, to create a more smoothed surface, which keeps the curvature of the retina without being influenced from motion artifacts especially along the slow axis. In our experiments, we found that values of $\alpha = [0.70, 0.85]$ provide consistent results. Extreme grid points in the original surface defined as mean + standard deviation in local nonoverlapping neighborhoods of 10×10 grid points of the TPS surface are removed. Then, the actual TPS fitting similar to Ref. 34 is applied. The choice of parameters at this second step is strongly influenced by the fact that we reduced outliers at a previous stage. Specifically, for grid points, we use 20% in the slow scan direction, 10% in the fast scan direction, with smoothing parameter 0.45. Consistent results were obtained for $\alpha = [0.30, 0.50]$. Our strategy is to obtain a TPS closer to the data in the grid points while smoothing the artifacts present in the position of the detected RPE_{lower} points, especially at the presence of blood vessels, or in the close vicinity of the approximated ONH region. Both stages are done on the RPE_{lower} without including A_{ONH}. Figure 3(a) shows the original RPE surface with typical artifacts in the in-between B-scans direction. These are corrected after applying our TPS approach while keeping the shape of the original surface. The result is presented in Fig. 3(b). The result of the RPE lower boundary after performing the TPS is shown in Fig. 2(e).

2.3 *BMO Points Computation*

BMO is the termination of the Bruch's membrane (BM) layer and was proposed as a stable zero reference plane for ONH quantification.[14] It is a key parameter in the detection of ONH shape parameters. A challenge in BMO detection is the correct identification of these points, especially in the presence of shadows caused by blood vessels, or the border tissue of Elsching,[14] a structure similar to the BM. We propose a BMO points'
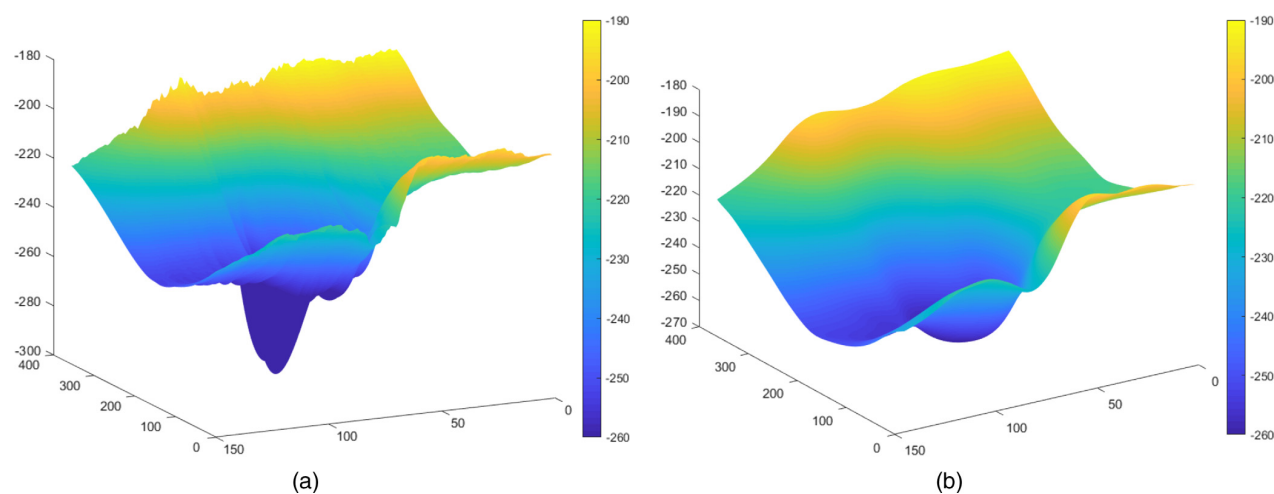
Fig. 3 (a) RPE lower boundary surface with motion artifacts. (b) Resulting TPS fitted surface. The proposed two-stage TPS is capable of reducing the motion and segmentation artifacts seen in the original RPE lower boundary and creating a smoothed surface while still keeping the shape of the retina.

segmentation approach in the 3-D volume directly without the use of a 2-D projection image in the xy plane, as presented in several previous works.[36,37]

2.3.1 Volume flattening

We start by flattening the whole OCT volume. This step, performed in several retinal segmentation algorithms,[33,36] refers to the translation of all A-scans such that a chosen boundary in the volume is flat. We choose to align the retina to the smoothed RPE_{lower}. The alignment facilitates the volume reduction process, as well as the differentiation of BMO from other tissue.

2.3.2 Volume reduction and vessel suppression

We reduce the OCT volume to a region comprising only the BMO. Depending on the ONH region fitted by the ellipse and the position of RPE_{lower}, the reduced volume can change from $384 \times 496 \times 145$ voxels in its original size to $384 \times 90 \times 52$ voxels, by taking only the B-scans containing the ellipse and in z direction $RPE_{lower} \pm 100 \ \mu m$. Vessels appear in the RPE layer as dark intensity regions or shadows. These affect the detection of the BMO, especially because vessels gather at the ONH creating large shadows. Our approach focuses on emphasizing the RPE layer and suppressing these artifacts. To this end, we first smooth the reduced OCT volume containing the original gray values with an anisotropic diffusion filter[38] and then apply a 2-D Morlet wavelet filter[39] for each B-scan to enhance the RPE line.

2.3.3 BMO points detection

The end-points of the rough ONH area, A_{ONH}, provide the starting points for BMO points detection. On each B-scan, the starting points are updated with new BMO points candidates if they meet the following conditions: (1) have minimum value in the 2-D Morlet filtered image, (2) $d(p_{new}, p_{BMO\text{-}seed}) < 30 \ \mu m$, and (3) the curvature in a neighboring region of five voxels is almost 0 to avoid including the tissue of Elsching. In case the BMO points detected in the left and right part of one B-scan overlap, the BMO starting or end region previously defined by A_{ONH} are updated accordingly. An example of a pair of (left and right) detected BMO points are shown in Fig. 2(f).

2.4 ILM Surface Computation

The ILM separates the retina from the vitreous body and defines a critical boundary layer for the ONH. Several ILM segmentation methods have been published to separate the ILM layer around the ONH region, and most of them compute the ILM layer as a graph function and are unable to capture complex and variable topological structures of the ONH. To compute the ILM surface, we previously developed a method introduced by Gawlik et al.[40] This method is based on an active contour method of Chan–Vese type and produces a truly 3-D ILM segmentation unlike other state-of-the-art methods. Figure 4(a) shows the ILM surface, which is computed using the marching cubes algorithm,[41] where the input level sets are computed using the method proposed by Gawlik et al.[40] The lower right corner of Fig. 4(a) shows that the approach is capable to reconstruct a complex topological structure in the ONH region and the marching cubes algorithm produces a manifold ILM surface $\mathcal{M}_{ILM}$ with proper neighborhood and properly oriented face normals.

2.5 ILM Surface Smoothing

During data acquisition of the ONH region using the 3-D OCT scanner, noise is inevitable due to various internal and external factors. As it can be seen from Fig. 4(a), the ILM surface is not smooth and has various noise components. Staircase artifacts are also shown in the left corner of Fig. 4 as an effect of the marching cubes algorithm and of the volume scan resolution. For an accurate shape parameter computation, these artifacts including noise components should be removed at the early stage of the algorithm. To compute a noise free and a high-fidelity ILM surface, we use a robust mesh denoising algorithm, proposed by Yadav et al.[42] In general, mesh denoising algorithms are divided into two categories: isotropic and anisotropic methods. Isotropic methods remove noise effectively but produce a volume shrinkage, which leads to an incorrect shape analysis of the ONH. Anisotropic methods are feature preserving mesh denoising algorithms and induce a small volume shrinkage compared to the isotropic methods. In the case of the ILM surface, the anisotropic methods treat the marching cube artifacts as features and lead to an incorrect shape analysis. The method in Ref. 42 is a combination of both isotropic and anisotropic methods and produces a high fidelity smooth ILM surface without staircase artifacts and minimum volume shrinkage, as shown in Fig. 4(b). This method also produces a high quality triangular mesh with proper face normal orientation, which is vital in further shape analysis of the ONH.

2.6 Ellipse Fitting to BMO Points

As presented in Sec. 2.3, the proposed algorithm computes the BMO points automatically. Due to blood vessels around the ONH, noise components and 3-D OCT scan patterns, the BMO points are nonuniform and noisy, as shown in Fig. 5(a). To remove these artifacts, we fit an ellipse to the BMO point onto XY-plane. First of all, the BMO points $\mathcal{P}$ are projected onto the corresponding XY-plane and denoted as a points set: $\mathcal{P}_{2D} = \{\tilde{\mathbf{p}}_i \in \mathbb{R}^2 | i = 0, \cdots, n_p - 1\}$. Then, we apply the
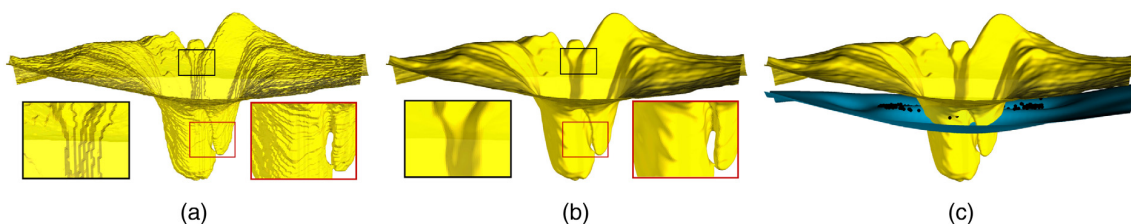
Fig. 4 (a) Noisy ILM surface. (b) Smooth ILM surface. (c) Smooth ILM and RPE surfaces with BMO. The ILM surface computed using the marching cube algorithm and level sets produced by the method.[40]
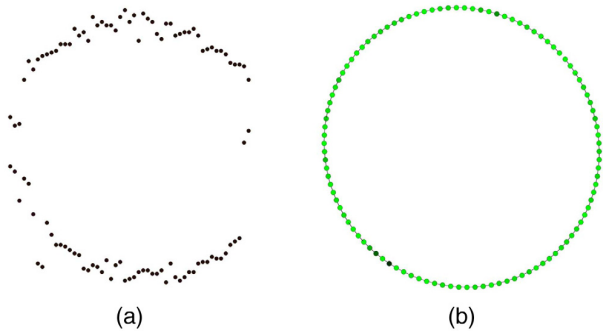
Fig. 5 (a) Noisy and irregular BMO points, which are computed automatically. (b) Smooth and uniform density BMO points are computed using an ellipse fit.

method[43] to compute a fitted ellipse to the BMO points in $\mathbb{R}^2$. Another key parameter in the ONH shape analysis is the center of the BMO points. This is computed as the barycentric of the all $\mathcal{P}_{2D}$ points:

$$\tilde{\mathbf{p}}_c = \frac{1}{n_p} \sum_{\tilde{\mathbf{p}}_i \in \mathcal{P}_{2D}} \tilde{\mathbf{p}}_i, \tag{4}$$

where $\tilde{\mathbf{p}}_c \in \mathbb{R}^2$. Figure 5 shows that the ellipse fitting is not only removes the noise but also increases the data points uniformly.

2.7 Correspondence between ILM and RPE Surfaces

The total retina at the ONH region is delimited by ILM and RPE. For further analysis, it is necessary to find the corresponding points between these two surfaces. In the proposed method, we compute vertices in the RPE surface corresponding to each face ($f_i \in \mathbf{F}_{ILM}|i = 0, \cdots, m_{ILM} - 1$) of the ILM surface. In general, the RPE surface, represented here as a function graph: $\mathcal{M}_{RPE}: \mathbb{R}^2 \to \mathbb{R}$, has a less complex structure compared to ILM. In the OCT scanner, the number of the A-scans (x-direction) and the number of the B-scans (y-direction) are fixed, which create a regular XY-grid as a domain for the RPE graph function. Therefore, the index of each vertex of the RPE surface can be computed using the number of x-lines (vertical lines) and y-lines (horizontal lines) and the sampling size in both directions, denoted by ε_x and ε_y, respectively. The numbers of x-lines and y-lines are computed using the following equation:

$$x\text{line} = \frac{x_{max} - x_{min}}{\varepsilon_x} + 1,$$
$$y\text{line} = \frac{y_{max} - y_{min}}{\varepsilon_y} + 1, \tag{5}$$

where x_{max}, x_{min}, y_{max}, and y_{min} are the bounding values of the RPE surface in x and y directions. For each face $f_i \in \mathbf{F}_{ILM}$, the vertex of the RPE surface onto the XY-plane is computed, which approximates the position of the corresponding A-scan and B-scan in the volume scan. Let us consider that $\mathbf{c}_i$ represents the centroid of the face f_i. To compute the corresponding vertex in the RPE surface, we project the face f_i onto the corresponding XY-plane, $\tilde{\mathbf{c}}_i$ represents the projected centroid. The terms $\tilde{c}_{x_i}$ and $\tilde{c}_{y_i}$ are the corresponding x and y coordinates. We compute the x-index (i_x), the y-index (i_y), and the vertex (i) index using x line and y line in the RPE surface for the face f_i using the following

equation:

$$i_x = \left\lceil \frac{\tilde{c}_{x_i} - x_{min} + \varepsilon_x/2}{\varepsilon_x} \right\rceil, \quad i_y = \left\lceil \frac{\tilde{c}_{y_i} - y_{min} + \varepsilon_y/2}{\varepsilon_y} \right\rceil,$$
$$i = i_x + i_y \cdot x\text{line}, \tag{6}$$

where $\lceil \ \rceil$ represents the ceil function and i denotes the corresponding vertex in the RPE surface. For an accurate computation, we check the neighborhood of vertex i of the RPE surface and the corresponding vertex is computed as follows:

$$\tilde{\mathbf{v}}_i = \tilde{\mathbf{v}}_j \in \Omega_i | \min |\tilde{\mathbf{c}}_i - \tilde{\mathbf{v}}_j|, \tag{7}$$

where Ω_i represents the 3×3 neighborhood (at XY-plane) of vertex i. The term $\tilde{\mathbf{v}}_i$ is the projection of vertex $\mathbf{v}_i \in \mathbf{V}_{RPE}$ onto XY-plane. Finally, we get the set $\mathcal{C} = \{\mathbf{v}_i \in \mathbb{R}^3 | i = 0, \cdots, m_{ILM} - 1\}$, which represents the set of RPE surface vertices corresponding to each face in $\mathbf{F}_{ILM}$. A visual representation of the correspondence computation is shown in Fig. 6, where the RPE's regular XY-grid is shown in blue and the projected ILM's vertices and edges are painted in red.

2.8 BMO Region Segmentation

For the ONH shape analysis, the region inside the BMO points is of special interest since BMO points represent the optic disc margin. To segment this region, we exploit the elliptic representation of the BMO points in $\mathbb{R}^2$ along with their center, as mentioned in Eq. (4). First, we compute the center of the ILM and the RPE surfaces corresponding to the center $\tilde{\mathbf{p}}_c$ of the BMO points. Let us consider that $\tilde{\mathbf{V}}_{ILM}$ and $\tilde{\mathbf{V}}_{RPE}$ represent projected sets of vertices onto XY-plane. Then, the indices of the centers of both surfaces can be computed as follows:

$$\text{ilmc} = j \in 0, \cdots, n_{ILM} - 1 | \min |\tilde{\mathbf{v}}_j^{ILM} - \tilde{\mathbf{p}}_c|,$$
$$\text{rpec} = j \in 0, \cdots, n_{RPE} - 1 | \min |\tilde{\mathbf{v}}_j^{RPE} - \tilde{\mathbf{p}}_c|, \tag{8}$$

where $\tilde{\mathbf{v}}_j^{ILM} \in \tilde{\mathbf{V}}_{ILM}$ and $\tilde{\mathbf{v}}_j^{rpe} \in \tilde{\mathbf{V}}_{rpe}$. The vertices $\mathbf{v}_{ILMc} \in \mathbf{V}_{ILM}$ and $\mathbf{v}_{RPEc} \in \mathbf{V}_{RPE}$ represent the center of the ILM and the RPE surfaces, respectively.

To compute the BMO regions in the ILM and the RPE surfaces, we transform the ellipse into a circle using the affine transform. Let us consider $\tilde{\mathbf{p}}_i^e$ represents the fitted ellipse point to $\tilde{\mathbf{p}}_i$ as mentioned in Sec. 2.6 and $\tilde{\mathbf{p}}_i^c$ denotes the corresponding affine transformed point on a circle of radius r. This transformation reduces the complexity of the BMO region computation and
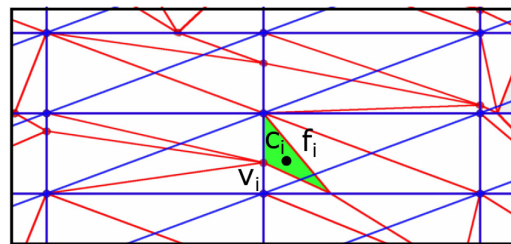
Fig. 6 Correspondence between ILM and RPE surfaces; the face $f_i \in \mathbf{F}_{ILM}$ (green triangle) has a corresponding vertex $\mathbf{v}_i \in \mathbf{V}_{RPE}$ in the RPE surface.

improves the speed of the algorithm. Now, by using the circular representation of the BMO points, the BMO regions in both RPE and ILM surfaces are computed as follows:

$$\Omega_{\mathrm{ILM}} = \{f_j \in \mathbf{F}_{\mathrm{ILM}} || \tilde{\mathbf{c}}_j^{\mathrm{ILM}} - \tilde{\mathbf{v}}_{ilmc}| \leq r\},$$
$$\Omega_{\mathrm{RPE}} = \{f_j \in \mathbf{F}_{\mathrm{RPE}} || \tilde{\mathbf{c}}_j^{\mathrm{RPE}} - \tilde{\mathbf{v}}_{rpec}| \leq r\}, \tag{9}$$

where r is the radius of the transformed circle and $\tilde{\mathbf{c}}_j^{\mathrm{ILM}}$, $\tilde{\mathbf{c}}_j^{\mathrm{RPE}}$ represent the centroid of a face in the ILM and the RPE surfaces, respectively. The computation shown in Eq. (9) is done using the disk growing method.

2.9 3-D Shape Parameters

2.9.1 ONH cup volume

The ONH cup is defined as a segment of the ILM surface, which is below the RPE surface, as shown in Figs. 7(a) and 7(b). Note that the cup is not present in every ONH volume scan. For example, mostly in the case swollen ONH scans, the ILM surface is always above the RPE. To detect the availability of the ONH cup, we go to each face $f_i \in \mathbf{F}_{\mathrm{ILM}}$ and compute its centroid $\mathbf{c}_i$. As we discussed in Sec. 2.7, each face f_i of the ILM has the corresponding vertex $\mathbf{v}_i \in \mathcal{C}$ in RPE. If $c_i^z - v_i^z \geq 0$ for all faces in ILM, then, there is no cup available in the ONH region. Otherwise, there is a cup. The terms c_i^z and v_i^z show the corresponding z-coordinates (height). Similarly, we can compute the cup region:

$$\Omega_{\mathrm{cup}} = \{f_i \in \mathbf{F}_{\mathrm{ILM}} | (c_i^z - v_i^z) \leq 0\}, \tag{10}$$

where Ω_{cup} consists of faces (triangles) of ILM, which are below the RPE surface. As it can be seen from Fig. 7(b), the cup region is also a manifold surface with proper face normal orientation. To compute the volume of the cup accurately, we exploit the face normal information at each triangle of the region. The cup volume is computed using the following equation:

$$V_{\mathrm{cup}} = \sum_{(f_i \in \Omega_{\mathrm{cup}})} \mathbf{A}_i h_i, \tag{11}$$

where $\mathbf{A}_i$ represents the area of a triangle, which is a projection of the face f_i of the ILM surface onto XY-plane and h_i is the height with respect to the RPE surface. These variables are defined as follows:

$$\mathbf{A}_i = \frac{1}{2} (\vec{\mathbf{e}}_0 \times \vec{\mathbf{e}}_1), \quad h_i = (c_i^z - v_i^z), \tag{12}$$

where $\vec{\mathbf{e}}_0$ and $\vec{\mathbf{e}}_1$ are the connected edges of the projected triangle. The cross-product between the two edges will take care of the orientation of the corresponding face and enables a precise volume computation even in complex topological regions.

2.9.2 Central ONH thickness

The CONHT is defined as the height difference between the center of the ILM and the RPE surfaces, as shown in Fig. 7(c). The CONHT of ONH volume scan is computed as follows:

$$\mathrm{CONHT} = (v_{ilmc}^z - v_{rpec}^z), \tag{13}$$

where v_{ilmc}^z and v_{rpec}^z show the corresponding height value (z-coordinates) of the center vertices $\mathbf{v}_{ilmc}$ and $\mathbf{v}_{rpec}$, respectively, introduced in Sec. 2.8.

2.9.3 BMO region volume

The BMO region volume is computed using the segmented ILM and RPE surfaces. We separated the cup volume from the BMO region volume such that it does not include the cup volume, if it exists. Then, the BMO region volume can be computed as follows:

$$\Omega_{\mathrm{BMO}} = \Omega_{\mathrm{ILM}} \setminus \Omega_{\mathrm{cup}}. \tag{14}$$

Similar to the ONH cup volume, we compute the BMO region volume using the similar formula:

$$V_{\mathrm{BMO}} = \sum_{(f_i \in \Omega_{\mathrm{BMO}})} \mathbf{A}_i h_i, \tag{15}$$

where $\mathbf{A}_i$ is the area of the face f_i that belongs to the set Ω_{BMO} and is computed using Eq. (12). Similarly, h_i is also computed using the corresponding vertices in the RPE surface as mentioned in Eq. (12).

2.9.4 ONH total volume

Similar to the ONH cup and the BMO region volumes, the ONH total volume is also computed using ILM and RPE
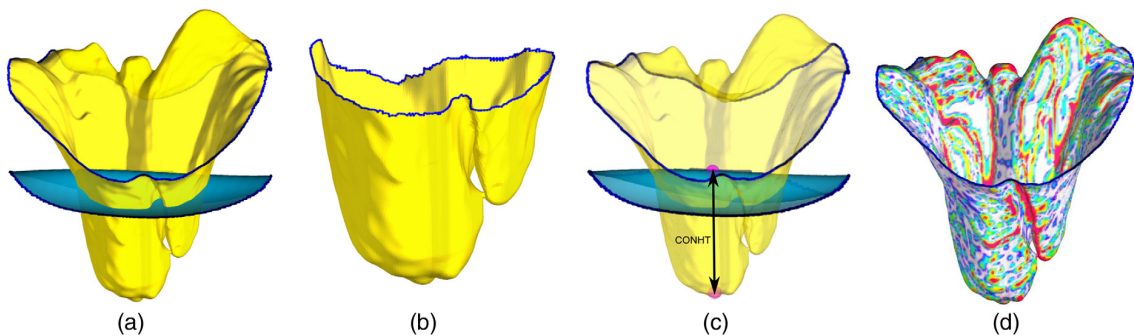
Fig. 7 A visual representation of the different morphological parameters. (a) BMO region, (b) cup volume V_{cup}, (c) central ONH thickness (CONHT), and (d) bending energy E_b.

surfaces. The total volume is computed from the circular region, with radius 1.5 mm, centered at $\mathbf{v}_{ilmc}$ and $\mathbf{v}_{rpec}$ for ILM and RPE surfaces, respectively, as shown in Fig. 8(a). Similar to Eq. (9), we compute the circular regions for ILM and RPE surfaces using the following equation:

$$\Omega_{1.5\text{ mm}}^{\text{ILM}} = \{f_j \in \mathbf{F}_{\text{ILM}} | |\tilde{\mathbf{c}}_j^{\text{ILM}} - \tilde{\mathbf{v}}_{ilmc}| \leq 1.5\text{ mm}\},$$
$$\Omega_{1.5\text{ mm}}^{\text{RPE}} = \{f_j \in \mathbf{F}_{\text{RPE}} | |\tilde{\mathbf{c}}_j^{\text{RPE}} - \tilde{\mathbf{v}}_{rpec}| \leq 1.5\text{ mm}\}, \quad (16)$$

where $\Omega_{1.5\text{ mm}}^{\text{ILM}}$ and $\Omega_{1.5\text{ mm}}^{\text{RPE}}$ are the sets consisting of all faces within the 1.5-mm region of the ILM and RPE surfaces from their centers. The other parameters were defined in Eq. (9). Then, the total volume region is calculated using Eq. (16):

$$\Omega_{tv} = \Omega_{1.5\text{ mm}} \setminus \Omega_{\text{cup}}, \quad (17)$$

where Ω_{tv} represents the total volume region on the ILM surface, as shown in Fig. 8(b), which is further employed for the total volume computation:

$$V_{tv} = \sum_{(f_i \in \Omega_{tv})} \mathbf{A}_i h_i, \quad (18)$$

where $\mathbf{A}_i$ is the area of the face $f_i \in \Omega_{tv}$ and h_i is the height with respect to corresponding vertex in the RPE surface similar to Eq. (12).

2.9.5 ONH annular region volume

The ONH annular region represents the ONH outer region, see Fig. 8(c). On ILM surface, this region is computed using the following equation:

$$\Omega_{av} = \Omega_{1.5\text{ mm}} \setminus \Omega_{\text{BMO}}, \quad (19)$$

where Ω_{av} consists of all the ILM surface faces, which belong to the annular region of the ONH. Similar to Eq. (18), we compute the volume of the annular region using the ILM and RPE surfaces correspondence:

$$V_{av} = \sum_{(f_i \in \Omega_{av})} \mathbf{A}_i h_i. \quad (20)$$

The annular region volume helps to see the change in the outer region of the ONH volume in different cohorts.

2.9.6 Bending energy

The roughness on the ILM surface within the BMO region is an important parameter and commonly known as the bending energy on a manifold surface. The bending energy measures the fairness of a surface in terms of the curvature. In general, the outer region of the ILM surface is quite smooth and flat unlike the one inside the BMO, which has very complex topological structure. In this paper, we define the bending energy within the BMO region using the element-based normal voting tensor (ENVT).[44] The ENVT exploits the orientation information (face normals) to compute a shape analysis operator at each face $f_i \in \Omega_{\text{BMO}}$ and is defined as follows:

$$\mathbf{M}_i = \frac{1}{\sum_{f_j \in \Omega_{\text{BMO}}} a_j} \sum_{f_j \in \Omega_{\text{BMO}}} a_j \mathbf{n}_j \cdot \mathbf{n}_j^T, \quad (21)$$

where $\mathbf{n}_j$ represents the normal of face f_i and $\mathbf{n}_j^T$ is the transpose of $\mathbf{n}_j$. The term a_j is the area of the face f_i. To assure robustness against irregular sampling of the ILM surface, we weight Eq. (21) by the corresponding face area a_j. The ENVT, $\mathbf{M}_i$, is a symmetric and positive semidefinite matrix, so, it can be decomposed into its spectral components:

$$\mathbf{M}_i = \sum_{k=0}^{2} \lambda_k^i \mathbf{e}_k \mathbf{e}_k^T, \quad (22)$$

where $\lambda_k^i = \{\lambda_0^i, \lambda_1^i, \lambda_2^i\}$ are the eigenvalues vector, and these eigenvalues are sorted in decreasing order ($\lambda_0^i \geq \lambda_1^i \geq \lambda_2^i \geq 0$). The corresponding eigenvector is denoted by $\mathbf{e}_k$. In general, the dominant eigenvalue λ_0^i has the corresponding eigenvector in the direction of the face normal and the remaining two eigenvectors will be aligned to the principle curvature direction on the ILM surface. On the planer region, only λ_0^i will be significant, on the edge region, λ_0^i and λ_1^i will be significant and at the corners, all of these eigenvalues are significant. Using the anisotropic properties of these eigenvalues, we define the bending energy inside the BMO region using the following equation:

$$E_b = \sum_{f_i \in \Omega_{\text{BMO}}} \lambda_1^i + \lambda_2^i, \quad (23)$$

where λ_1^i and λ_2^i are the two least dominant eigenvalues of the ENVT of the face f_i. Figure 7(d) shows how each face of the BMO region is colored based on Eq. (26). The color is scaled from white (flat regions) to red (sharp features).
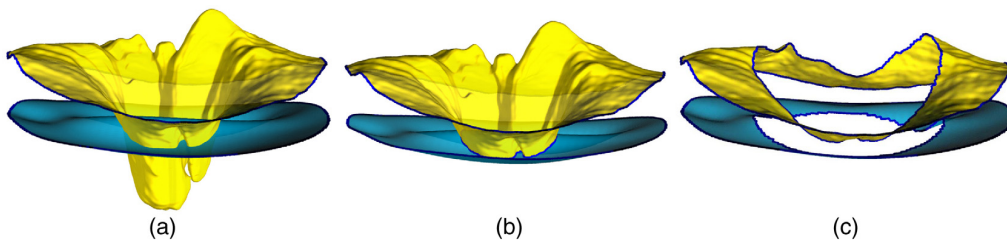
Fig. 8 A visual representation of total and annular volume regions. (a) 1.5 mm regions of ILM ($\Omega_{1.5\text{ mm}}$) and RPE ($\Omega_{1.5\text{ mm}}^{\text{RPE}}$) surfaces from the BMO center. (b) Total volume (V_{tv}) between ILM and RPE surfaces within 1.5 mm radius region. (c) Annular volume (V_{av}) is defined as the volume between ILM after taking out the BMO region.

2.9.7 BMO-MRW

BMO-MRW has been proposed by Ref. 14 as a valid alternative structural measure. It computes the minimum distance between the BMO points and the ILM surface. The average BMO-MRW, denoted by avg_{MRW}, is calculated as follows:

$$\text{avg}_{\text{mrw}} = \frac{1}{n_p} \sum_{i=1}^{n_p} |\mathbf{p}_i^{mrw} - \mathbf{p}_i^e|. \tag{24}$$

2.9.8 BMO-MRW surface area

BMO-MRW surface area, BMO-MRA, is computed by taking the whole region defined by all BMO-MRW. We combine the ellipse fitted BMO points $\mathcal{P}_{2D}$ and the z-coordinates from $\mathcal{P}$ and represent these as $\mathcal{P}_e = \{\mathbf{p}_i^e \in \mathbb{R}^3 \,|\, i = 0, \cdots, n_p - 1\}$, as it can be seen in Fig. 9 (green points). For each point $\mathbf{p}_i^e \in \mathcal{P}_e$, we compute a point $\mathbf{p}_i^{\text{MRW}}$ on the ILM surface:

$$\mathbf{p}_i^{mrw} = \mathbf{v}_j \in \mathbf{V}_{i \times lm} \,|\, \min |\mathbf{v}_j - \mathbf{p}_i^e|. \tag{25}$$

The MRW points $\mathcal{P}_{\text{MRW}} = \{\mathbf{p}_i^{\text{MRW}} \in \mathbb{R}^3 \,|\, i = 0, \cdots, n_p - 1\}$ are lying on the ILM surface as shown in Fig. 9(a) (violet points). We create a quad surface using point sets $\mathcal{P}_e$ and $\mathcal{P}_{\text{mrw}}$ by introducing edges between the corresponding vertices in both point sets and connecting the neighbor points as shown in Fig. 9(b). The number of quad elements in the MRD surface is equal to the number of points in each point sets and is represented as $\mathcal{Q} = \{q_i \,|\, i = 0 \cdots n_p - 1\}$. MRW-MRA is computed as follows:

$$A_{\text{mrw}} = \sum_{q_i \in \mathcal{Q}} a_{q_i}, \tag{26}$$

where a_{q_i} represents the area of the quad q_i.

2.9.9 BMO area

As shown in Fig. 5, BMOA represents the area under the fitted ellipse to the BMO points and is computed using the conic representation:

$$A_{\text{BMO}} = \pi r_1 r_2, \tag{27}$$

where r_1 and r_2 are the major and minor axes of the fitted ellipse.

3 Experiments and Results

In order to evaluate our method, we performed repeated-measurement reliability tests, investigated ONH shape in healthy subjects, and tested if our method is able to detect differences in patients with diseases known to affect the ONH in the form of swelling and atrophy. Finally, we measured the implementation's performance.

3.1 Repeated-Measurement Reliability

In order to estimate the repeated-measurement reliability, we took three repeated scans of each eye from 10 healthy subjects. These subjects were measured each in a time frame of a week and then again in the following week. Table 1 shows the repeatability results. We see that our method scores highly at every parameter presented, with lowest intraclass correlation coefficient (ICC) of 0.905 for CONHT, and highest 0.998 for V_{cup}. The ICC and confidence intervals were estimated using the variance components from a one-way ANOVA.

We also evaluated our method with several other scan protocols of the same device (ONH cube with 73 B-scans, scanning angle of 15 deg × 15 deg and resolution 384 A-scans per B-scan, spatial resolution in x direction is ≈12.6 μm, in axial direction ≈3.9 μm and the distance between two B-scans ≈61 μm, ONH star scan with 24 B-scans, scanning angle of 15 deg × 15 deg and a resolution of 768 A-scans per B-scan, spatial resolution in x direction is ≈5.36 μm, in axial direction ≈3.9 μm) and the volumetric ONH-centered protocol acquired using Cirrus HD OCT (Carl Zeiss Meditec, Dublin, California), which covers $6 \times 6 \times 2$ mm³ region with $200 \times 200 \times 1024$ voxels and obtained positive results.

3.2 Validation

We validated the BMO detection and checked the RPE segmentation. Five scans from the ones used in the repeatability testing were randomly selected. An experienced grader manually selected the BMO points using the RoI tool from ImageJ.[45] This resulted in a total amount of 488 B-scans with manually selected BMO points, which corresponded to the number detected automatically. Furthermore, we compared the mean signed and unsigned error in the x axis, as well as in the axial one (in z axis). If the automated method identified the BMO closer to the optic disc center, the sign of distance in the x-direction was positive. Similarly, if the automated BMO located below the manual BMO, the sign of distance in the z-direction was positive. Results are shown in Table 2. To our knowledge, there is no other study regarding BMO segmentation with the device used in this approach. As such, we are not able to relate our results to other published methods, since comparative studies revealed that measurements are not directly
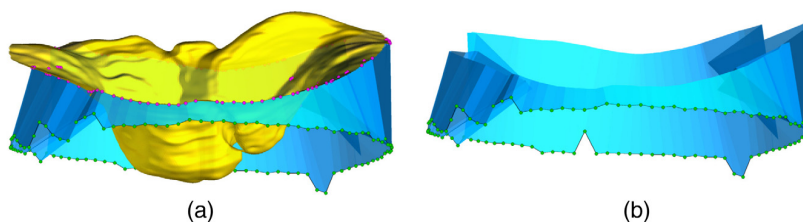

Fig. 9 BMO-MRW surface with and without ILM. (a) BMO-MRW surface with ILM surface and (b) BMO-MRW surface.

Table 1 Repeatability test for the 3-D parameters.

Parameters	ICC	LCI	UCI
ONH cup vol. (V_{cup}) (mm³)	0.998	0.996	0.999
Central ONH thickness (CONHT) (mm)	0.905	0.813	0.958
BMO region vol (V_{BMO}) (mm³)	0.993	0.986	0.997
ONH total vol. (V_{tv}) (mm³)	0.995	0.989	0.998
ONH annular vol. (V_{av}) (mm³)	0.983	0.965	0.993
Bending energy (E_b)	0.911	0.824	0.961
BMO-MRW surface area (A_{MRW}) (mm²)	0.910	0.823	0.960
BMO-MRW (d_{MRW}) (mm)	0.993	0.986	0.997
BMOA (A_{BMO}) (mm²)	0.989	0.976	0.995

Note: LCI, lower boundary of 95% confidence interval and UCI, upper boundary of 95% confidence interval.

comparable between different OCT devices.[46] The ILM validation was done in another work of our research group.[40] For RPE computation, an experience grader visually controlled all scans used in the repeatability testing and assessed these as correctly segmented.

3.3 Clinical Evaluation

In this section, we present the results of our automatic pipeline approach for 248 OCT scans, from three groups, 71 HC eyes, 31 eyes of patients suffering from IIH,[25] which causes swelling of the ONH (papilledema). We also included 146 eyes of patients with autoimmune central nervous system disorders (MS and NMOSD) and a history of ON, an inflammatory optic neuropathy that damages the optic nerve leading to neuroaxonal degeneration.[47,48]

All participants gave written informed consent according to the 1964 Declaration of Helsinki. The study was approved by the ethics committee of Charité – Universitätsmedizin Berlin.

In IIH patients, the ONH volume is increased and was shown to correlate with cerebrospinal fluid pressure.[8] The longitudinal analyses from Ref. 8 revealed that ONH volume measured by OCT decreased after the initial lumbar puncture and initiation of therapy with acetazolamide. Additionally, increased ONH volume was associated with lower visual acuity in IIH patients,

Table 2 Mean unsigned and signed error in pixel and μm, for the x axis, and z axis between automatic (proposed) and manual segmentation.

	Mean ($\pm$SD) unsigned error (pixels)	Mean ($\pm$SD) unsigned error (μm)	Mean ($\pm$SD) signed error (pixels)	Mean ($\pm$SD) signed error (μm)
x axis	4.9098 ($\pm$4.9182)	61.8635 ($\pm$61.9693)	−0.6107 ($\pm$6.9261)	−7.6943 ($\pm$87.2693)
z axis	2.8828 ($\pm$3.1801)	12.4024 ($\pm$11.2429)	−0.3618 ($\pm$4.2790)	−1.4110 ($\pm$16.6881)

which points out to the potential clinical relevance of the parameter.

ON is one of the most common initial clinical presentations of MS without any prior history of a demyelinating event. During the course of the disease, acute ON affects 50% and 70% of MS patients.[9] After initial swelling due to edema in the acute phase of ON, RNFL thickness decreased over the following six months.[47,49] ON is the first NMOSD-related clinical event in 55% of the patients, which causes severe structural damage to the optic nerve and retina with resulting functional impairment. Recurrent ONs in NMOSD give rise to severely thinned pRNFL and combined ganglion cell layer and inner plexiform layer.[11] Furthermore, within 5 years, ~50% of NMO patients are either blind in one or both eyes.[49] RNFL reduction was consistently observed in MS patients, who had never had a clinical episode of ON, as well as in the clinically unaffected fellow eye of patients with a history of ON.[50,51] Similarly, a recent study[52] found that there is also retinal neuroaxonal damage without ON in NMOSD, but longitudinal studies investigating neuroaxonal damage without ON in NMOSD have not been performed extensively.

We hypothesized that patients with IIH would show significant changes in comparison to HCs indicating ONH swelling. Also, patients with a history of ON would show significant changes in comparison to HCs indication ONH atrophy. The results presented in Table 3 demonstrate that our approach successfully captures the differences. The only parameter showing no difference between groups is bending energy, E_b. Although we expected that in the IIH affected eyes, the ONH shape inside the BMO to have a smoother convex shape, the data are still extremely heterogeneous. Thus, the bending energy reflects this extreme variability in the data. Especially inside the BMO, the topologies from one ONH to the other can be extremely different.

We plan to further investigate these findings (for both processes of swelling and atrophy of the ONH) with the parameters presented, to gain more insight into the pathology of the ONH.

3.4 Performance

Computation of the whole pipeline for a volume on an Intel (R) Core(TM) i7-4790, 3.60 GHz, 16 GB RAM and 64bit operating system takes on average 2 min (computation of the ILM, RPE lower boundary and BMO points takes about 75 s, and the morphological computation another 40 and 45 s).

4 Discussion and Conclusion

We have proposed an automatic and robust pipeline for the computation of several parameters that characterize ONH shape. In particular, we developed an approach that computes truly 3-D parameters derived from triangulated mesh surfaces of the ILM and RPE, and BMO points.

The proposed method identifies the RPE lower boundary and is able to provide a smooth 2.5-D surface by employing a two-stage TPS fitting that preserves the retina natural curvature. Then, the estimated location of ONH region is detected and BMO points are identified. The issue of the presence of border tissue and the blood vessels was also dealt with by employing several filters that suppress vessel artifacts and enhance the Bruch's membrane termination points. Additionally, the computation time is significantly reduced by performing the BMO points' detection only in the ONH approximated region.

Table 3 Analysis of all the 3-D parameters defined for the HC and patient group. The last column shows the GEE analysis between the two groups.

Parameters	HC		IIH		ON		GEE		
	Mean (SD)	Min-Max	Mean (SD)	Min-Max	Mean (SD)	Min-Max	p(HC-IIH)	p(HC-ON)	p(IIH-ON)
ONH cup vol. (V_{cup}) (mm³)	0.044 (0.075)	0.000–0.370	0.004(0.012)	0.000–0.049	0.035(0.052)	0.000–0.256	**0.0012**	0.353	**1.95E-07**
Central ONH thickness (CONHT) (mm)	0.002 (0.25)	-0.545–0.550	0.403(0.340)	-0.242–0.966	0.012(0.231)	-0.399–0.668	**9.91E-06**	0.747	**4.22E-06**
BMO region vol (V_{BMO}) (mm³)	0.572 (0.21)	0.107–1.035	1.521 (1.022)	0.436–4.3098	0.444(0.189)	0.105–1.050	**5.02E-05**	**0.0012**	**2.66E-06**
ONH total vol. (V_{tv}) (mm³)	2.523 (0.250)	2.114–2.988	3.309 (0.799)	2.351–5.365	2.163(0.295)	1.522–3.087	**2.57E-05**	**5.28E-13**	**6.54E-10**
ONH annular vol. (V_{av}) (mm³)	1.906(0.181)	1.504–2.268	1.78(0.357)	0.572–2.200	1.683(0.210)	1.162–2.118	0.146	**2.19E-10**	0.257
Bending energy (E_b)	0.026 (0.009)	0.011–0.065	0.029 (0.013)	0.008–0.066	0.029(0.010)	0.011–0.066	0.477	0.038	0.793
BMO-MRW surface area (A_{MRW}) (mm²)	1.791 (0.459)	0.763–2.789	2.975(1.016)	1.439–5.351	1.414(0.364)	0.615–2.765	**1.35E-06**	**5.44E-06**	**3.94E-11**
BMO-MRW (d_{MRW})	0.135(0.054)	0.261–0.035	0.263 (0.105)	0.127–0.447	0.093(0.040)	0.030–0.260	**3.52E-07**	**2.69E-05**	**1.81E-12**
BMOA (A_{BMO}) (mm²)	1.906 (0.352)	1.158–2.646	2.682 (1.109)	1.057–5.709	1.861(0.377)	1.030–3.326	0.0028	0.407	**0.001**

Note: SD, standard deviation; Min, minimum value; Max, maximum value; GEE, generalized estimating equation models analysis accounting for the intereye/intrasubject dependencies; p, p value.

Furthermore, the ILM detection, using a Chan–Vese level set approach, provides a 3-D surface that is able to identify this membrane despite high heterogeneity and complicated topologies of the ONH. The issue of presence of noise and artifacts in the ILM surface, effects of acquisition process and marching cube algorithm, is corrected by employing a robust mesh denoising method. The resulting high fidelity surface preserves the features with minimal shrinkage. It is important to remember that we are interested in detecting even minimal shape changes; obtaining a surface that has no staircase artifacts, but preserves features, is crucial for parameter computation.

The same argument applies to the BMO points. We need a robust detection of this structure. Using our custom scan protocol, we have 145 B-scans in one volume, but only a part of these contain BMO points. Thus, depending on the position of each B-scan and on vessel shadow artifacts, large variation of BMO points in the XY plane can occur. To penalize the deviation of single BMO point coordinates from the elliptic shape of the BMO described in the literature, we fit an ellipse to the initially detected points. Hence, the natural trend of the BMO trajectories in the volume is kept while increasing the number of sample points.

Having these three components, ILM, RPE, and BMO points, our method computes the correspondence between surfaces ILM and RPE, such that each face of the ILM surface has a corresponding vertex in RPE. After this step, we have all the ingredients to derive the parameters.

Although the computed parameters, except the bending energy, were already introduced in several previous studies (mostly for the investigation of glaucoma or papilledema), we are the first to provide quantifiable measurements derived in a truly 3-D context. Furthermore, we were able to provide a first proof of applicability in a clinical setting, by showing the power of several parameters introduced in differentiating between inflammation in form of swelling and destruction in the form of reduction of layer thickness.

To the best of our knowledge, this is the first approach that is able to provide truly 3-D parameters. Most of the morphometric parameters derived for the characterization of the ONH shape[17,21,22,24] use either manual detection or manual correction of commercial software, a time-consuming task prone to subjectivity especially in volume scans consisting of a high number of B-scans. Similarly, methods[30,31,53] performed a manual detection of the BMO points and automatic segmentation of the ILM, BM, and choroid layers to compute surface correspondence between multiple eyes.

Future work will include creation of population normative parameters and statistics using larger cohorts. The goal is to better detect and understand shape changes or differences correlated with neuroinflamatory diseases. Also, shapes from a large group of eyes will be made comparable by a common surface (a mean template); surface correspondence and anatomical changes at different time points will also be detected. Since we are interested in small, localized changes that could be clinically important, for example, as indicators of disease or treatment success, we will investigate the derivation of additional morphometric parameters.

There are several limitations. First, the OCT data were not acquired relative to the foveal-BMO axis, because some of our early data were taken before this concept had been established. OCT devices with wide field optics capable of imaging ONH and fovea in the same scan session may be used to address

this issue in the future and establish the foveal-BMO axis as reference axis to eliminate rotational artifacts, which might increase repeated measurement reliability also in the context of longitudinal measurements. Furthermore, the algorithm was implemented and tested only on images of one device. Future work needs to adapt the approach to imaging data from other devices. Last, the sample size of our HC cohort is too small to allow meaningful investigation of ONH shape parameters correlations, e.g., with age and sex. These analyses should be repeated in a future study with higher sample sizes. We plan to perform an evaluation of our method on a larger dataset with different scan protocols and different OCT devices and to create a normative database for the developed parameters.

In summary, our results showed that the proposed method successfully and robustly identifies ILM, RPE, and BMO points and it enables computing the morphometric parameters, that capture shape characteristics of the ONH.

Disclosures

Acknowledgments

References

1. B. Nesmith et al., "Mathematical analysis of the normal anatomy of the aging fovea," *Invest. Ophthalmol. Visual Sci.* **55**, 5962–5966 (2014).
2. L. Liu et al., "A sloped piecemeal Gaussian model for characterising foveal pit shape," *Ophthalmic Physiol. Opt.* **36**, 615–631 (2016).
3. P. Scheibe et al., "Parametric model for the 3D reconstruction of individual fovea shape from OCT data," *Exp. Eye Res.* **119**, 19–26 (2014).
4. P. Scheibe et al., "Analysis of foveal characteristics and their asymmetries in the normal population," *Exp. Eye Res.* **148**, 1–11 (2016).
5. S. K. Yadav et al., "CuBe: parametric modeling of 3D foveal shape using cubic Bezier," *Biomed. Opt. Express* **8**, 4181–4199 (2017).
6. J. B. Jonas et al., "Glaucoma," *Lancet* **390**, 2183–2193 (2017).
7. F. Kaufhold et al., "Optic nerve head quantification in idiopathic intracranial hypertension by spectral domain OCT," *PLoS One* **7**, e36965 (2012).
8. P. Albrecht et al., "Optical coherence tomography for the diagnosis and monitoring of idiopathic intracranial hypertension," *J. Neurol.* **264**, 1370–1380 (2017).
9. A. T. Toosy, D. F. Mason, and D. H. Miller, "Optic neuritis," *Lancet Neurol.* **13**, 83–99 (2014).
10. S. L. Galetta et al., "Acute optic neuritis," *Neurology* **2**, e135 (2015).
11. F. C. Oertel et al., "Microstructural visual system changes in AQP4-antibody-seropositive NMOSD," *Neurology* **4**, e334 (2017).
12. A. Petzold et al., "Retinal layer segmentation in multiple sclerosis: a systematic review and meta-analysis," *Lancet Neurol.* **16**, 797–812 (2017).
13. J. Bennett et al., "Neuromyelitis optica and multiple sclerosis: seeing differences through optical coherence tomography," *Mult. Scler. J.* **21**, 678–688 (2015).
14. A. S. C. Reis et al., "Influence of clinically invisible, but optical coherence tomography detected, optic disc margin anatomy on neuroretinal rim evaluation," *Invest. Ophthalmol. Visual Sci.* **53**(4), 1852–1860 (2012).
15. B. C. Chauhan and C. F. Burgoyne, "From clinical examination of the optic disc to clinical assessment of the optic nerve head: a paradigm change," *Am. J. Ophthalmol.* **156**(2), 218–227.e2 (2013).
16. M. Young et al., "Comparison of the clinical disc margin seen in stereo disc photographs with neural canal opening seen in optical coherence tomography images," *J. Glaucoma* **23**, 360–367 (2014).
17. P. Enders et al., "The use of Bruch's membrane opening-based optical coherence tomography of the optic nerve head for glaucoma detection in microdiscs," *Br. J. Ophthalmol.* **101**(4), 530–535 (2017).
18. D. R. Muth and C. W. Hirnei, "Structure-function relationship between Bruch's membrane opening-based optic nerve head parameters and visual field defects in glaucoma," *Invest. Ophthalmol. Visual Sci.* **56**(5), 3320–3328 (2015).
19. B. C. Chauhan et al., "Enhanced detection of open-angle glaucoma with an anatomically accurate optical coherence tomography-derived neuroretinal rim parameter," *Ophthalmology* **120**(3), 535–543 (2013).
20. F. Pollet-Villard et al., "Structure-function relationships with spectral-domain optical coherence tomography retinal nerve fiber layer and optic nerve head measurements," *Invest. Ophthalmol. Visual Sci.* **55**(5), 2953–2962 (2014).
21. B. C. Chauhan et al., "Bruch's membrane opening minimum rim width and retinal nerve fiber layer thickness in a normal white population," *Ophthalmology* **122**(9), 1786–1794 (2015).
22. P. Enders et al., "Neuroretinal rim in non-glaucomatous large optic nerve heads: a comparison of confocal scanning laser tomography and spectral domain optical coherence tomography," *Br. J. Ophthalmol.* **101**(2), 138–142 (2017).
23. S. K. Gardiner et al., "A method to estimate the amount of neuroretinal rim tissue in glaucoma: comparison with current methods for measuring rim area," *Am. J. Ophthalmol.* **157**, 540–549.e2 (2014).
24. P. Enders et al., "Novel Bruch's membrane opening minimum rim area equalizes disc size dependency and offers high diagnostic power for glaucoma," *Invest. Ophthalmol. Visual Sci.* **57**, 6596–6603 (2016).
25. E. M. Kadas et al., *3D Optic Nerve Head Segmentation in Idiopathic Intracranial Hypertension*, pp. 262–267, Springer, Berlin, Heidelberg (2012).
26. J.-K. Wang et al., "Automated quantification of volumetric optic disc swelling in papilledema using spectral-domain optical coherence tomography," *Invest. Ophthalmol. Visual Sci.* **53**(7), 4069–4075 (2012).
27. P. Auinger et al., "Baseline OCT measurements in the idiopathic intracranial hypertension treatment trial, part I: quality control, comparisons, and variability," *Invest. Ophthalmol. Visual Sci.* **55**(12), 8180–8188 (2014).
28. S. Lee et al., "End-to-end pipeline for spectral domain optical coherence tomography and morphometric analysis of human optic nerve head," *J. Med. Biol. Eng.* **31**, 111–119 (2011).
29. E. Gibson et al., "Optic nerve head registration via hemispherical surface and volume registration," *IEEE Trans. Biomed. Eng.* **57**, 2592–2595 (2010).
30. S. Lee et al., "Exact surface registration of retinal surfaces from 3-D optical coherence tomography images," *IEEE Trans. Biomed. Eng.* **62**, 609–617 (2015).
31. S. Lee et al., "Quantifying variability in longitudinal peripapillary RNFL and choroidal layer thickness using surface based registration of OCT images," *Transl. Vision Sci. Technol.* **6**(1), 11 (2017).

32. C.-L. Chen et al., "Individual A-scan signal normalization between two spectral domain optical coherence tomography devices," *Invest. Ophthalmol. Visual Sci.* **54**(5), 3463–3471 (2013).

33. M. K. Garvin et al., "Intraretinal layer segmentation of macular optical coherence tomography images using optimal 3D graph search," *IEEE Trans. Med. Imaging* **27**, 1495–1505 (2008).

34. B. J. Antony, "A combined machine-learning and graph-based framework for the 3-D automated segmentation of retinal structures in SD-OCT images," PhD Thesis, AAI3608177, Iowa City, Iowa (2013).

35. K. Rohr et al., *Point-Based Elastic Registration of Medical Image Data Using Approximating Thin-Plate Splines*, pp. 297–306, Springer, Berlin, Heidelberg (1996).

36. B. J. Antony et al., "Automated 3D segmentation of multiple surfaces with a shared hole segmentation of the neural canal opening in SD-OCT volumes," *Lect. Notes Comput. Sci.* **8673**, 739–746 (2014).

37. Z. Hu et al., "Automated segmentation of neural canal opening and optic cup in 3D spectral optical coherence tomography volumes of the optic nerve head," *Invest. Ophthalmol. Visual Sci.* **51**(11), 5708–5717 (2010).

38. J. Weickert, *Anisotropic Diffusion in Image Processing*, Universität Kaiserslautern, Kaiserslautern (1996).

39. J. Soares et al., "Retinal vessel segmentation using the 2-D Gabor wavelet and supervised classification," *IEEE Trans. Med. Imaging* **25**, 1214–1222 (2006).

40. K. Gawlik et al., "An active contour method for ILM segmentation in ONH volume scans in retinal OCT," submitted to *Biomed. Opt. Express* (2018).

41. W. E. Lorensen and H. E. Cline, "Marching cubes: a high resolution 3D surface construction algorithm," in *Proc. of the 14th Annual Conf. on Computer Graphics and Interactive Techniques, SIGGRAPH*, pp. 163–169, ACM (1987).

42. S. K. Yadav, U. Reitebuch, and K. Polthier, "Robust and high fidelity mesh denoising," *IEEE Trans. Visual Comput. Graphics* **PP**(99), 1–1 (2018).

43. A. Fitzgibbon, M. Pilu, and R. B. Fisher, "Direct least square fitting of ellipses," *IEEE Trans. Pattern Anal. Mach. Intell.* **21**(5), 476–480 (1999).

44. S. K. Yadav, U. Reitebuch, and K. Polthier, "Mesh denoising based on normal voting tensor and binary optimization," *IEEE Trans. Visual Comput. Graphics* **24**(8), 2366–2379 (2018).

45. C. A. Schneider, W. S. Rasband, and K. W. Eliceiri, "NIH image to ImageJ: 25 years of image analysis," *Nat. Methods* **9**, 671–675 (2012).

46. L. Pierro et al., "Macular thickness interoperator and intra-operator reproducibility in healthy eyes using 7 optical coherence tomography instruments," *Am. J. Ophthalmol.* **150**, 199–204.e1 (2010).

47. H. Zimmermann et al., "Optical coherence tomography for retinal imaging in multiple sclerosis," *Degener. Neurol. Neuromuscular Dis.* **4**, 153–162 (2014).

48. A. Petzold et al., "The investigation of acute optic neuritis: a review and proposed protocol," *Nat. Rev. Neurol.* **10**, 447–458 (2014).

49. A. U. Brandt et al., "Frequent retinal ganglion cell damage after acute optic neuritis," *Mult. Scler. Relat. Disord.* **22**, 141–147 (2018).

50. J. Sepulcre et al., "Diagnostic accuracy of retinal abnormalities in predicting disease activity in MS," *Neurology* **68**, 1488–1494 (2007).

51. P. Albrecht et al., "Degeneration of retinal layers in multiple sclerosis subtypes quantified by optical coherence tomography," *Mult. Scler. J.* **18**, 1422–1429 (2012).

52. D.-C. Tian et al., "Bidirectional degeneration in the visual pathway in neuromyelitis optica spectrum disorder (NMOSD)," *Mult. Scler. J.* 135245851772760 (2017).

53. S. Lee et al., "Atlas-based shape analysis and classification of retinal optical coherence tomography images using the functional shape (fshape) framework," *Med. Image Anal.* **35**(Suppl. C), 570–581 (2017).

Biographies for the authors are not available.

Normative Data and Minimally Detectable Change for Inner Retinal Layer Thicknesses Using a Semi-automated OCT Image Segmentation Pipeline

Seyedamirhosein Motamedi[1], Kay Gawlik[1], Noah Ayadi[1], Hanna G. Zimmermann[1], Susanna Asseyer[1], Charlotte Bereuter[1], Janine Mikolajczak[1], Friedemann Paul[1,2,3], Ella Maria Kadas[1] and Alexander Ulrich Brandt[1,4*]

[1] NeuroCure Clinical Research Center, Charité-Universitätsmedizin Berlin, Corporate Member of Freie Universität Berlin, Humboldt-Universität zu Berlin, and Berlin Institute of Health, Berlin, Germany, [2] Experimental and Clinical Research Center, Max Delbrück Center for Molecular Medicine and Charité-Universitätsmedizin Berlin, Corporate Member of Freie Universität Berlin, Humboldt-Universität zu Berlin, and Berlin Institute of Health, Berlin, Germany, [3] Department of Neurology, Charité-Universitätsmedizin Berlin, Corporate Member of Freie Universität Berlin, Humboldt-Universität zu Berlin, and Berlin Institute of Health, Berlin, Germany, [4] Department of Neurology, University of California, Irvine, Irvine, CA, United States

Neurodegenerative and neuroinflammatory diseases regularly cause optic nerve and retinal damage. Evaluating retinal changes using optical coherence tomography (OCT) in diseases like multiple sclerosis has thus become increasingly relevant. However, intraretinal segmentation, a necessary step for interpreting retinal changes in the context of these diseases, is not standardized and often requires manual correction. Here we present a semi-automatic intraretinal layer segmentation pipeline and establish normative values for retinal layer thicknesses at the macula, including dependencies on age, sex, and refractive error. Spectral domain OCT macular 3D volume scans were obtained from healthy participants using a Heidelberg Engineering Spectralis OCT. A semi-automated segmentation tool (SAMIRIX) based on an interchangeable third-party segmentation algorithm was developed and employed for segmentation, correction, and thickness computation of intraretinal layers. Normative data is reported from a 6 mm Early Treatment Diabetic Retinopathy Study (ETDRS) circle around the fovea. An interactive toolbox for the normative database allows surveying for additional normative data. We cross-sectionally evaluated data from 218 healthy volunteers (144 females/74 males, age 36.5 ± 12.3 years, range 18–69 years). Average macular thickness (MT) was 313.70 ± 12.02 μm, macular retinal nerve fiber layer thickness (mRNFL) 39.53 ± 3.57 μm, ganglion cell and inner plexiform layer thickness (GCIPL) 70.81 ± 4.87 μm, and inner nuclear layer thickness (INL) 35.93 ± 2.34 μm. All retinal layer thicknesses decreased with age. MT and GCIPL were associated with sex, with males showing higher thicknesses. Layer thicknesses were also positively associated with each other. Repeated-measurement reliability for the manual correction of automatic intraretinal segmentation results was

excellent, with an intra-class correlation coefficient >0.99 for all layers. The SAMIRIX toolbox can simplify intraretinal segmentation in research applications, and the normative data application may serve as an expandable reference for studies, in which normative data cannot be otherwise obtained.

1. INTRODUCTION

Optical coherence tomography (OCT) allows non-invasive high-resolution *in vivo* imaging of the retina (1). Spectral domain OCT (SD-OCT) provides 3D volume scans of the retina, and intraretinal segmentation of macular volume scans enables quantitative OCT applications in neurodegenerative and autoimmune neuroinflammatory disorders (2, 3). The inner retinal layers, in particular, are currently of pivotal interest for several neurologic disorders. For example, the combined macular ganglion cell and inner plexiform layer (GCIPL) thickness reflects disease severity and activity in patients with multiple sclerosis (MS) (4) and is suggested for monitoring disease activity in MS (5). GCIPL might further serve to identify neurodegeneration already very early on in the disease (6), and could thus be used as a marker for assessing the individual risk of a patient at onset for an active disease course (7). GCIPL is also suggested as a sensitive marker for attack severity in acute optic neuritis (8, 9). The inner nuclear layer (INL), on the other hand, is a marker for inflammatory disease activity in MS and might be utilized to monitor treatment response (10–12). In neuromyelitis optica spectrum disorders (NMOSD), the INL might be affected as part of an autoimmune reaction against Müller cells (13), which could lead in turn to progressive GCIPL loss (14).

Intraretinal layer segmentation is a crucial step in measuring GCIPL or INL changes. In recent years, many algorithms for intraretinal layer segmentation have been developed, and are now routinely implemented in clinical OCT devices or are available as external tools for research (15). While reliability in healthy eyes is usually good (16), many scans in diseases with macroscopic retinal changes or signal quality issues caused by more difficult OCT measurement in vision-impaired individuals require quality control and manual correction (17). Proper user interfaces for manual correction of automatic segmentation results are not always available, having led to many studies with questionable OCT data based on very small regions of interest (6) or inappropriate quality control (17).

Many studies have investigated intraretinal layer thicknesses in healthy eyes to establish normative reference values, recently e.g., Invernizzi et al. (18). Clinical features like age, sex, and axial length have been reported to physiologically affect intraretinal layer thicknesses (18, 19). But normative data studies are often only applicable in a narrow context depending on the selected samples and the methodology used, and data from studies from Asia, or as a control for different diseases, are not necessarily applicable in the context of neuroinflammatory diseases in European or North American populations.

In this study we aimed (a) to establish normative values for inner intraretinal layer thicknesses in a healthy Caucasian population and age/sex distribution suitable for typical autoimmune neuroinflammatory disorders, and (b) to evaluate layer thicknesses in association with age and sex. For this task we developed an easily usable and adaptable intraretinal segmentation pipeline based on an interchangeable third-party segmentation algorithm (20) as well as a survey tool for additional normative data, which together allow data surveys also beyond the scope of this study. Both are made available as an open source application along with this publication.

2. MATERIALS AND METHODS

2.1. Study Population

We queried our institute's research database to create a normative OCT database. The database contained healthy control data from two multimodal register studies aiming to evaluate quantitative measurements of neuro-axonal damage in MS and other neuroinflammatory disorders who were recruited from July 2010 to March 2018 at the NeuroCure Clinical Research Center at the Charité-Universitätsmedizin Berlin. Each participant underwent an examination of both eyes with Spectralis SD-OCT. Retrospective inclusion criteria for the present study were participants in a healthy condition aged between 18 and 70 years, Caucasian ethnicity, and high-quality macular OCT scans (signal strength more than 15 dB). Exclusion criteria were any neurological condition, any other disorder known to affect the retina (i.e., diabetes), any eye disease affecting the retina (i.e., glaucoma), any relevant pathological finding in the neurovisual examination performed by experienced optometrists, and a refractive error above ±6 diopters. Twenty high quality macular OCT scans (signal strength more than 15 dB) of NMOSD patients all with the history of optic neuritis (ON) were randomly selected from our database to test the performance of the segmentation pipeline presented in this study.

The study was approved by the ethics committee of Charité–Universitätsmedizin Berlin and conducted according to the Declaration of Helsinki in its currently applicable version. All participants gave written informed consent.

2.2. Optical Coherence Tomography

All OCT measurements were carried out with a Spectralis SD-OCT and Heidelberg Eye Explorer (HEYEX) version 5.7.5.0 (Heidelberg Engineering, Heidelberg, Germany), by eight individual operators, with automatic real-time (ART) function for image averaging and an activated eye tracker in a dimly lit room. Macular 3D volumes were assessed by a custom scan

comprising 61 vertical B-scans (each with 768 A-Scans, with ART of 13 frames) with a scanning angle of 30 × 25° focusing on the fovea. All scans were quality controlled according to the OSCAR-IB criteria (21) and reporting adheres to APOSTEL recommendations (22). Scans not passing the quality control were excluded from analysis.

The macular scans were exported from the device and stored in HEYEX Vol file format (*.vol files), and then intraretinal segmentation was performed using the segmentation pipeline as described below. All segmentation results were quality controlled and manually corrected in case of errors by an experienced grader. In the end, the thickness data was calculated and stored in a CSV file format (.csv) for further analysis. The Early Treatment Diabetic Retinopathy Study (ETDRS) macular map, as described by the ETDRS research group (23), were used for this study. We report average macular thickness (MT), macular retinal nerve fiber layer thickness (mRNFL), combined ganglion cell and inner plexiform layer thickness (GCIPL), and inner nuclear layer thickness (INL) in the entire ETDRS macular map (the 6 mm diameter circular area around the fovea). Other layer thicknesses (e.g., outer retinal layers) and the thicknesses in different sectors of the ETDRS macular map can be studied using the provided *shiny* application and source data (**Supplementary Material**).

2.3. Intraretinal Segmentation

Intraretinal segmentation, manual correction, and thickness data export of all macular scans were done using a custom-developed intraretinal segmentation pipeline (SAMIRIX). SAMIRIX modularly includes import filters for OCT data, a third-party segmentation algorithm, a user interface for controlling and correcting segmentation results, and batch-operations for processing multiple OCT images (**Figure 1A**).

SAMIRIX was developed in MATLAB (R2017a, MathWorks, Natick, MA, USA) and the user interface OCT-Marker was written in C++11, by using Qt5, Boost, and OpenCV libraries.

2.3.1. Segmentation Algorithm

As a segmentation algorithm we used OCTLayerSegmentation (20), which has been released as a package of AURA Tools on NITRC (https://www.nitrc.org/projects/aura_tools/). We chose OCTLayerSegmentation, because it showed good performance and accuracy with an overall absolute error of 3.5 μm by combining a machine learning approach for boundary classification (random forest classification) and a robust state-of-the-art graph-cut algorithm boundary refinement (optimal graph search) in a previous study (24). OCTLayerSegmentation delineates the inner limiting membrane (ILM), external limiting membrane (ELM), Bruch membrane (BM), and the boundaries between the retinal nerve fiber layer and ganglion cell layer (RNFL-GCL), inner plexiform layer and inner nuclear layer (IPL-INL), inner nuclear layer and outer plexiform layer (INL-OPL), outer plexiform layer and outer nuclear layer (OPL-ONL), inner and outer segments (ISOS), and outer photoreceptor tips and retinal pigment epithelium (OPT-RPE) (**Figure 1B**). These
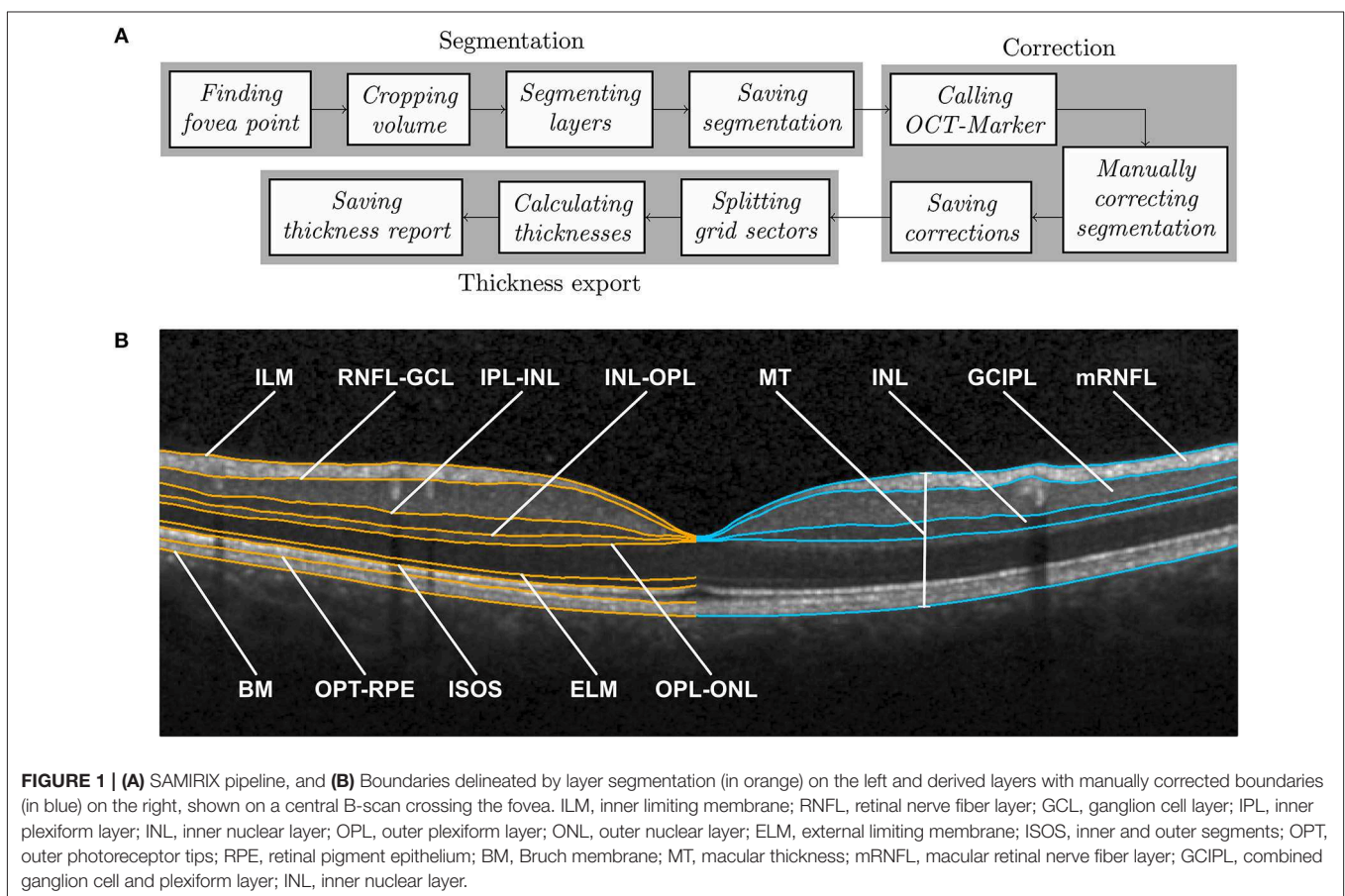
FIGURE 1 | (A) SAMIRIX pipeline, and **(B)** Boundaries delineated by layer segmentation (in orange) on the left and derived layers with manually corrected boundaries (in blue) on the right, shown on a central B-scan crossing the fovea. ILM, inner limiting membrane; RNFL, retinal nerve fiber layer; GCL, ganglion cell layer; IPL, inner plexiform layer; INL, inner nuclear layer; OPL, outer plexiform layer; ONL, outer nuclear layer; ELM, external limiting membrane; ISOS, inner and outer segments; OPT, outer photorec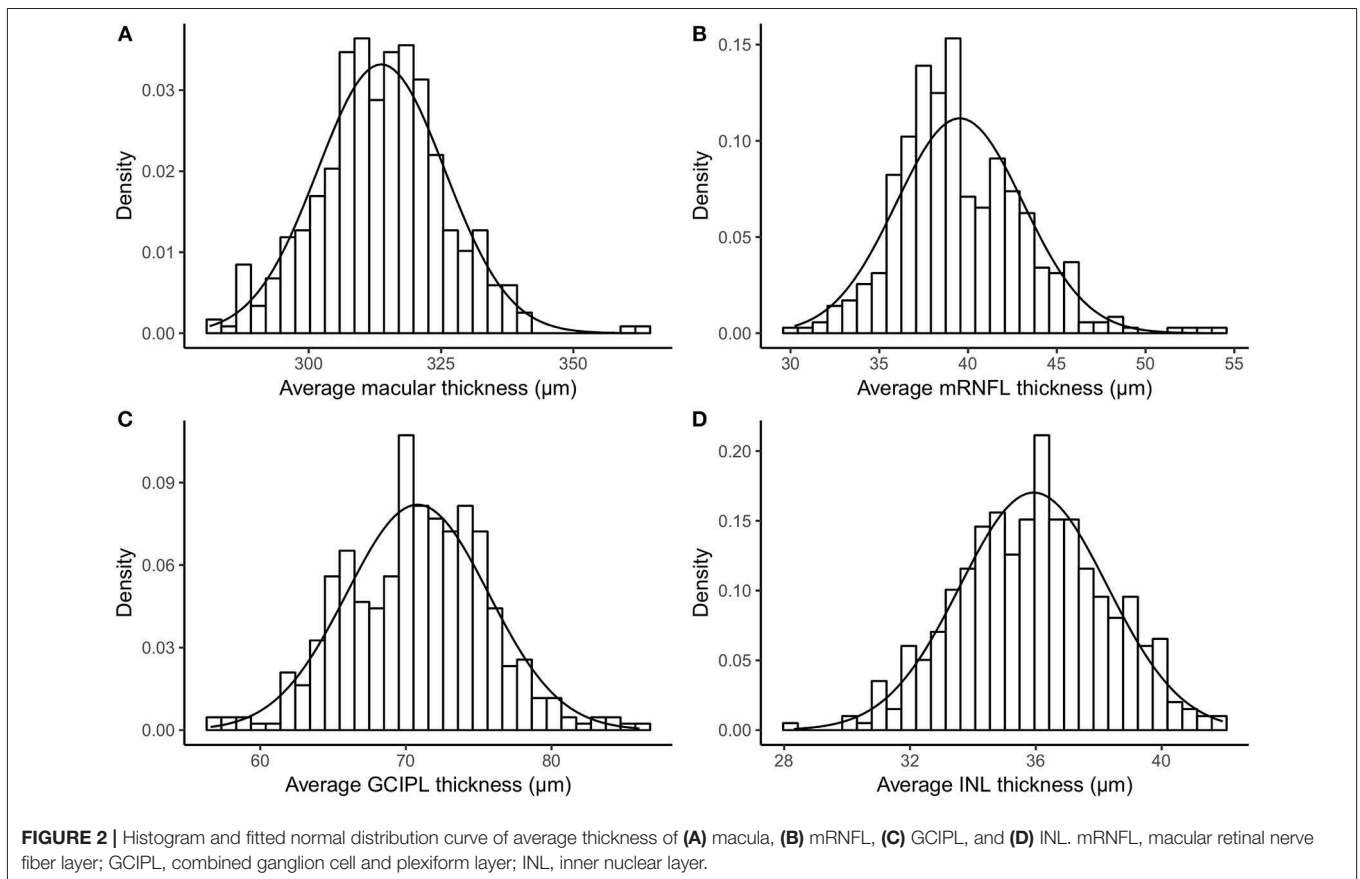eptor tips; RPE, retinal pigment epithelium; BM, Bruch membrane; MT, macular thickness; mRNFL, macular retinal nerve fiber layer; GCIPL, combined ganglion cell and plexiform layer; INL, inner nuclear layer.

boundaries then serve to calculate intraretinal layer areas with nomenclature as suggested by the APOSTEL criteria (22).

For segmentation, the first step is to automatically find the central fovea point of the macular volume scan to be segmented. Based on the segmentation of the ILM and BM by the Heidelberg Engineering Eye Explorer (HEYEX) software, the height difference between the two layers is computed. In order to detect the lowest point of the foveal surface, we look at the minimum of this difference within the 1 mm circular area around the center automatically defined by HEYEX. If several minima are detected, then the median point of them is taken as the center of the foveal pit. The next step is to crop the volume to 6–6 mm square around the fovea, aligned with the main direction of the scan. This was done because many segmentation approaches work with a priori assumption regarding the expected image. The algorithm by Lang et al. used in this version of SAMIRIX works well with this volume, which was also used by the original developers of the algorithm (20). After being cropped, the volume is segmented by the integrated 3rd-party segmentation algorithm (20). The segmentation results are then read by SAMIRIX and saved alongside the volume in a single file.

2.3.2. User Interface for Manual Correction

For quality control and manual correction, we developed a graphical user interface (OCT-Marker). In the first step, the scan to be checked and corrected if necessary, is opened in OCT-Marker. A Piecewise Cubic Hermite Interpolating Polynomial (PCHIP) based correction method with defined control points is provided to the user to ease the correction process. This enables modifications on the segmentation results while going through the volume scan, B-scan by B-scan. When the correction is done, the modified segmentation is written and saved over the previous one in the data file.

2.3.3. Data Export and Batch Processing

For thickness data export, the user selects the upper and lower boundaries of the layer, and also the grid in which the thickness is going to be calculated (e.g., ETDRS 6 mm grid). Then, each volume is split into these sectors, and the average thickness of each is computed. At the end, the calculated values are written and saved in a comma separated values (csv) file.

SAMIRIX also offers the possibility of performing batch segmentation. For this purpose, the selected volumes are taken through the steps in the segmentation module, one by one. Also, in the thickness export module, the first two steps are repeated for each volume, and then the end result consists in a single thickness report saved in a single table. SAMIRIX only works with Spectralis OCT scans in HEYEX Vol file format (*.vol files). Screenshots from SAMIRIX and OCT-Marker are provided in **Supplementary Material**.

2.4. Statistical Analysis

Statistical analysis was done in R [Version 3.4.4 (25)]. Exploratory data analysis and data visualization were performed using the ggplot2 package (26). For assessment of consistency, the intra-class correlation coefficient (ICC) and 95% confidence intervals were estimated using the ICC package (27), based on the variance components from a one-way ANOVA. The coefficient of variation (CV), standard error of measurement (SEM), and minimum detectable change (MDC) for inter-rater and intra-rater consistency analysis were calculated based on the formulas described by Beckerman et al. (28). SEM and MDC, the latter sometimes also called smallest real difference (SRD), are statistical approaches to estimate the minimally needed difference between two measurements that a method is able to detect (28), and is used in this study as a measure to quantify the amount of noise. In this study, an ICC >0.9 was considered as high, between 0.8 and 0.9 as moderate, and <0.8 as insufficient, as suggested by Vaz et al. (29).

Analysis of OCT values against age, sex, and refractive error was performed by linear mixed effect models (LMM), including inter-eye within-patient correlations as a random effect [lme4 package (30), and lmerTest package (31)]. The conditional and marginal coefficients of determination were calculated with pseudo R-squared [MuMIn package (32)]. The correlation of OCT values was assessed using Pearson's product-moment correlation [stats package (25)] and regression analysis was carried out using LMM with the inclusion of inter-eye within-patient correlations as a random effect. For this study, p-values below 0.05 were considered significant.

All statistical and exploratory results of this study were established in an interactive HTML document using R Markdown (33) and Shiny (34) packages. R Markdown is a framework to run codes written in R and generates reports based on the output of the codes. By using Shiny R package, the reports can be turned into interactive web applications. The documents based on R Markdown and Shiny packages can be deployed on web servers and are therefore accessible, like web pages. A screenshot of the interactive HTML document is provided in the **Supplementary Material**.

3. RESULTS

Initially, macula scans of 438 eyes of 219 subjects were collected from our database according to the inclusion and exclusion criteria, from which the scans from 15 eyes of 14 subjects were excluded due to insufficient scan quality. Therefore, in this study, macula scans of 423 eyes of 218 subjects of Caucasian descent were included, from which 144 (66 %) subjects were females and 74 (34 %) were males. Age ranged between 18 and 69 years, with an average [±standard deviation (SD)] of 36.5 ± 12.27 years. Refractive error was available from a subset of 70 eyes (35 subjects), from which the average was −0.55 ± 1.38 SD diopter with a range between −4.75 and +1.75 diopter.

Table 1 provides descriptive statistics of average MT, mRNFL, GCIPL, and INL thicknesses, including the mean, SD, coefficient of variation, range, first percentile, fifth percentile, ninety-fifth percentile, and ninety-ninth percentile. **Figure 2** shows the distribution of the average layer thicknesses together with an overlaid curve representing normal distribution fitted to each graph.

Additionally, the normative (mean) thickness of the MT, mRNFL, GCIPL, and INL layers in the ETDRS macular map is

shown as heat maps in **Figure 3**, alongside the normative values of the average layer thicknesses of the eyes included in this study in the ETDRS macular map sectors. Descriptive statistics of the layer thicknesses in the ETDRS macular map sectors is provided in **Supplementary Material**.

To test inter-rater reliability, the automatic segmentation results of 44 eyes of 24 subjects from this study were manually corrected by two different experienced graders, who were masked. We then calculated the intra-class correlation coefficient (ICC) and minimum detectable change (MDC) for MT, mRNFL, GCIPL, and INL, which is detailed in **Table 2**.

Intra-rater reliability of the manual correction was tested by manually correcting the segmentation results of the same set of OCT scans from the previous reliability test (44 eyes of 24 subjects) twice by an experienced grader. The MDC (and ICC) was 0.24 (0.99994), 0.31 (0.99861), 0.23 (0.99947), and 0.19 micrometers (0.99890) for MT, mRNFL, GCIPL, and INL, respectively.

Regression analysis of layer thicknesses against age showed significant changes. In particular, MT showed an average decrease of 0.215 μm per year (p-value = 0.001). Likewise, GCIPL thickness decreased by on average 0.088 μm per year (p-value = 0.001). Significant changes of average thickness of mRNFL and INL by aging are also reported; **Table 3** provides detailed results.

Analysis of average layer thicknesses vs. sex revealed significant differences in MT and GCIPL between males and females. Males showed on average 4.18 μm higher MT than females (p-value = 0.015). Further, males had a 1.52 μm thicker GCIPL in comparison to females (p-value = 0.029). As reported in **Table 3**, neither mRNFL nor INL thickness showed significant sex differences.

Since GCIPL and INL are of particular interest, **Figure 4** shows the average GCIPL and INL thicknesses against age. The INL thickness was also plotted against the GCIPL thickness in **Figure 4**. The correlation coefficient between the INL and GCIPL thicknesses was 0.579 (p-value $< 2 \times 10^{-16}$) and the slope (B) of the linear regression was 0.277 [standard error (SE) = 0.022, p-value $< 2 \times 10^{-16}$].

TABLE 1 | Descriptive statistics of average thicknesses in the entire ETDRS macular map.

Average thickness (μm)	Mean ± SD	CV (%)	Min–Max	1st–99th percentile	5th–95th percentile
MT	313.70 ± 12.02	3.83	281.29–362.29	286.53–339.59	294.20–333.25
mRNFL	39.53 ± 3.57	9.03	30.22–54.38	32.41–49.18	34.35–45.68
GCIPL	70.81 ± 4.87	6.87	56.60–86.03	59.00–83.56	63.16–77.95
INL	35.93 ± 2.34	6.52	28.31–41.94	31.00–40.97	32.08–39.87

MT, macular thickness; mRNFL, macular retinal nerve fiber layer; GCIPL, combined ganglion cell and plexiform layer; INL, inner nuclear layer; CV, coefficient of variation; Min, minimum; Max, maximum.

FIGURE 2 | Histogram and fitted normal distribution curve of average thickness of **(A)** macula, **(B)** mRNFL, **(C)** GCIPL, and **(D)** INL. mRNFL, macular retinal nerve fiber layer; GCIPL, combined ganglion cell and plexiform layer; INL, inner nuclear layer.

FIGURE 3 | The mean of the layer thicknesses of all the volumes included in this study in the ETDRS macular map area shown as heat maps, together with the mean and standard deviation (Mean±SD) of the average layer thicknesses in different sectors of the ETDRS macular map. The mRNFL, GCIPL, and INL heat maps have the same scale with the minimum and maximum values of all the three layers (min: 6.28 μm, max: 104.02 μm) in the interest of comparison. The left eyes were mirrored along the vertical axis, and all the images were rotated to be aligned with the fovea and center of the optic nerve head axis. All the numbers are in micrometers. MT, macular thickness; mRNFL, macular retinal nerve fiber layer; GCIPL, combined ganglion cell and plexiform layer; INL, inner nuclear layer; T, temporal; N, nasal; S, superior; I, inferior; ETDRS, Early Treatment Diabetic Retinopathy Study; Min, minimum; Max, maximum.

TABLE 2 | Inter-rater reliability measurements of segmentation corrections.

Average thickness (μm)	ICC	Upper CI	Lower CI	CV	SEM	MDC
MT	0.99984	0.99971	0.99991	0.04464	0.13728	0.38052
mRNFL	0.99350	0.98817	0.99644	0.57594	0.23771	0.65889
GCIPL	0.99794	0.99625	0.99887	0.21960	0.16519	0.45788
INL	0.99734	0.99515	0.99854	0.27271	0.10564	0.29281

MT, macular thickness; mRNFL, macular retinal nerve fiber layer; GCIPL, combined ganglion cell and plexiform layer; INL, inner nuclear layer; ICC, intra-class correlation coefficient; CI, confidence interval; CV, coefficient of variation; SEM, standard error of measurement; MDC, minimum detectable change.

To test the performance of SAMIRIX and to compare it with the performance of the HEYEX software, 20 OCT scans from NMOSD patients, all with a history of optic neuritis (ON) were segmented, and the segmentation results were manually corrected by a grader experienced in both SAMIRIX and HEYEX. The median correction time for SAMIRIX was 7:59 min (minimum: 5:07 min, maximum: 27:22 min), while the median correction time for HEYEX was 10:30 min (minimum: 8:01 min, maximum: 22:01 min). The mean absolute correction in the 6 mm ETDRS circle (the amount of correction for all the five

corrected boundaries ILM, RNFL-GCL, IPL-INL, INL-OPL, and BM divided by the number of A-Scans in the 6 mm ETDRS circle) was also calculated. For the mean absolute correction in SAMIRIX, the median was 0.16 μm (minimum: 0 μm, maximum: 22.45 μm), and in HEYEX, the median was 0.79 μm (minimum: 0.06 μm, maximum: 2.02 μm).

4. DISCUSSION

In this study we present normative data for inner intraretinal layer thicknesses of a large cohort of 218 healthy subjects (423 eyes) of Caucasian ethnicity aged between 18 and 69 years, using Spectralis SD-OCT 3D macular scans.

In our study the average thickness of all investigated layers was associated with age, which is consistent with other studies (35–40). Recently, Invernizzi et al. (18) investigated the association of different intraretinal layer thicknesses in the outer and middle rings and the center of the ETDRS thickness map, with age, and showed no significant association in any regions except the center of macular thickness, which is consistent with some other studies (41, 42). von Hanno et al. (43) suggested a positive association between macular thickness and age up to around 60 years and a negative association afterwards, by studying retinal OCTs of 4,508 eyes. Previous studies investigating retinal thicknesses in relation

TABLE 3 | Regression analysis of average thicknesses against age, sex, and refractive error.

Average thickness (μm)	Against	Mean (SD)	B	SE	P	$R^2_{Marg.}$	$R^2_{Cond.}$
MT	Age (years)		−0.2148	0.0648	**0.0010**	0.0478	0.9679
	Sex: F	312.32 (12.11)	4.1771	1.6941	**0.0145**	0.0268	0.9679
	vs. M	316.38 (11.41)					
	RE (diopter)		−0.3926	0.7013	0.5777	0.0030	0.9644
mRNFL	Age (years)		−0.0523	0.0192	**0.0072**	0.0312	0.8821
	Sex: F	39.46 (3.69)	0.3152	0.5056	0.5337	0.0017	0.8820
	vs. M	39.67 (3.33)					
	RE (diopter)		−0.6067	0.2936	**0.0430**	0.0729	0.8753
GCIPL	Age (years)		−0.0874	0.0263	**0.0010**	0.0480	0.9652
	Sex: F	70.28 (4.98)	1.5150	0.6896	**0.0291**	0.0214	0.9652
	vs. M	71.82 (4.48)					
	RE (diopter)		0.0049	0.2950	0.9869	0	0.9730
INL	Age (years)		−0.0453	0.0125	**0.0004**	0.0558	0.9331
	Sex: F	35.82 (2.40)	0.3526	0.3312	0.2883	0.0050	0.9331
	vs. M	36.15 (2.22)					
	RE (diopter)		0.2394	0.1783	0.1841	0.0209	0.9512

MT, macular thickness; mRNFL, macular retinal nerve fiber layer; GCIPL, combined ganglion cell and plexiform layer; INL, inner nuclear layer; F, female; M, male; vs., versus; RE, refractive error; SD, standard deviation; B, slope; SE, standard error of B; P, p-value; $R^2_{Marg.}$, Marginal R-squared; $R^2_{Cond.}$, Conditional R-Squared. Significant p-values marked in bold.

to sex in a healthy population showed that women had thinner retinal thickness measures than men (36, 40, 41, 43, 44). Our results are in accordance with this for MT and GCIPL, but not for mRNFL and INL, which were both not sex-dependent in our cohort. The analysis using OCT data from the UK Biobank study (67,321 adults) from (45) reported associations among older age, ethnicity, BMI, smoking, and macular thickness.

Inter-rater reliability of manually corrected segmentation results was excellent with ICC values above 0.99 for all layers. MDC, from the inter-rater reliability test, was 0.46 μm for GCIPL, which is higher than the projected annual loss in healthy subjects in this study (0.09 μm per year) and similar to the average annual GCIPL loss reported in patients with MS (−1.1 μm over 2 years) (46). This means that current intraretinal segmentation is not able to reliably detect annual GCIPL loss in an individual MS patient, and further technological improvements in acquisition and image analysis are required to allow this, e.g., for clinical monitoring applications. Intraretinal segmentation of the GCIPL is, however, suited to track optic neuritis associated damage, which is often magnitudes higher than the observed MDC in this study (8, 9). For INL, the inter-rater MDC in our study was 0.29 μm, which is similar to group-wise changes reported with disease activity related effects in the range of 0.35 to 0.71 μm (12). Again, this suggests that current OCT intraretinal segmentation is not able to reliably detect meaningful INL change for this application. A previous multicenter study using the device's own semi-automatic segmentation approach with manual correction produced even higher MDC (17). While previous studies, and our current study only investigated segmentation-based reliability on a single scan, the additional acquisition noise from two different scans is likely to result in even higher MDC in a real world scenario of follow-up measurements. The reported MDC

is below the resolution of the used SD-OCT technology, which suggests that imaging rather than segmentation is the limiting issue in detecting change.

To further support the opposing roles of GCIPL and INL measurements in neuroinflammatory disorders, we investigated their association in healthy controls. Both showed a moderate to strong correlation in our study, indicating that retinal thickness is reflected similarly throughout layers in an individual person. This relationship might be of relevance when interpreting GCIPL and INL in neuroinflammatory diseases, where GCIPL and INL are supposed to change in opposite directions, with GCIPL thickness reduction due to neurodegeneration (4) and INL thickening due to inflammation (12) or in response to ganglion cell loss (10).

The presented semi-automatic OCT image segmentation pipeline, SAMIRIX, provides an accessible and flexible toolbox, which can handle the entire process needed to analyze intra-retinal layer thicknesses on raw SD-OCT images. SAMIRIX is not introducing a new segmentation approach, but rather implements an existing algorithm, and extends it with processing pipelines and comfortable manual correction tools. For research use, SAMIRIX was faster compared to HEYEX, and the initial segmentation more accurate. In a few cases with severely affected eyes, initial automatic segmentation produced large errors. These cases then needed more processing time than with HEYEX, suggesting a potential in improving the initial segmentation approach. Importantly, SAMIRIX offers a transparent open-source segmentation pipeline. Of note, while we compared SAMIRIX to HEYEX, there are other commercial and academic intraretinal segmentation tools available, e.g., Orion (by Voxeleron LLC, https://www.voxeleron.com/orion/) and Iowa Reference Algorithms (by Iowa Institute for Biomedical Imaging, https://www.iibi.uiowa.edu/oct-reference).

FIGURE 4 | (A) The average GCIPL thickness against age, **(B)** the average INL thickness against age, and **(C)** the average INL thickness against the average GCIPL thickness. GCIPL, combined ganglion cell and plexiform layer; INL, inner nuclear layer.
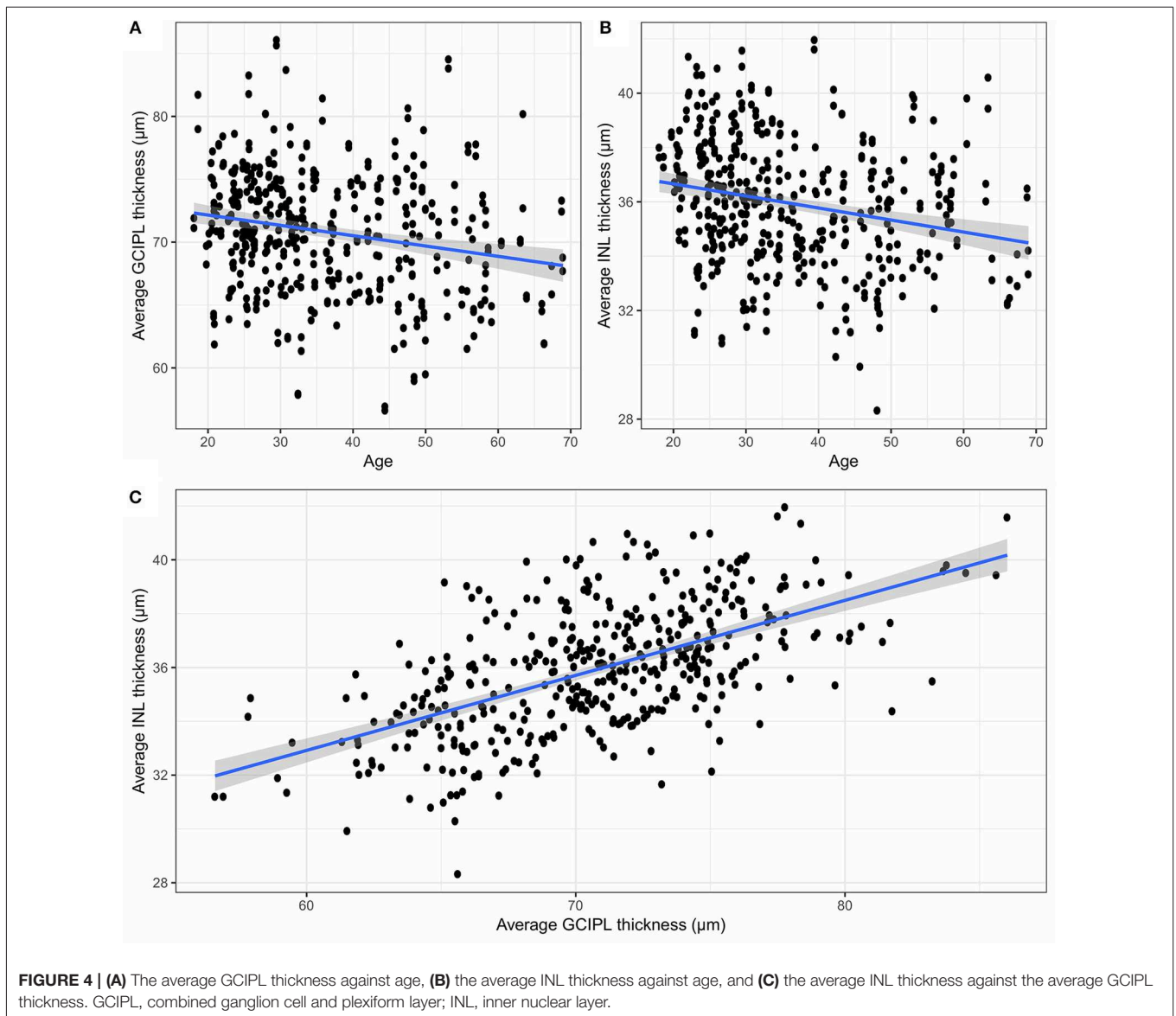
4.1. Strengths and Limitations

A general problem with reporting normative data is not only different optical properties and acquisition strategies of different devices, but also different regions of interest, which are then summarized in the respective thickness or volume measurements (47). While we report 6 mm ETDRS ring thicknesses in micrometers in this study, other regions of interest can be surveyed using the accompanying *shiny* web application. Other strengths of this study are its sample size and the similar age and sex distribution in comparison to typical cohorts of autoimmune neuroinflammatory diseases. A limitation of this study is the cross-sectional design, which impairs inferences about temporal development. The most important limitation is that we included OCT scans from only one device and one scan protocol, which limits generalizability of normative data (47). Particular caution should be taken when interpreting data

acquired with various instruments, since comparative studies revealed that measurements are not directly comparable between different OCT devices (48, 49) and results can even be influenced by simple software upgrades (50). Currently, SAMIRIX is only able to work with the HEYEX Vol file format (*.vol files), which is only available through specific collaborative arrangements with Heidelberg Engineering, which is a clear limitation.

Because this study was done on a Caucasian population, readers should keep in mind that our results are not necessarily applicable to other ethnicities. Grover et al. (42) found Black subjects to have a thinner retinal thickness compared to Caucasian subjects, while Tariq et al. (51) showed that average inner macula was significantly thicker in Caucasian than East Asian and South Asian children, with South Asian children having the thinnest values. These findings were also confirmed by Girkin et al. (35), which reported that Hispanic and Indian

participants showed higher thickness compared to Europeans and Africans.

DATA AVAILABILITY STATEMENT

All analyses of this study are combined in a single R markdown code embedding R shiny interactive applications, which is provided alongside the raw data as **Supplementary Material** as well as in a public repository, in https://github.com/neurodial/am-HC-project-analysis-public.git. A copy of the source code of SAMIRIX which was used in this study and described in this paper is also provided as **Supplementary Material**. An up-to-date version of SAMIRIX can be found in a public repository with the address of https://github.com/neurodial/am_SAMIRIX.git. Additionally, the markdown HTML document was deployed to a server and is ready-to-use, available under http://shiny-apps.neurodial.de/shiny/am-HC-project-analysis-public/HC_traditional_params_markdown.Rmd with the username of "guest_user" and the password of "NeuroDiaL."

ETHICS STATEMENT

The study was approved by the ethics committee of Charité–Universitätsmedizin Berlin and conducted according to the Declaration of Helsinki in its currently applicable version. All participants gave written informed consent.

AUTHOR CONTRIBUTIONS

FUNDING

ACKNOWLEDGMENTS

SUPPLEMENTARY MATERIAL

The Supplementary Material for this article can be found online at: https://www.frontiersin.org/articles/10.3389/fneur.2019.01117/full#supplementary-material

REFERENCES

1. Huang D, Swanson EA, Lin CP, Schuman JS, Stinson WG, Chang W, et al. Optical coherence tomography. *Science* (1991) 254:1178–81.
2. Oertel FC, Zimmermann H, Paul F, Brandt AU. Optical coherence tomography in neuromyelitis optica spectrum disorders: potential advantages for individualized monitoring of progression and therapy. *EPMA J.* (2017) 9:21–33. doi: 10.1007/s13167-017-0123-5
3. Oertel FC, Zimmermann HG, Brandt AU, Paul F. Novel uses of retinal imaging with optical coherence tomography in multiple sclerosis. *Expert Rev Neurother.* (2019) 19:31–43.doi: 10.1080/14737175.2019.1559051
4. Petzold A, Balcer LJ, Calabresi PA, Costello F, Frohman TC, Frohman EM, et al. Retinal layer segmentation in multiple sclerosis: a systematic review and meta-analysis. *Lancet Neurol.* (2017) 16:797–812. doi: 10.1016/S1474-4422(17)30278-8
5. Brandt AU, Martinez-Lapiscina EH, Nolan R, Saidha S. Monitoring the course of MS with optical coherence tomography. *Curr Treat Options Neurol.* (2017) 19:15.doi: 10.1007/s11940-017-0452-7
6. Oberwahrenbrock T, Ringelstein M, Jentschke S, Deuschle K, Klumbies K, Bellmann-Strobl J, et al. Retinal ganglion cell and inner plexiform layer thinning in clinically isolated syndrome. *Mult Scler J.* (2013) 19:1887–95. doi: 10.1177/1352458513489757
7. Zimmermann HG, Knier B, Oberwahrenbrock T, Behrens J, Pfuhl C, Aly L, et al. Association of retinal ganglion cell layer thickness with future disease activity in patients with clinically isolated syndrome. *JAMA Neurol.* (2018) 75:1071–9. doi: 10.1001/jamaneurol.2018.1011

8. Brandt AU, Specovius S, Oberwahrenbrock T, Zimmermann HG, Paul F, Costello F. Frequent retinal ganglion cell damage after acute optic neuritis. *Mult Scler Relat Disord.* (2018) 22:141–7. doi: 10.1016/j.msard.2018.04.006
9. Soelberg K, Specovius S, Zimmermann HG, Grauslund J, Mehlsen JJ, Olesen C, et al. Optical coherence tomography in acute optic neuritis: a population-based study. *Acta Neurol Scand.* (2018) 138:566–73. doi: 10.1111/ane.13004
10. Brandt AU, Oberwahrenbrock T, Kadas EM, Lagreze WA, Paul F. Dynamic formation of macular microcysts independent of vitreous traction changes. *Neurology.* (2014) 83:73–7. doi: 10.1212/wnl.0000000000000545
11. Kaufhold F, Zimmermann H, Schneider E, Ruprecht K, Paul F, Oberwahrenbrock T, et al. Optic neuritis is associated with inner nuclear layer thickening and microcystic macular edema independently of multiple sclerosis. *PLoS ONE.* (2013) 8:e71145. doi: 10.1371/journal.pone.0071145
12. Knier B, Schmidt P, Aly L, Buck D, Berthele A, Mühlau M, et al. Retinal inner nuclear layer volume reflects response to immunotherapy in multiple sclerosis. *Brain.* (2016) 139:2855–63. doi: 10.1093/brain/aww219
13. Oertel FC, Kuchling J, Zimmermann H, Chien C, Schmidt F, Knier B, et al. Microstructural visual system changes in AQP4-antibody–seropositive NMOSD. *Neurol Neuroimmunol Neuroinflamm.* (2017) 4:e334. doi: 10.1212/NXI.0000000000000334
14. Oertel FC, Havla J, Roca-Fernández A, Lizak N, Zimmermann H, Motamedi S, et al. Retinal ganglion cell loss in neuromyelitis optica: a longitudinal study. *J Neurol Neurosurg Psychiatry.* (2018) 89:1259–65. doi: 10.1136/jnnp-2018-318382
15. Tian J, Varga B, Tatrai E, Fanni P, Somfai GM, Smiddy WE, et al. Performance evaluation of automated segmentation software on optical coherence tomography volume data. *J Biophoton.* (2016) 9:478–89. doi: 10.1002/jbio.201500239

16. Ctori I, Huntjens B. Repeatability of foveal measurements using spectralis optical coherence tomography segmentation software. *PLoS ONE.* (2015) 10:e0129005. doi: 10.1371/journal.pone.0129005

17. Oberwahrenbrock T, Traber GL, Lukas S, Gabilondo I, Nolan R, Songster C, et al. Multicenter reliability of semiautomatic retinal layer segmentation using OCT. *Neurol Neuroimmunol Neuroinflamm.* (2018) 5:e449. doi: 10.1212/NXI.0000000000000449

18. Invernizzi A, Pellegrini M, Acquistapace A, Benatti E, Erba S, Cozzi M, et al. Normative data for retinal-layer thickness maps generated by spectral-domain OCT in a white population. *Ophthalmol Retina.* (2018) 2:808–15.e1. doi: 10.1016/j.oret.2017.12.012

19. Ooto S, Hangai M, Tomidokoro A, Saito H, Araie M, Otani T, et al. Effects of age, sex, and axial length on the three-dimensional profile of normal macular layer structures. *Investig Opthalmol Vis Sci.* (2011) 52:8769. doi: 10.1167/iovs.11-8388

20. Lang A, Carass A, Hauser M, Sotirchos ES, Calabresi PA, Ying HS, et al. Retinal layer segmentation of macular OCT images using boundary classification. *Biomed Opt Express.* (2013) 4:1133–52. doi: 10.1364/BOE.4.001133

21. Tewarie P, Balk L, Costello F, Green A, Martin R, Schippling S, et al. The OSCAR-IB consensus criteria for retinal OCT quality assessment. *PLoS ONE.* (2012) 7:e34823. doi: 10.1371/journal.pone.0034823

22. Cruz-Herranz A, Balk LJ, Oberwahrenbrock T, Saidha S, Martinez-Lapiscina EH, Lagreze WA, et al. The APOSTEL recommendations for reporting quantitative optical coherence tomography studies. *Neurology.* (2016) 86:2303–9. doi: 10.1212/WNL.0000000000002774

23. ETDRS Research Group. Grading diabetic retinopathy from stereoscopic color fundus photographs–an extension of the modified Airlie House classification. ETDRS report number 10. Early Treatment Diabetic Retinopathy Study Research Group. *Ophthalmology.* (1991) 98:786–806.

24. Oberwahrenbrock T, Jost R, Zimmermann H, Beckers I, Paul F, Brandt AU. Signal quality dependency of intra-retinal segmentation algorithms. In: *ECTRIMS Online Library* (2016). p. 146399. Available online at: https://onlinelibrary.ectrims-congress.eu/ectrims/2016/32nd/146399/timm.oberwahrenbrock.signal.quality.dependency.of.intra-retinal.segmentation.html

25. R Core Team. *R: A Language and Environment for Statistical Computing.* Vienna: R Core Team (2018). Available online at: https://www.R-project.org/

26. Wickham H. *ggplot2: Elegant Graphics for Data Analysis.* New York, NY: Springer-Verlag (2009). Available online at: http://ggplot2.org

27. Wolak ME, Fairbairn DJ, Paulsen YR. Guidelines for estimating repeatability. *Methods Ecol Evol.* (2012) 3:129–37. doi: 10.1111/j.2041-210X.2011.00125.x

28. Beckerman H, Roebroeck ME, Lankhorst GJ, Becher JG, Bezemer PD, Verbeek AL. Smallest real difference, a link between reproducibility and responsiveness. *Qual Life Res.* (2001) 10:571–8. doi: 10.1023/a:1013138911638

29. Vaz S, Falkmer T, Passmore AE, Parsons R, Andreou P. The case for using the repeatability coefficient when calculating test–retest reliability. *PLoS ONE.* (2013) 8:e73990. doi: 10.1371/journal.pone.0073990

30. Bates D, Mächler M, Bolker B, Walker S. Fitting linear mixed-effects models using lme4. *J Stat Softw.* (2015) 67:1–48. doi: 10.18637/jss.v067.i01

31. Kuznetsova A, Brockhoff PB, Christensen RHB. lmerTest package: tests in linear mixed effects models. *J Stat Softw.* (2017) 82:1–26. doi: 10.18637/jss.v082.i13

32. Barton K. *MuMIn: Multi-Model Inference* (2018). R package version 1.40.4. Available online at: https://CRAN.R-project.org/package=MuMIn

33. Allaire J, Horner J, Marti V, Porte N. *Markdown: 'Markdown' Rendering for R; 2017.* R package version 0.8. Available online at: https://CRAN.R-project.org/package=markdown

34. Chang W, Cheng J, Allaire J, Xie Y, McPherson J. *Shiny: Web Application Framework for R* (2017). R package version 1.0.5. Available online at: https://CRAN.R-project.org/package=shiny

35. Girkin CA, McGwin G, Sinai MJ, Sekhar GC, Fingeret M, Wollstein G, et al. Variation in optic nerve and macular structure with age and race with spectral-domain optical coherence tomography. *Ophthalmology.* (2011) 118:2403–8. doi: 10.1016/j.ophtha.2011.06.013

36. Gupta P, Sidhartha E, Tham YC, Chua DKP, Liao J, Cheng CY, et al. Determinants of macular thickness using spectral domain optical coherence tomography in healthy eyes: the Singapore Chinese eye study. *Investig Opthalmol Vis Sci.* (2013) 54:7968. doi: 10.1167/iovs.13-12436

37. Mitkova-Hristova VT, Konareva-Kostyaneva MI. Macular thickness measurements in healthy eyes using spectral optical coherence tomography. *Folia Med.* (2011) 53:28–33. doi: 10.2478/v10153-011-0064-z

38. Myers CE, Klein BEK, Meuer SM, Swift MK, Chandler CS, Huang Y, et al. Retinal thickness measured by spectral-domain optical coherence tomography in eyes without retinal abnormalities: the Beaver dam eye study. *Am J Ophthalmol.* (2015) 159:445–56.e1. doi: 10.1016/j.ajo.2014.11.025

39. Nieves-Moreno M, de-la Casa JMM, Morales-Fernández L, Sánchez-Jean R, Sáenz-Francés F, García-Feijoó J. Impacts of age and sex on retinal layer thicknesses measured by spectral domain optical coherence tomography with spectralis. *PLoS ONE.* (2018) 13:e0194169. doi: 10.1371/journal.pone.0194169

40. Song WK, Lee SC, Lee ES, Kim CY, Kim SS. Macular thickness variations with sex, age, and axial length in healthy subjects: a spectral domain–optical coherence tomography study. *Investig Opthalmol Vis Sci.* (2010) 51:3913. doi: 10.1167/iovs.09-4189

41. Adhi M, Aziz S, Muhammad K, Adhi MI. Macular thickness by age and gender in healthy eyes using spectral domain optical coherence tomography. *PLoS ONE.* (2012) 7:e37638. doi: 10.1371/journal.pone.0037638

42. Grover S, Murthy RK, Brar VS, Chalam KV. Normative data for macular thickness by high-definition spectral-domain optical coherence tomography (spectralis). *Am J Ophthalmol.* (2009) 148:266–71. doi: 10.1016/j.ajo.2009.03.006

43. von Hanno T, Lade AC, Mathiesen EB, Peto T, Njølstad I, Bertelsen G. Macular thickness in healthy eyes of adults (N = 4508) and relation to sex, age and refraction: the Tromsø Eye Study (2007–2008). *Acta Ophthalmol.* (2016) 95:262–9. doi: 10.1111/aos.13337

44. Duan XR, Liang YB, Friedman DS, Sun LP, Wong TY, Tao QS, et al. Normal macular thickness measurements using optical coherence tomography in healthy eyes of adult Chinese persons: the Handan eye study. *Ophthalmology.* (2010) 117:1585–94. doi: 10.1016/j.ophtha.2009.12.036

45. Patel PJ, Foster PJ, Grossi CM, Keane PA, Ko F, Lotery A, et al. Spectral-domain optical coherence tomography imaging in 67,321 adults. *Ophthalmology.* (2016) 123:829–40. doi: 10.1016/j.ophtha.2015.11.009

46. Balk LJ, Cruz-Herranz A, Albrecht P, Arnow S, Gelfand JM, Tewarie P, et al. Timing of retinal neuronal and axonal loss in MS: a longitudinal OCT study. *J Neurol.* (2016) 263:1323–31.doi: 10.1007/s00415-016-8127-y

47. Oberwahrenbrock T, Weinhold M, Mikolajczak J, Zimmermann H, Paul F, Beckers I, et al. Reliability of intra-retinal layer thickness estimates. *PLoS ONE.* (2015) 10:e0137316. doi: 10.1371/journal.pone.0137316

48. Pierro L, Giatsidis SM, Mantovani E, Gagliardi M. Macular thickness interoperator and intraoperator reproducibility in healthy eyes using 7 optical coherence tomography instruments. *Am J Ophthalmol.* (2010) 150:199–204.e1. doi: 10.1016/j.ajo.2010.03.015

49. Seigo MA, Sotirchos ES, Newsome S, Babiarz A, Eckstein C, Ford E, et al. *In vivo* assessment of retinal neuronal layers in multiple sclerosis with manual and automated optical coherence tomography segmentation techniques. *J Neurol.* (2012) 259:2119–30. doi: 10.1007/s00415-012-6466-x

50. Coric D, Petzold A, Uitdehaag BMJ, Balk LJ. Software updates of OCT segmentation algorithms influence longitudinal assessment of retinal atrophy. *J Neurol Sci.* (2018) 387:16–20. doi: 10.1016/j.jns.2018.01.020

51. Tariq YM, Li H, Burlutsky G, Mitchell P. Ethnic differences in macular thickness. *Clin Exp Ophthalmol.* (2011) 39:893–8. doi: 10.1111/j.1442-9071.2011.02593.x

Temporal visual resolution and disease severity in MS

Noah Ayadi, Jan Dörr, MD, Seyedamirhosein Motamedi, MSc, Kay Gawlik, MSc, Judith Bellmann-Strobl, MD, Janine Mikolajczak, PhD, Alexander U. Brandt, MD, Hanna Zimmermann, PhD,* and Friedemann Paul, MD*

Correspondence
Dr. Dörr
jan-markus.doerr@charite.de

Abstract

Objective
To examine temporal visual resolution assessed as critical flicker frequency (CFF) in patients with MS and to investigate associations with visual system damage and general disability and cognitive function.

Methods
Thirty-nine patients with MS and 31 healthy controls (HCs) were enrolled in this cross-sectional study and underwent CFF testing, high- and low-contrast visual acuity, alertness and information processing speed using the paced auditory serial addition task (PASAT), and retinal optical coherence tomography (OCT). In patients with MS, visual evoked potentials (VEPs) and Expanded Disability Status Scale (EDSS) scores were assessed.

Results
CFF in patients with MS (mean ± SD: 40.9 ± 4.4 Hz) was lower than in HCs (44.8 ± 4.4 Hz, $p <$ 0.001). There was no significant CFF difference between eyes with and without previous optic neuritis (ON). CFF was not associated with visual acuity, VEP latency, the peripapillary retinal nerve fiber layer thickness, and the combined ganglion cell and inner plexiform layer volume. Instead, reduced CFF was associated with worse EDSS scores ($r^2 = 0.26$, $p < 0.001$) and alertness ($r^2 = 0.42$, $p = 0.00042$) but not with PASAT ($p = 0.33$).

Conclusion
CFF reduction in MS occurs independently of ON and structural visual system damage. Its association with the EDSS score and alertness suggests that CFF reflects global disease processes and higher cortical processing rather than focal optic nerve or retinal damage.

Glossary

ART = automatic real-time; **CFF** = critical flicker frequency; **EDSS** = Expanded Disability Status Scale; **GCIP** = ganglion cell and inner plexiform layer; **GEE** = Generalized estimating equation; **HC** = healthy control; **HCVA** = high-contrast visual acuity; **ICC** = intraclass correlation coefficient; **INL** = inner nuclear layer; **LCLA** = Low-contrast letter acuity; **OCT** = optical coherence tomography; **ON** = optic neuritis; **PASAT** = paced auditory serial addition task; **pRNFL** = Peripapillary retinal nerve fiber layer thickness; **RRMS** = relapsing-remitting MS; **RT** = reaction time; **SE** = standard error; **TAP** = Test of Attentional Performance; **TMV** = total macular volume; **VEP** = visual evoked potential.

Afferent visual pathway damage in MS results from acute focal damage, i.e., by optic neuritis (ON) or chronic diffuse damage,[1–3] which leads to visual dysfunction and has a relevant impact on the quality of life of patients.[4] Thus, clinical assessment of the visual pathway by means of high-contrast visual acuity (HCVA), functional assessment by means of visual evoked potentials (VEP),[5] and more recently also structural assessment by optical coherence tomography (OCT) have become integral in diagnosing and monitoring patients with MS.[6]

An intriguing aspect of visual function is the visual temporal resolution, commonly assessed as the critical flicker frequency (CFF).[7] CFF represents the frequency of a pulsed light source, from which an individual perceives the signal as flickering. Braunstein already reported in 1903 that CFF was decreased in optic atrophy and other ophthalmologic conditions.[7,8] From the 1950s onward, CFF was investigated in MS,[9] and decreased CFF was found to relate to ON,[9–11] but independence from ON was also reported.[12,13] Furthermore, higher cortical processes had an impact on CFF in patients with cerebral injuries[14] and hepatic encephalopathy.[15]

Despite these early studies suggesting CFF as a potentially important marker for visual function, it remains unclear how CFF could serve as a marker for monitoring disease severity in MS. Our study is thus aimed at evaluating the potential of CFF measurements by investigating its association with clinical and cognitive assessments and structural visual system damage assessed by OCT.

Methods

Patients and controls

Forty-two patients with relapsing-remitting MS (RRMS) and 31 healthy controls (HCs) were enrolled in this prospective, cross-sectional pilot study. Inclusion criteria were diagnosis of RRMS according to the 2010 revised McDonald criteria[16] (or HC) and age between 18 and 70 years. Exclusion criteria were any comorbidity (e.g., glaucoma, retinal disease, diabetes mellitus, ophthalmologic surgery), which could influence vision or the retina. Patients with MS were recruited consecutively over 5 years (2012–2017) from the NeuroCure Clinical Research Center, Berlin. HCs were recruited from volunteers.

To match the groups for sex and age, the 3 oldest female patients with MS were excluded before analysis, leading to a final number of 39 patients included in the analysis.

All patients with MS underwent clinical assessment and were scored using the Expanded Disability Status Scale (EDSS).[17] A demographic and clinical overview is given in table 1.

Standard protocol approvals, registrations, and patient consents

This study was conducted in line with the strengthening the reporting of observational studies in epidemiology statement[18] and was approved by the local ethics committee (EA1/216/11). It was conducted in accordance with the Declaration of Helsinki in its applicable version and applicable German laws. All participants provided written informed consent.

Table 1 Cohort description

	MS	HC	*p* Value
Participants, N	39	31	
Sex, male/female (N)	13/26	12/19	0.6 (χ^2)
Age/years, mean ± SD (range)	45.9 ± 8.4 (27–66)	45.0 ± 16.1 (20–70)	0.6 (MWU)
Eyes with previous ON, yes/no (N)	28/50		
Time since diagnosis, mo, mean ± SD (range)	156.8 ± 92.3 (24–446)		
EDSS, median (range)	2.5 (0–6)		

Abbreviations: EDSS = Expanded Disability Status Scale; HC = healthy control; MWU = Mann-Whitney *U* test; ON = optic neuritis.

Critical flicker frequency

CFF measurement was performed monocularly using a HEPAtonorm analyzer (nevoLAB GmbH, Maierhöfen, Germany) in a quiet and semidarkened room. The device includes a headset that shields any external light from the participant's eyes and that features intrafoveal visual stimulation with a red luminous diode. The initial light signal of 60 Hz is perceived as continuous by the participant. Participants were instructed to press a stop button as soon as they perceive a flickering signal. When the operator starts the measurement on a hand-held controller, the pulse frequency decreases until it is perceived as flickering. The corresponding pulse frequency is defined as CFF and recorded by the hand-held controlling unit. CFF thresholds were determined monocularly, where each eye was tested 8 times, and the mean CFF (mCFF) value was calculated. All participants underwent a training session with 5 measurements before each initial measurement session.[15,19]

Visual function parameters

HCVA was assessed with the Functional Vision Analyzer Optec 6500P system (Stereo Optical Co, Chicago, IL), as described previously.[20] Testing was performed monocularly under habitual correction and photopic conditions (85 cd/m^2) with Early Treatment of Diabetic Retinopathy Study charts in a simulated distance of 20 ft.[20] Low-contrast letter acuity (LCLA) was assessed binoculary with 2.5% contrast Sloan charts in 2 m distance.[21]

Visual evoked potentials (VEP) were tested using the Dantec Keypoint VEP system (Natus Europe GmbH, Planegg, Germany). The P100 latency was measured using a standard black-and-white checkerboard stimulation (15′/50–60′, at 1 m) and were recorded from the Oz electrode against a Cz reference electrode according to the 10–20 International System. The P100 amplitude was not analyzed.

Alertness and cognitive parameters

Because of time constraints, denial by participants and technical issues, only a subset of 17 patients with MS and 20 HCs underwent a selected task from the computerized test of attentional performance (TAP) battery for alertness testing.[22] The tasks consist of a simple visual reaction time (RT) task without an acoustic warning signal, called tonic alertness task (part A) and a visual RT task preceded by an acoustic warning signal, phasic alertness (part B). To measure alertness, several trials were undertaken by alternating part A and part B. The participant was then asked to respond as fast as possible by pushing a button whenever a cross is displayed.[22] Mean RTs from tests without acoustic warning signal were considered a measure of alertness.

Also because of time constrains, only a subset of 29 patients with MS were tested with the 3-second version of the paced auditory serial addition task (PASAT), a measure of information processing speed.[23] For 14 patients, both alertness and PASAT testing were available.

OCT and intraretinal segmentation

All participants underwent retinal examination using a spectral domain OCT (Spectralis SD-OCT; Heidelberg Engineering, Heidelberg, Germany) using Eye Explorer 1.9.10.0 and automatic real-time (ART) image averaging.[24] Peripapillary retinal nerve fiber layer thickness (pRNFL) was derived from a standard ring scan around the optic nerve head (12°, 1536 A-scans, 16 ≤ ART ≤ 100) using segmentation by the device's software with viewing module 6.0.14.0. A macular volume scan (25° × 30°, 61 B-scans, 768 A-scans per B-scan, 12 ≤ ART ≤ 15) was acquired for total macular volume (TMV) including all retinal layers from the inner limiting membrane and Bruch membrane, as determined by the device's segmentation software within a 6-mm diameter cylinder around the fovea.

Intraretinal segmentation of combined ganglion cell and inner plexiform layer (GCIP) volume and inner nuclear layer (INL) volume was performed on macular scans with the Johns Hopkins OCT layer segmentation method (AURA Tools

Figure 1 Critical flicker frequency measurements in healthy controls
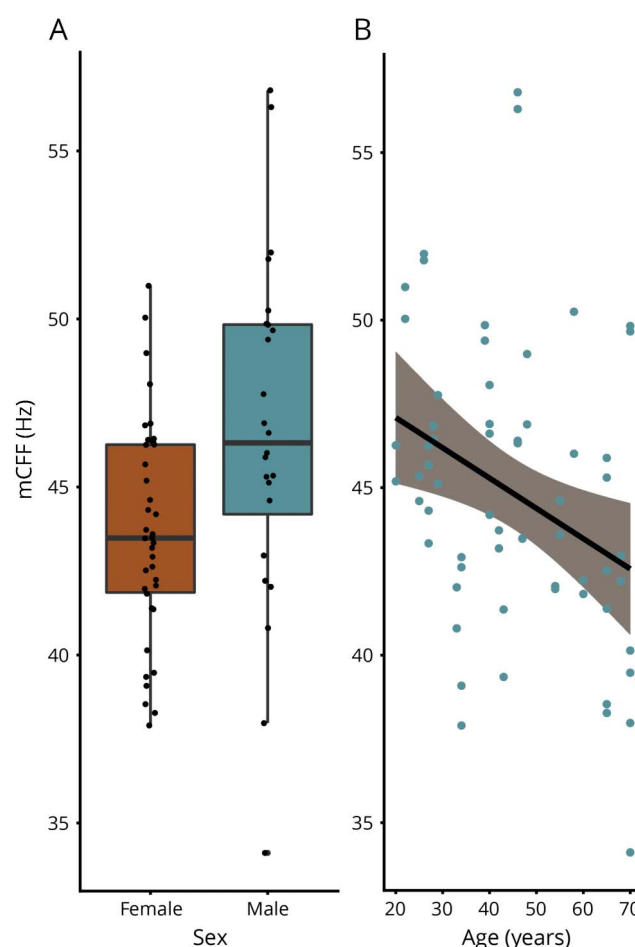
Comparison of CFF measurements between female and male HCs (A) and association of CFF measurements with age (B). HC = healthy control; mCFF = mean critical flicker frequency.

version 1.2)[25] combined with in-house pre-processing (cropping of volume scans to 6 × 6 mm) and postprocessing tools (graphical user interface for manual correction of segmentation results). All OCT scans were carefully checked for retinal changes unrelated to MS, sufficient quality,[26,27] segmentation errors, and were manually corrected by a blinded experienced grader if necessary.

Statistical analysis

Statistical analyses were performed with R version 3.1.2 including geepack package 1.2-0. For demographic comparisons between patients and HCs, the Pearson χ^2 test for sex and nonparametric Mann-Whitney U test for age were used. Generalized estimating equation (GEE) models with working correlation matrix "exchangeable" and corrected for age and sex were used for group comparisons and associations involving eye-related measurements to account for within-subject intereye effects. GEE results are given with regression coefficient (B) and standard error (SE). All measurements were treated as continuous variables, and groups were stratified within patients with MS in ON and non-ON eyes. For the assessment of the test-retest reliability, the intraclass correlation coefficient (ICC) and its 95% confidence intervals were estimated using the R ICC package.[28] As suggested in a previous study, we considered an ICC greater than 0.9 as high and as moderate if between 0.8 and 0.9.[29] Statistical significance was established at $p < 0.05$. A correction for multiple comparisons with the Bonferroni-Holm method was performed for all correlation analyses.[30]

Data availability

All data of this study will be shared by request from any qualified investigator.

Results

CFF in HC

HC had an mCFF of 44.8 ± 4.4 Hz. There was no mCFF difference between female and male HCs (43.70 ± 3.24 vs 46.6 ± 5.3 Hz, B = 1.7188, SE = 4.06, $p = 0.67$) (figure 1A), but lower mCFF was associated with higher age (B = −0.090, SE = 0.043, $p = 0.036$)(figure 1B) in HC. Also, in HC, there was no association between mCFF and HCVA (B = 2.30, SE = 1.99, $p = 0.34$), mCFF and LCLA (B = 0.029, SE = 0.078, $p = 0.71$), or VEP P100 latency (B = 0.044, SE = 0.042, $p = 0.29$). Likewise, alertness did not correlate with mCFF (B = −0.011, SE = 0.0093, $p = 0.25$). Mean results are presented in a supplemental file (table e-1, links.lww.com/NXI/A65). The test-retest reliability in HC was high, with an ICC value of 0.91 (0.87–0.94).

CFF in MS

mCFF in patients with MS was lower than in HC (40.9 ± 4.72 Hz, $p < 0.001$). There was no difference between ON and non-ON eyes (39.7 ± 5.22 vs 41.5 ± 4.33 Hz, $p = 0.094$) (figure 2). mCFF was also not associated with visual function as determined by HCVA, LCLA, VEP latencies, and retinal OCT parameters pRNFL (global and papillomacular bundle),

Figure 2 Critical flicker frequency measurements
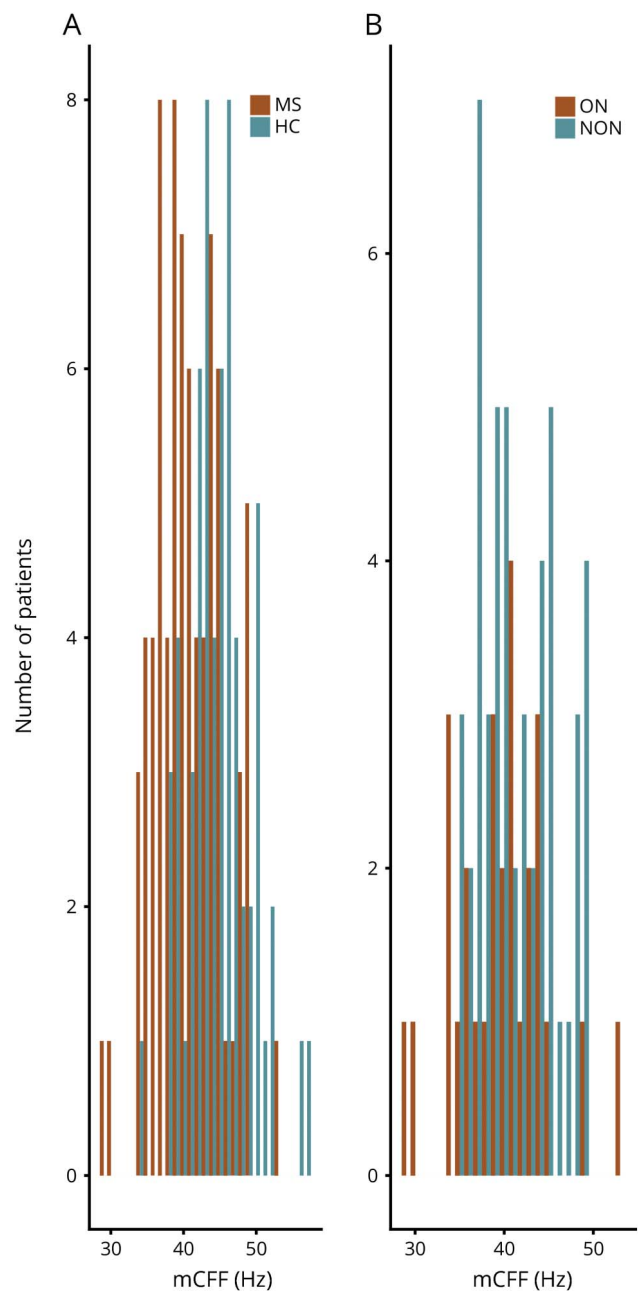
Comparison of CFF measurements between HCs and patients with MS (A) and comparison of CFF measurements between eyes with optic neuritis (ON) and eyes without ON (NON) in patients with MS (B). HC = healthy control; mCFF = mean critical flicker frequency.

GCIP, INL, and TMV (figure 3). Mean results are presented in a supplemental file (table e-1, links.lww.com/NXI/A65). The test-retest reliability was moderate, with an ICC value of 0.89 (0.85–0.92).

CFF and disability

We then investigated whether CFF was associated with overall disability, alertness, and information processing speed in MS patients. Here, overall disability was found as higher EDSS scores, which was inversely correlated with lower

Association of CFF measurements with structural and visual functional parameters: pRNFL (A), GCIP (B), INL (C), TMV (D), HCVA (E), LCLA (F), P100 (G). After Bonferroni-Holm correction, no *p* value remained significant. GCIP = ganglion cell/inner plexiform layer; HCVA = high-contrast visual acuity; INL = inner nuclear layer; LCLA = low-contrast letter acuity; mCFF = mean critical flicker frequency; pRNFL = peripheral retinal nerve fiber layer; TMV = total macular volume; VEP = visual evoked potential.

mCFF (r^2 = 0.26, B = −1.77, SE = 0.50, *p* = 0.00036) (figure 4A). Moreover, lower mCFF was associated with worse alertness (r^2 = 0.42, B = −0.048, SE = 0.014, *p* = 0.00042) (figure 4B), but not with information processing speed, assessed by PASAT (B = 0.063, SE = 0.065, *p* = 0.33). After Bonferroni-Holm correction, the associations between mCFF and alertness and between mCFF and EDSS remained significant. The SD of the CFF measurements was not associated with alertness (B = 0.0015, SE = 0.0035, *p* = 0.68).

Discussion

In this study, we investigated the visual temporal resolution by means of CFF assessment in patients with MS. Key findings are as follows: (1) CFF is reduced in MS compared with HC; (2) CFF is not or only weakly associated with structural and functional measures of afferent visual system damage in MS;

and (3) by contrast, CFF is associated with alertness and clinical disability.

Previous studies consistently reported impaired CFF in MS and ON.[9,10,12] Some investigators interpreted these results as support for cortical damage causing impairment at the central perceptual-discriminative level.[9,31] Thus, they recommended CFF as a general measure of cortical processing capacity.[32] On the other hand, neuroaxonal degeneration in the retina and the visual pathway of patients with MS could affect CFF as well.[9]

Perception of high-frequency stimuli has been suggested to be influenced by retinal ganglion cells.[32] Furthermore, cells of the magnocellular system are confirmed to be more sensitive to higher temporal frequency stimulation than cells of the parvocellular system.[33] Thus, we postulated that CFF could

Figure 4 Critical flicker frequency measurements in patients with MS
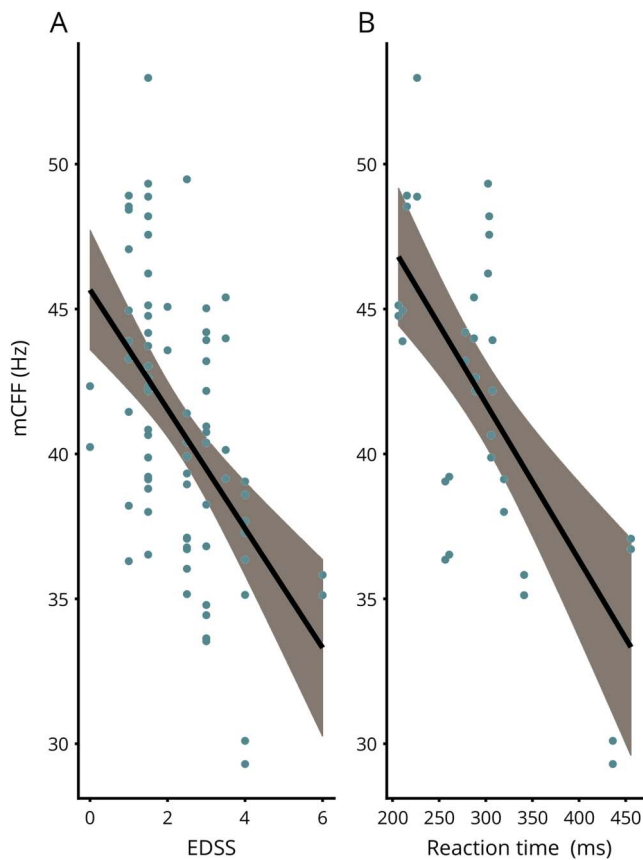
Association of CFF measurements with the EDSS (A) and with reaction time in MS (B). EDSS = Expanded Disability Status Scale; mCFF = mean critical flicker frequency.

reflect integrity of the magnocellular retinal cells' ability to detect higher frequency stimuli,[34] and damage of magnocellular retinal ganglion cells might specifically cause decreased CFF. However, our results show no significant association of CFF with any afferent visual system marker, indicating that retinal neuroaxonal retinal damage had no or only negligible influence to CFF in patients with MS.[34,35] These findings could be explained by effects being small and masked by other associations. However, neuroaxonal retinal damage and demyelination of our MS cohort seem to be comparable to other MS cohorts regarding OCT and VEP measurements.[36,37]

By contrast, our results showed that lower CFF values are associated with longer RTs in a test of alertness, whereas there is no association with CFF SD. This suggests that the association of CFF with alertness is not caused by impaired alertness reducing the ability to comply with the CFF assessment. Tonic alertness refers to a cognitive control of wakefulness and arousal in the absence of a warning and is part of the domain of attention.[38] It is based on the activation of frontoparietal and partly thalamic regions of the right hemisphere.[38] Alertness was shown to be impaired after

appearance of right hemispheric lesions,[38] and we could report an association with MS-related fatigue in an earlier study.[39] This suggests that impaired CFF reflects damage to higher cognitive areas involved in alertness and cognition. Contrarily, the PASAT, which focuses on information processing speed, the cognitive domain most commonly affected in MS, showed no association with CFF in our study.

CFF also correlated with overall disability as represented by the EDSS score. Studies from the 1950/1960s already suggested an association of CFF with general disease disability, but did not investigate this systematically.[9,40]

CFF measurements from our HC are in line with previous studies regarding the mean CFF and an increase of CFF with age.[41] However, although 1 study found sex differences in CFF, this difference was not significant in our study.[42] The ICC values for CFF measurements in HC and MS showed that this method produces reliable results.

Our study has several limitations. Sample sizes of <40 in both MS and control groups might have been insufficient to detect small effects. This is particularly important for a potential effect of a previous ON on the CFF, which was not significant in our study, but gave a low *p* value indicative of a potential power issue. Moreover, the subsets with available TAP and PASAT tests were even smaller, and differences in sample size due to some technical problems and time restrictions in the assessment of the measurements may have resulted in a selection bias potentially weakening our conclusions. We therefore might have missed an association of CFF to information processing as assessed by PASAT. It should also be noted that exclusion of the 3 oldest patients has to be regarded critically because higher age is associated with decreased CFF and impaired visual parameters potentially influencing our findings in regard of the absence of associations between CFF and visual parameters. All visual parameters were measured monocularly except the LCLA because of unavailability at the beginning of the study, potentially reducing the validity of its comparison to monocularly measured CFF values. We did not perform MRI in our study, so we have no information on the association of radiologic disease activity and CFF. Likewise, we have only cross-sectional measurements, so the dynamics of CFF in context of the disease course and any causal inferences remain unclear. It is important to note that most previous studies on CFF in ON and MS were published in the 1950–1970s.[11–13] Thus, test procedures regarding CFF and other parameters might differ, making comparison of our results to these previous ones difficult. The interpretation of the findings of this study is mostly based on the absence of association with functional and visual parameters. Therefore, we believe that adding MRI and conducting longitudinal observations would be the next step in validating CFF measurements in MS.

Our study showed that visual temporal resolution as assessed by CFF is impaired in patients with MS independent of visual and structural visual system damage. Whether CFF

can serve as a marker for overall disease activity warrants further investigation.

Author contributions

Acknowledgment

Study funding

Disclosure

References

1. Martínez-Lapiscina EH, Sanchez-Dalmau B, Fraga-Pumar E, et al. The visual pathway as a model to understand brain damage in multiple sclerosis. Mult Scler 2014;20: 1678–1685.
2. Kuchling J, Brandt AU, Paul F, Scheel M. Diffusion tensor imaging for multilevel assessment of the visual pathway: possibilities for personalized outcome prediction in autoimmune disorders of the central nervous system. EPMA J 2017;8:279–294.
3. Backner Y, Kuchling J, Massarwa S, et al. Anatomical wiring and functional networking changes in the visual system following optic neuritis. JAMA Neurol 2018;75: 287–295.
4. Schinzel J, Zimmermann H, Paul F, et al. Relations of low contrast visual acuity, quality of life and multiple sclerosis functional composite: a cross-sectional analysis. BMC Neurol 2014;14:31.
5. Halliday AM, McDonald WI, Mushin J. Visual evoked response in diagnosis of multiple sclerosis. Br Med J 1973;4:661–664.
6. Brandt AU, Martinez-Lapiscina EH, Nolan R, Saidha S. Monitoring the course of MS with optical coherence tomography. Curr Treat Options Neurol 2017;19:15.
7. Brenton RS, Thompson HS, Maxner C. Critical flicker frequency: a new look at an old test [internet]. In: New Methods of Sensory Visual Testing. New York: Springer; 1989:29–52. Available at: link.springer.com/chapter/10.1007/978-1-4613-8835-7_3.
8. Braunstein EP. Beitrag zur Lehre des intermittierenden Lichtreizes der gesunden und kranken Retina. Z Psychol Physiol Sinnesorgan 1903;33:171–206, 241–288.
9. Parsons OA, Miller PN. Flicker fusion thresholds in multiple sclerosis. AMA Arch Neurol Psychiatry 1957;77:134–139.
10. Titcombe AF, Willison RG. Flicker fusion in multiple sclerosis. J Neurol Neurosurg Psychiatry 1961;24:260–265.
11. Galvin RJ, Regan D, Heron JR. Impaired temporal resolution of vision after acute retrobulbar neuritis. Brain 1976;99:255–268.
12. Daley ML, Swank RL, Ellison CM. Flicker fusion thresholds in multiple sclerosis: a functional measure of neurological damage. Arch Neurol 1979;36:292–295.
13. Patterson VH, Foster DH, Heron J, Mason RJ. Multiple sclerosis: luminance threshold and measurements of temporal characteristics of vision. Arch Neurol 1981;38:687–689.
14. Bender MB, Teuber HL. Disturbances in visual perception following cerebral lesions. J Psychol 1949;28:223–233.
15. Sharma P, Sharma BC, Puri V, Sarin SK. Critical flicker frequency: diagnostic tool for minimal hepatic encephalopathy. J Hepatol 2007;47:67–73.
16. Polman CH, Reingold SC, Banwell B, et al. Diagnostic criteria for multiple sclerosis: 2010 revisions to the McDonald criteria. Ann Neurol 2011;69:292–302.
17. Kurtzke JF. Rating neurologic impairment in multiple sclerosis an expanded disability status scale (EDSS). Neurology 1983;33:1444.
18. von Elm E, Altman DG, Egger M, et al. Strengthening the reporting of observational studies in epidemiology (STROBE) statement: guidelines for reporting observational studies. BMJ 2007;335:806–808.
19. Romero-Gómez M, Córdoba J, Jover R, et al. Value of the critical flicker frequency in patients with minimal hepatic encephalopathy. Hepatology 2007;45:879–885.
20. Bock M, Brandt AU, Kuchenbecker J, et al. Impairment of contrast visual acuity as a functional correlate of retinal nerve fibre layer thinning and total macular volume reduction in multiple sclerosis. Br J Ophthalmol 2012;96:62–67.
21. Baier ML, Cutter GR, Rudick RA, et al. Low-contrast letter acuity testing captures visual dysfunction in patients with multiple sclerosis. Neurology 2005;64:992–995.
22. Zimmermann P, Fimm B. Test for Attentional Performance (TAP)-Version 1.02. Manual. Würselen: Psytest; 1994.
23. Cutter GR, Baier ML, Rudick RA, et al. Development of a multiple sclerosis functional composite as a clinical trial outcome measure. Brain J Neurol 1999;122:871–882.
24. Cruz-Herranz A, Balk LJ, Oberwahrenbrock T, et al. The APOSTEL recommendations for reporting quantitative optical coherence tomography studies. Neurology 2016;86: 2303–2309.
25. Lang A, Carass A, Hauser M, et al. Retinal layer segmentation of macular OCT images using boundary classification. Biomed Opt Express 2013;4:1133–1152.
26. Tewarie P, Balk L, Costello F, et al. The OSCAR-IB consensus criteria for retinal OCT quality assessment. PLoS One 2012;7:e34823.
27. Schippling S, Balk LJ, Costello F, et al. Quality control for retinal OCT in multiple sclerosis: validation of the OSCAR-IB criteria. Mult Scler 2015;21:163–170.
28. Wolak ME, Fairbairn DJ, Paulsen YR. Guidelines for estimating repeatability. Methods Ecol Evol 2012;3:129–137.
29. Vaz S, Falkmer T, Passmore AE, et al. The case for using the repeatability coefficient when calculating test–retest reliability. PLoS One 2013;8:e73990.
30. Holm SA. Simple sequentially rejective multiple test procedure. Scand J Stat 1979;6: 65–70.

31. Ross AT, ReitanIntellectual RM, Functions affective: in multiple sclerosis: a quantitative study. AMA Arch Neurol Psychiatry 1955;73:663–677.

32. Seitz AR, Sr JEN, Holloway SR, Watanabe T. Perceptual learning of motion leads to faster flicker perception. PLoS One 2006;1:e28.

33. Derrington AM, Lennie P. Spatial and temporal contrast sensitivities of neurones in lateral geniculate nucleus of macaque. J Physiol 1984;357:219–240.

34. Jacobson DM, Olson KA. Impaired critical flicker frequency in recovered optic neuritis. Ann Neurol 1991;30:213–215.

35. Raz N, Shear-Yashuv G, Backner Y, et al. Temporal aspects of visual perception in demyelinative diseases. J Neurol Sci 2015;357:235–239.

36. Petzold A, de Boer JF, Schippling S, et al. Optical coherence tomography in multiple sclerosis: a systematic review and meta-analysis. Lancet Neurol 2010;9:921–932.

37. Trip SA, Schlottmann PG, Jones SJ, et al. Retinal nerve fiber layer axonal loss and visual dysfunction in optic neuritis. Ann Neurol 2005;58:383–391.

38. Sturm W, Willmes K. On the functional neuroanatomy of intrinsic and phasic alertness. NeuroImage 2001;14(1 pt 2):S76–S84.

39. Weinges-Evers N, Brandt AU, Bock M, et al. Correlation of self-assessed fatigue and alertness in multiple sclerosis. Mult Scler J 2010;16:1134–1140.

40. Sandry M. Critical flicker frequency in multiple sclerosis. Percept Mot Skills 1963;16:103–108.

41. Misiak H. Age and sex differences in critical flicker frequency. J Exp Psychol 1947;37:318–332.

42. Ginsburg N, Jurenovskis M, Jamieson J. Sex differences in critical flicker frequency. Percept Mot Skills 1982;54(3 suppl):1079–1082.

Neurology®
Neuroimmunology
& Neuroinflammation

This information is current as of August 14, 2018

Updated Information & Services	including high resolution figures, can be found at: http://nn.neurology.org/content/5/5/e492.full.html
References	This article cites 40 articles, 4 of which you can access for free at: http://nn.neurology.org/content/5/5/e492.full.html##ref-list-1
Subspecialty Collections	This article, along with others on similar topics, appears in the following collection(s): **Attention** http://nn.neurology.org//cgi/collection/attention **Multiple sclerosis** http://nn.neurology.org//cgi/collection/multiple_sclerosis **Retina** http://nn.neurology.org//cgi/collection/retina **Visual loss** http://nn.neurology.org//cgi/collection/visual_loss **Visual processing** http://nn.neurology.org//cgi/collection/visual_processing
Permissions & Licensing	Information about reproducing this article in parts (figures,tables) or in its entirety can be found online at: http://nn.neurology.org/misc/about.xhtml#permissions
Reprints	Information about ordering reprints can be found online: http://nn.neurology.org/misc/addir.xhtml#reprintsus

AMERICAN ACADEMY OF NEUROLOGY®

Mein Lebenslauf wird aus datenschutzrechtlichen Gründen in der elektronischen Version meiner Arbeit nicht veröffentlicht.

Komplette Publikationsliste

Artikel in Fachzeitschriften

[20] Kay Gawlik, Frank Hausser, Friedemann Paul, Alexander Ulrich Brandt und Ella Maria Kadas. „Active contour method for ILM segmentation in ONH volume scans in retinal OCT". In: *Biomed. Opt. Express* 9.12 (Dez. 2018), S. 6497–6518. DOI: 10.1364/BOE.9.006497.

[23] Sunil Kumar Yadav, Ella Maria Kadas, Seyedamirhosein Motamedi, Konrad Polthier, Frank Haußer, Kay Gawlik, Friedemann Paul und Alexander Ulrich Brandt. „Optic nerve head three-dimensional shape analysis". In: *Journal of Biomedical Optics* 23 (2018), S. 23 - 23 –13. DOI: 10.1117/1.JBO.23.10.106004.

[25] Seyedamirhosein Motamedi, Kay Gawlik, Noah Ayadi, Hanna Gwendolyn Zimmermann, Susanna Asseyer, Charlotte Bereuter, Janine Mikolajczak, Friedemann Paul, Ella Maria Kadas und Alexander Ulrich Brandt. „Normative data and minimally detectable change for inner retinal layer thicknesses using a semi-automated OCT image segmentation pipeline". In: *Frontiers in Neurology* 10 (2019), S. 1117. DOI: 10.3389/fneur. 2019.01117.

[26] Noah Ayadi, Jan Dörr, Seyedamirhosein Motamedi, Kay Gawlik, Judith Bellmann-Strobl, Janine Mikolajczak, Alexander Ulrich Brandt, Hanna Gwendolyn Zimmermann und Friedemann Paul. „Temporal visual resolution and disease severity in MS". In: *Neurology - Neuroimmunology Neuroinflammation* 5 (Sep. 2018), e492. DOI: 10.1212/NXI.0000000000000492.

Kongressbeiträge

[39] V Vitkova, H Zimmermann, N Ayadi, I Martorell Serra, P Koduah, C Chien, J Kuchling, R Giess, S Motamedi, K Gawlik, J. Bellmann-Strobl, K. Ruprecht, M. Scheel, F. Paul und A. Brandt. „Quantitative OCT and MRI in MS as surrogates for clinical activity based on annual follow-ups". In: Bd. 24. Sage Publications Sage UK: London, England, 2018, S. 439–440.

[40] J Kauer, K Gawlik, I Beckers, HG Zimmermann, EM Kadas, C Bereuter, F Hausser, F Paul und AU Brandt. „Automatic quality analysis of retinal optical coherence tomography". In: Bd. 24. Sage Publications Sage UK: London, England, 2018, S. 438–439.

[41] Josef Kauer, Kay Gawlik, Hanna G Zimmermann, Ella Maria Kadas, Charlotte Bereuter, Friedemann Paul, Alexander U Brandt, Frank Haußer und Ingeborg E Beckers. „Automatic quality evaluation as assessment standard for optical coherence tomography". In: *Advanced Biomedical and Clinical Diagnostic and Surgical Guidance Systems XVII*. Bd. 10868. International Society for Optics und Photonics. 2019, S. 1086814. DOI: 10.1117/12.2510393.